

THESIS FOR THE DEGREE OF DOCTOR OF PHILOSOPHY

Innovative Electrolytes for Safer Sodium-Ion Batteries

Damien Monti



CHALMERS

Department of Physics

CHALMERS UNIVERSITY OF TECHNOLOGY

Göteborg, Sweden, 2016

INNOVATIVE ELECTROLYTES FOR SAFER SODIUM-ION BATTERIES

DAMIEN MONTI

© Damien Monti, 2016

Doktorsavhandlingar vid Chalmers tekniska högskola

ISBN: 978-91-7597-310-4

Serial number: 3991

ISSN 0346-718X

Chalmers University of Technology

Department of Physics

SE-412 96 Göteborg

Sweden

Telephone: +46 (0)31-772 3333

Fax: +46 (0)31-772 20 90

Cover:

Schematic of a sodium-ion battery

© Nicolas Monti

Printed by Chalmers Reproservice

Göteborg, Sweden, 2016

Abstract

The overconsumption of non-renewable/fossil fuels by vehicles and industry has resulted in dangerously high levels of CO₂ in the atmosphere the last 40 years. The impact on the environment, climate and public health urge governments to find new technologies to ensure a sustainable development. In this context, the development of greener energy storage technologies such as novel secondary batteries has already had a wide impact. The commercialisation of the first lithium-ion battery (LIB) in 1991 by Sony has revolutionized mobile devices and the LIB now emerges in electric vehicles, but can be even more important for load levelling of renewable energy. Unfortunately, an increase in our lithium consumption coupled with its low abundance in the Earth's crust raises financial and sustainability concerns, forcing us to think about complementary battery technologies.

One of the most appealing alternatives is to use sodium instead of lithium. Chemically these elements are close and these similarities should ease a technological change. Therefore, the sodium-ion battery (SIB) is a concept worth studying - especially for large-scale applications due to the "unlimited" abundance of sodium in the Earth's crust and the overall low materials cost, anticipated to be 30 times lower than for Li.

Electrolytes for SIBs can be based on organic solvents or ionic liquids (IL), or a mixture of both as matrices, all doped with the appropriate sodium salt. Several features and properties of hybrid IL and pure IL-based electrolytes for SIBs are investigated in this thesis; the ionic conductivity of novel electrolytes using a few ILs chosen among the large number available. These studies are complemented by Raman vibrational spectroscopy to understand the interactions within the electrolytes, and the possible operation temperature ranges by differential scanning calorimetry. Moreover, several electrolytes have been analysed to understand the IL contribution to various safety measures; ignition time (IT), flash point (FP), and self-extinguishing time (SET).

In addition, a significant part of the work is dedicated to the electrochemical compatibility of the electrolytes with novel SIB electrode materials. The stability and behaviour toward the electrodes are investigated to make possible a fully operative safer SIB in the future, possibly based on hybrid IL or pure IL-based electrolytes.

Keywords: Sodium-ion batteries, ionic liquids, organic solvents, electrodes, electrolytes, safety, Raman spectroscopy, ionic conductivity, electrochemistry.

List of Appended Papers

This thesis is based on the work presented in the following publications:

Paper I

Microwaves as a synthetic route for preparing electrochemically active TiO₂ nanoparticles
Damien Monti, Alexandre Ponrouch, Marc Estruga, M. Rosa Palacín, José A. Ayllón and Anna Roig
Journal of Materials Science, Volume 28, 2012, Pages 340-347

Paper II

Towards high energy density sodium-ion batteries through electrolyte optimization
Alexandre Ponrouch, Rémi Dedryvère, Damien Monti, Atif E. Demet, Jean Marcel Ateba Mba, Laurence Croguennec, Christian Masquelier, Patrik Johansson and M. Rosa Palacín
Energy and Environmental Science, Volume 4, 2013, Pages 2361-2369

Paper III

Ionic liquid based electrolytes for sodium-ion batteries: Na⁺ solvation and ionic conductivity
Damien Monti, Erlendur Jónsson, M. Rosa Palacín and Patrik Johansson
Journal of Power Sources, Volume 245, 2014, Pages 630-636

Paper IV

Non-aqueous electrolytes for sodium-ion batteries
Alexandre Ponrouch, Damien Monti, Andrea Boschini, Bengt Steen, Patrik Johansson and M. Rosa Palacín
Journal of Materials Chemistry A, Volume 3, 2015, Pages 22-42

Paper V

Towards safer sodium-ion batteries via organic solvents/ionic liquids based hybrid electrolytes
Damien Monti, Alexandre Ponrouch, M. Rosa Palacín and Patrik Johansson
Submitted

Additional Publication Not Included in the Thesis

Paper VI

Solvation of Li^+ and Na^+ in carbonate based battery electrolytes – a combined computational and spectroscopic study

Erlendur Jónsson, Luis Aguilera, Damien Monti, Aleksandar Matic and Patrik Johansson

Submitted

My Contribution to the Appended Papers

Paper I

I (D.M) performed the synthesis of the TiO₂ nanoparticles and the full characterization of the samples made using the laboratory microwave (MW) equipment. I electrochemically characterized the TiO₂ synthesized with the domestic MW equipment. I wrote the first draft of the paper, wrote the paper together with my colleagues, and was the first author.

Paper II

I performed the Raman spectroscopy experiments and analysis for all the electrolytes and wrote the corresponding part of paper, and co-authored the rest of the paper with my colleagues.

Paper III

I characterized all the samples by all the experimental techniques included and did all the data analysis, except for the DFT calculations. I wrote the first draft of the paper and was first author of the paper written together with my colleagues.

Paper IV

I wrote the ionic liquid part of the review including the bibliographic work. I co-authored the review with my colleagues.

Paper V

I characterized all the samples by all the experimental techniques included and did all the data analysis. I wrote the first draft and was first author of the paper written together with my colleagues.

List of Acronyms

°C	Degrees Celsius
BF ₄ ⁻	Tetrafluoroborate
BMIIm	1-butyl-3-methyl-imidazolium
CE	Counter electrode
CN	Coordination number
Cu	Copper
CV	Cyclic voltammetry
DEC	Diethyl carbonate
DFT	Density functional theory
DMC	Dimethyl carbonate
DME	Dimethoxyethane
DSC	Differential scanning calorimetry
EC	Ethylene carbonate
EMC	Ethyl methyl carbonate
EMIIm	1-ethyl-3-methyl-imidazolium
ESW	Electrochemical stability window
EV	Electric vehicle
F	Faraday's constant
F ⁻	Fluoride ion
FP	Flash point
FR	Flame retardant
FSI	Bis(fluorosulfonyl)imide
FWHM	Full width at half maximum
GCPL	Galvanostatic cycling with potential limitation
GPE	Gel polymer electrolyte
G3	Triglyme - H ₃ CO(CH ₂ CH ₂ O) ₃ CH ₃
HC	Hard carbon
HF	Hydrogen fluoride
Hz	Hertz
IL	Ionic liquid
IT	Ignition time
LE	Liquid electrolyte
LFP	LiFePO ₄
Li	Lithium
Li ₂ CO ₃	Lithium carbonate
LIB	Lithium-ion battery
LMO	LiMn ₂ O ₄
LTO	Li ₄ Ti ₅ O ₁₂
MW	Microwave

Na	Sodium
NASICON	Na Super Ionic CONductor
NiMH	Nickel-metal hydride
NVP	$\text{Na}_3\text{V}_2(\text{PO}_4)_3$
NVPF	$\text{Na}_3\text{V}_2(\text{PO}_4)_2\text{F}_3$
PC	Propylene carbonate
PEO	Poly(ethylene oxide)
PHEV	Plug-in hybrid electric vehicle
PVA	Poly(vinyl alcohol)
Pyr ₁₃	N-propyl-N-methyl-pyrrolidinium
Q	Current flux
RE	Reference electrode
RTIL	Room temperature ionic liquid
SEI	Solid electrolyte interphase
SET	Self-extinguishing time
S.H.E	Standard hydrogen electrode
SIB	Sodium-ion battery
SLI	Starting, lighting, and ignition
SN	Solvation number
SPI	Solid permeable interface
TFSI	Bis(trifluoromethanesulfonyl)imide
τ_a	Amplitude correlation time
τ_c	Correlation lifetime
T_g	Glass transition temperature
T_m	Melting temperature
TOTO	2,5,8,11-tetraoxatridecan-13-oate
WE	Working electrode
WEC	World energy consumption
VTF	Vogel-Tammann-Fulcher

List of Figures

Figure 1. Worldwide CO₂ emissions by fuel in 1973 and 2012.

Figure 2. Worldwide energy repartition (a, b) and oil consumption (c, d) by sector in 1973 and 2012.

Figure 3. Price and consumption evolution of Li₂CO₃ and soda ash during the 20th Century.

Figure 4. Schematic illustration of an SIB with E_1 and E_2 being the electrode potentials and e^- electrons. The signs are using the galvanic cell convention (anode = negative electrode).

Figure 5. GCPL data at different C-rates for a cell based on a HC WE, a Na metal CE/RE and 0.8 m NaTFSI in EC_{0.45}:PC_{0.45}:Pyr₁₃TFSI_{0.10} as the electrolyte.

Figure 6. Ragone plot of the specific capacity as function of the C-rate of electrolytes from **II** and **V**.

Figure 7. Intercalation of sodium into HC (left) vs. intercalation of lithium into graphite (right).

Figure 8. An ion pair of the IL BMImBF₄.

Figure 9. Schematic representation showing the difference between the intrinsic electrolyte ESW and the extended ESW due to the electrode/electrolyte interfaces.

Figure 10. Dielectric spectroscopy cell used for all measurements in **II** and **III**.

Figure 11. Variation of the real part $\epsilon^*(\omega)$ (solid line) $\epsilon'(\omega)$ and the imaginary part $\epsilon''(\omega)$ (dashed line) of the complex dielectric function.

Figure 12. Conductivity vs. frequency for different temperature of NaTFSI in BMImTFSI.

Figure 13. Ionic conductivity results for Na_xEMIm_(1-x)TFSI and Na_xBMIm_(1-x)TFSI for different molar fractions ($x = 0, 0.1, 0.2,$ and saturated).

Figure 14. Schematic of two masses m_1 and m_2 connected by a weightless spring with a stiffness force k .

Figure 15. Description of the Stokes and anti-Stokes processes, where E_0 and E_i are vibrational modes while $h\nu_0$ and $h\nu_s$ are photon energies.

Figure 16. Raman spectra of (a) EC_x:PC_x:BMImTFSI_(1-2x) and (b) EC_x:PC_x:Pyr₁₃TFSI_(1-2x), between 675-1075 cm⁻¹.

Figure 17. Deconvolution and fitting of peaks of TFSI, EC, and PC between 680-770 cm⁻¹ using Voigt profiles. The red line is the experimental Raman data and the green lines are the resulting individual peaks from the fitting procedure.

Figure 18. Illustration of a DSC chamber with T_s , T_R , and T_F the temperatures of the sample, reference, and furnace, respectively. ϕ_{FS} and ϕ_{FR} are the heat flow rates from the furnace to the sample, and from the furnace to the reference, respectively.

Figure 19. DSC traces of Na_xEMIm_(1-x)TFSI for different molar fractions ($x = 0, 0.1, 0.2,$ and saturated) between -150 - 150°C. Typical glass transitions, crystallizations and meltings are highlighted.

Figure 20. Microwave mechanism from dipole motion.

Figure 21. Three electrode Swagelok cell set-up.

Figure 22. CV of EC_{0.40}:PC_{0.40}:EMImTFSI_{0.20} ((E₁=0.005) – (E₂=4) V vs. Na⁺/Na^o) at a sweep rate of 1 mV/s using an Al WE; V₀=2 V vs. Na⁺/Na^o.

Figure 23. CV of 10 cycles (20 sweeps) for EMImTFSI (0-3 V vs. Na⁺/Na^o) at a sweep rate of 1 mV/s using a SS WE.

Figure 24. GCPL data for a half cell of NVP of 0.8 m NaTFSI in EC_{0.45}:PC_{0.45}:Pyr₁₃TFSI_{0.10} electrolyte cycled at different C-rates.

Figure 25. GCPL data for the charge and discharge of NVP with 0.8 m NaTFSI in EC_{0.45}:PC_{0.45}:Pyr₁₃TFSI_{0.10} as electrolyte at different C-rates. The alternation between fast and slow C-rates is used to test the structural and chemical stability/reversibility.

Figure 26. Isotherms of the conductivity for (a) Na_xEMIm_(1-x)TFSI and (b) Na_xBMIm_(1-x)TFSI for different molar fractions (x = 0.025, 0.05, 0.075, 0.1, 0.15, 0.2, and saturated). (III)

Figure 27. Conductivities of (a) EC_x:PC_x:BMImTFSI_(1-2x) and (b) EC_x:PC_x:Pyr₁₃TFSI_(1-2x) as functions of temperature. (V)

Figure 28. Viscosity of (a) EC_x:PC_x:BMImTFSI_(1-2x) and (b) EC_x:PC_x:Pyr₁₃TFSI_(1-2x) as functions of temperature. (V)

Figure 29. Isotherms of the conductivity for (a) Na_xEMIm_(1-x)TFSI and (b) Na_xBMIm_(1-x)TFSI for different molar fractions (x = 0.025, 0.05, 0.075, 0.1, 0.15, 0.2, and saturated). (III)

Figure 30. Various safety measures as functions of the electrolyte IL content: (a) FP, (b) IT, and (c) SET. Reference data for 1M MPF₆ in EC:DMC (M=Na, Li) are represented by horizontal lines. (V)

Figure 31. Raman spectra of Na_xEMIm_(1-x)TFSI and Na_xBMIm_(1-x)TFSI between 725-765 cm⁻¹ for different molar fractions with the deconvolution and fitting for Na_xEMIm_(1-x)TFSI, x=sat, as insert.

Figure 32. Raman spectra of 1 M NaTFSI in EC_x:PC_x:DMC_(1-2x) between 880-940 cm⁻¹ for different electrolyte compositions (x= 0.25, 0.33, 0.45, and 0.50).

Figure 33. Capacity versus cycle number for MWA₂₀₀ (green inverted triangles), MWA₂₀₀⁵⁰⁰ (red triangles), DMW_{BTMA} (black circles), DMW_{TEA} (blue squares) (left), and capacity versus cycle number of DMW_{BTMA} (black circles) and DMW_{TEA} (blue squares) (right) all cycled at C/15-rate. (I)

Figure 34. Typical behaviour of the anatase TiO₂ anode material (MW₂₀₀⁵⁰⁰) between 1-3 V vs. Li⁺/Li^o.

Figure 35. (a) 1st cycle voltage vs. normalized capacity profiles for HC using 1 M NaClO₄ in EC:PC:DMC electrolytes with various amounts of DMC recorded at C/20-rate, (b) discharge capacity and (c) coulombic efficiency vs. cycle number for the corresponding half-cells.

Figure 36. (a) Coulombic efficiency and discharge capacity vs. cycle number for HC electrodes tested at C/10, C/5, 1C, and 2C-rates and a EC_{0.45}:PC_{0.45}:Pyr₁₃TFSI_{0.10} electrolyte and (b) Potential vs. capacity profiles at different C-rates for HC and a EC_{0.45}:PC_{0.45}:Pyr₁₃TFSI_{0.10} electrolyte.

Figure 37. (a) Voltage vs. capacity profiles for HC || NVPF full SIB cells cycled with 1 M NaPF₆ or 1 M NaClO₄ in EC_{0.45}:PC_{0.45}:DMC_{0.1} electrolytes recorded at C/5-rate (b) Voltage vs. capacity profiles for HC || NVPF full SIB cells cycled with 1 M NaPF₆ in EC_{0.45}:PC_{0.45}:DMC_{0.10} electrolytes at different C-rates.

List of Tables

Table 1. Worldwide primary energy supply, final energy consumption, and electricity generation between 1973 and 2012.

Table 2. Comparison of lithium and sodium resources and the main electrochemical properties.

Table 3. Comparison of cell voltages, typical electrode materials, and resulting approximate energy densities at the cell level for the NiMH, LIB, and SIB technologies.

Table 4. Some SIB and LIB cell energy densities (Wh.kg^{-1}) from BatPaC modelling. The battery size is expressed as an expected EV driving range (miles).

Table 5. Summary of SIB anode materials with potentials of insertion and specific capacities (* = for first charge/discharge cycle).

Table 6. Some SIB cathode materials with potentials for sodium insertion and resulting specific capacities.

Table 7. Comparison of different SIB electrolyte concepts.

Table 8. Linear and cyclic carbonate solvents for battery electrolytes.

Table 9. Conductivity (σ), viscosity (η), ESW, and thermal stability of common SIB electrolytes.

Table 10. Molecular vibration modes with their characteristics. The + and - signs correspond to movements vs. the plane.

Table 11. Functional groups/vibration modes and their approximate positions in a Raman spectrum.

Table 12. Associated vibrational modes to bands used in the analysis of hybrid electrolytes.

Table 13. Solvation number analysis of hybrid electrolytes for two different types of ILs.

Table of Contents

Abstract	i
List of Appended Papers	ii
Additional Publication Not Included in the Thesis	iii
My Contribution to the Appended Papers	iv
List of Acronyms	v
List of Figures	vii
List of Tables	ix
1 Introduction	1
2 Batteries	5
2.1 General Concepts and the SIB.....	8
2.2 SIB Electrodes.....	10
2.2.1 Anodes	10
2.2.1.1 Carbon Based Anodes.....	11
2.2.1.2 Non-carbonaceous Anodes	12
2.2.2 Cathodes	13
2.3 Electrolytes.....	15
2.3.1 Organic Solvents Based Electrolytes.....	17
2.3.2 Ionic Liquids	19
2.3.2.1 Ionic Liquid Based Electrolytes.....	20
2.3.3 Hybrid Electrolytes.....	21
2.4 Electrode/Electrolyte Interfaces	22
2.4.1 The Solid Electrode Interphase (SEI) and the Solid Permeable Interface (SPI)	22
2.5 Safety Concerns.....	24
3 Experimental Methods	25
3.1 Dielectric Spectroscopy.....	25
3.1.1 Data Interpretation	27
3.2 Raman Spectroscopy.....	29
3.2.1 Theory of Raman Scattering.....	29
3.2.1.1 Classical Wave Interpretation	29

3.2.1.1 Quantum Particle Theory	31
3.2.2 Molecular Vibrations.....	33
3.2.3 Raman Data Interpretation	34
3.3 Differential Scanning Calorimetry (DSC)	37
3.3.1 Theoretical Foundation.....	37
3.3.2 DSC Data Interpretation.....	39
3.4 Microwave Synthesis	39
3.4.1 Microwaves and Electrode Synthesis	40
3.5 Cyclic Voltammetry (CV)	41
3.5.1 Theoretical Foundation	42
3.5.2 CV Data Interpretation	44
3.6 Chronopotentiometry	45
3.7 Safety Assessments	46
3.7.1 Flash Point (FP)	46
3.7.2 Ignition Time (IT)	47
3.7.3 Self-Extinguishing Time (SET).....	47
4 Results and Discussions.....	49
4.1 Physical Properties of IL Based SIB Electrolytes	49
4.2 Sodium Ion Solvation and Coordination	53
4.3 Electrode Synthesis and SIB Performance	56
5 Conclusions and Outlook	61
Acknowledgements.....	63
Bibliography.....	64

1 Introduction

In 1760, the occidental world witnessed a turning point which had a major impact on the standard of living for the general population. It is known as the “1st industrial revolution” and lasted until 1840 [1]. During this period, the industry moved from hand production methods to machines, developed new chemical manufacturing and iron production processes, improved efficiency of water power, saw the increasing use of steam power, and worked on the development of machine tools. The use of wood and bio-fuels was replaced by coal, nowadays coined a “fossil” fuel. The use of petroleum as it is known today started in 1840 with the “2nd industrial revolution” and helped the development of textile and chemical industries, and later on the automotive industry [2, 3]. Unfortunately, this quick energy race initiated industrial pollutions that severely impacted public health. The first catastrophe happened in London in 1873 when numerous “killer fogs” caused over 1150 deaths in only three days from severe air pollution due to coal burning. Aside sanitary concerns, later on climate modifications and the new global awareness of CO₂ emissions and levels and greenhouse gases in general were seriously discussed in for example 1992 with the establishment of the Kyoto protocol. But as of today 2016 has just started and have the Kyoto protocol directives really been followed? As an example, the air in Beijing is so polluted due to the extensive use of coal that breathing damages the lungs as much as smoking 40 cigarettes a day and at the same time the pollution overall kills 4000 people every day in China [4]. Moreover, the global CO₂ emissions by fuel consumption have more than doubled since 1973 (Fig. 1) [5].

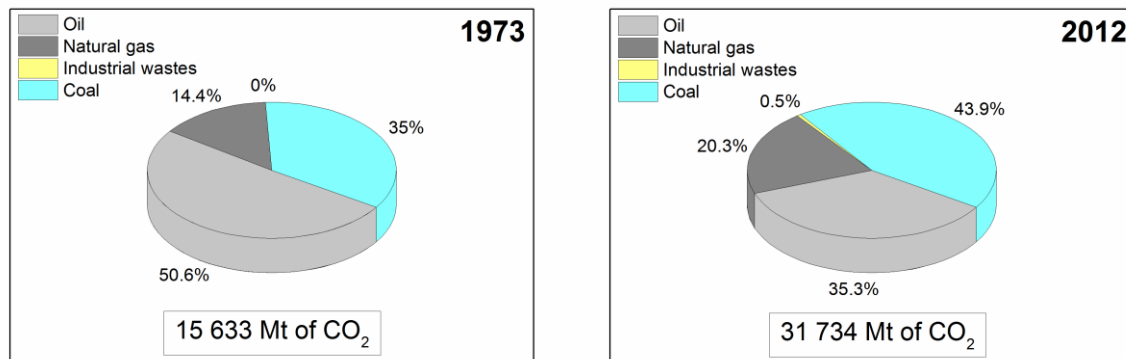


Figure 1. Worldwide CO₂ emissions by fuel consumption in 1973 and 2012.

Another issue is the world energy consumption (WEC) *i.e.* the total energy used by the human civilization per year including every energy source used in the industrial and technologic sectors world-wide. The energy partition shows fossil fuel based energy (coal, natural gas, oil) to still be close to 70% of the WEC in 2012 (Fig. 2) [5]. Also the final energy consumption (energy after processed into usable forms) and electricity generation reveal large increases over the years (Table 1). Facing an inevitable fossil fuel depletion, research towards electrical energy storage for renewable and variable energy has been intensified the past 20 years. In this context, secondary batteries have rapidly evolved since the early 1990’s due to the boost of mobile electronics [6] and are today part of our everyday lives [7-9]. This technology can partially solve the urge for balancing renewable and green energy, with a focus on large scale applications, in particular by storing the energy from solar cells and wind turbines. It is thus an absolute current necessity to improve and develop new

energy storage technologies and materials suitable for high performance devices to satisfy the increasing market demand.

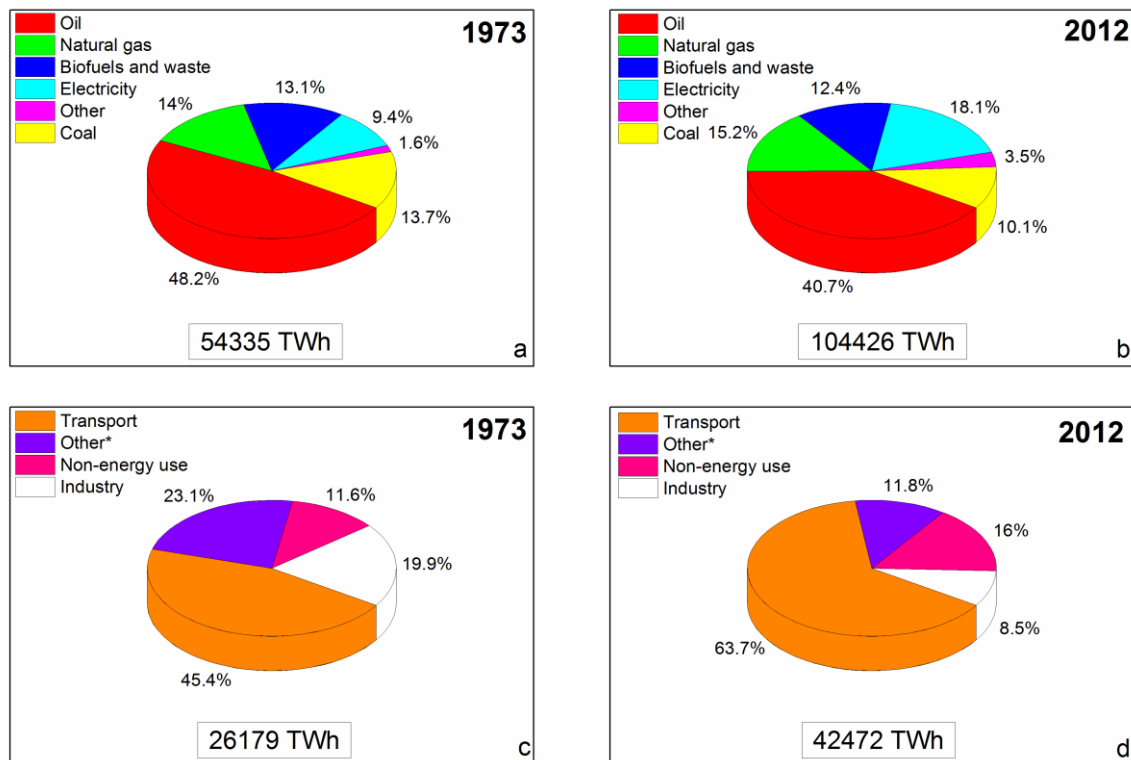


Figure 2. Worldwide energy repartition (a, b) and oil consumption (c, d) by sector in 1973 and 2012.

Table 1. Worldwide primary energy supply, final energy consumption, and electricity generation between 1973 and 2012.

Year	Primary energy supply	Final energy consumption	Electricity generation	Ref.
1973	71013	54335	6129	[5]
1990	102569	-	11821	[5]
2000	117687	-	15395	[5]
2010	147899	100914	21431	[10]
2011	152504	103716	22126	[11]
2012	155505	104426	22668	[5]

The lithium-ion battery (LIB) technology is currently the energy storage technology of choice for hybrid and fully electric vehicles (EVs), and is starting to play a role also for large scale energy storage. There are, however, numerous debates on the limited lithium supply and the lithium consumption (Table 2 and Fig. 3), and thus it is useful to put forth complementary electric energy storage technologies [12-14]. As an example, the Chevrolet Volt plug-in hybrid electric vehicle (PHEV) with a 17.1 kWh LIB necessitates 3 kg of raw Li_2CO_3 (≈ 440 g of Li). Based on the annual world production of Li_2CO_3 it would be possible to

build *ca.* 12,350,000 such PHEVs a year. This figure is far from the total of 67,000,000 cars produced in 2014 [15]. Moreover, this does not take into account the still growing portable electronics market, large electric storage facilities, ceramics industry, or the growing pharmaceutical need for lithium, all severely reducing the amount of lithium available [16]. They also do not include the growing commercial vehicle demand for electrification. In all, these factors will modify the price tag for all materials, not only Li_2CO_3 , needed to construct the energy storage (Fig. 3).

Table 2. Comparison of lithium and sodium resources and the main electrochemical properties.

Lithium (Li_2CO_3)	Property	Sodium (Soda Ash)
37 [16]	World Production (thousands of metric tons)	52,000 [16]
13,000 [16]	World reserves (thousands of metric tons)	24,000,000 [16]
39,500 [16]	World resources (thousands of metric tons)	>50,000,000 [16]
4500 [16]	Price (\$ton ⁻¹)	155 [16]
3829 [17]	Theoretical capacity (Metal) (mAhg ⁻¹)	1165 [17]
0	Electrochemical Potential E_0 (V vs. Li^+/Li^0)	0.3 [17]

Sodium based battery technologies were seriously considered in the 1970's and 1980's prior to the emergence of the LIB concept in the 1990's, but why? Sodium (Na) is ranked as the 4th most abundant element on Earth [16] and its derivatives are massively produced and consumed (Fig. 3) around the world for various applications such as basic chemicals (sodium bicarbonate, sodium chromates, sodium phosphates, and sodium silicates), and glass containers for beverages, household products, food, liquor, medical products, toiletries and cosmetics, as well as in soaps and detergents. Chemically, Li and Na are close and the similarities should ease a technological change from LIBs to sodium-ion batteries (SIBs). Therefore SIBs have been intensively "re-studied" the past decades and seem to be technologically viable. In Table 3 three secondary battery technologies are compared; SIBs, nickel-metal hydride (NiMH) batteries, and LIBs. The cell voltage and the energy density are two characteristics discussed in the following section.

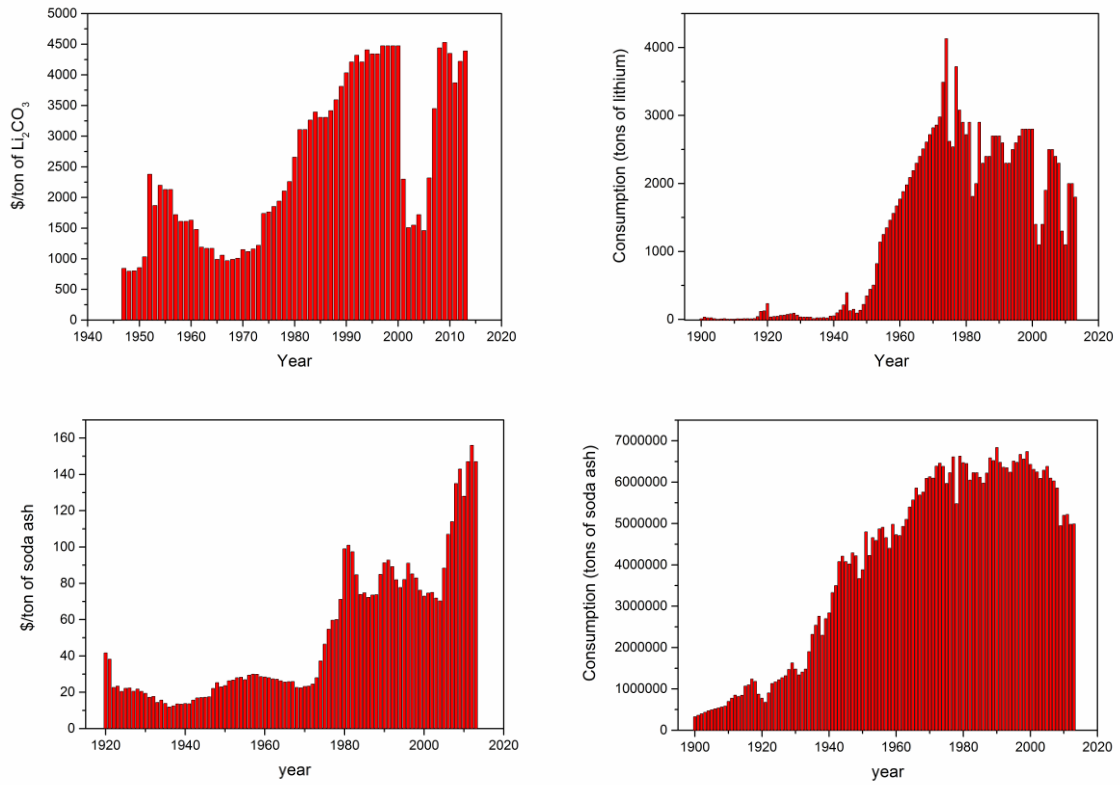


Figure 3. Price and consumption evolution of Li_2CO_3 and soda ash during the 20th Century.

Table 3. Comparison of cell voltages, typical electrode materials, and resulting approximate energy densities at the cell level for the NiMH, LIB, and SIB technologies.

Property\Battery technology	NiMH [18, 19]	LIB [9, 20]	SIB [21, 22]
Nominal voltage [V]	1.20	3.70	3.65
Anode material	H in TiNi_2	Graphite	Hard Carbon
Cathode material	NiOOH	LiCoO_2 or $\text{Li}(\text{Ni}_x\text{Co}_y\text{Al}_z)\text{O}_2$ (NCA)	$\text{Na}_3\text{V}_2(\text{PO}_4)_2\text{F}_3$ (NVPF)
Energy density [$\text{Wh}\cdot\text{kg}^{-1}$]	30-80	175-240	78-365

2 Batteries

When it comes to storing energy, secondary batteries converting chemical energy into electrical energy – and vice versa – are one of the most efficient devices (far beyond hydraulic and thermal storage). A battery is an electrochemical device composed of one or more electrochemical cells that can be assembled both in parallel and series depending on the currents and voltages desired. Historically, Alessandro Volta two centuries ago constructed the first battery [23], later known as the voltaic cell, based on copper and zinc plates and with an electrolyte made of brine. However, Volta did not realize that the operation of the cell was the result of redox (**reduction-oxidation**) reactions, but rather used an obsolete scientific theory known as contact tension to justify the current as a result of two materials simply touching each other [23].

But what are redox reactions? Redox reactions include all chemical reactions in which the oxidation states of atoms change – and thus involve the transfer of electrons between species. By definition oxidation is an increase in oxidation state by a molecule, atom, or ion, while reduction is a decrease in oxidation state. This concept is the basis of all electrochemistry.

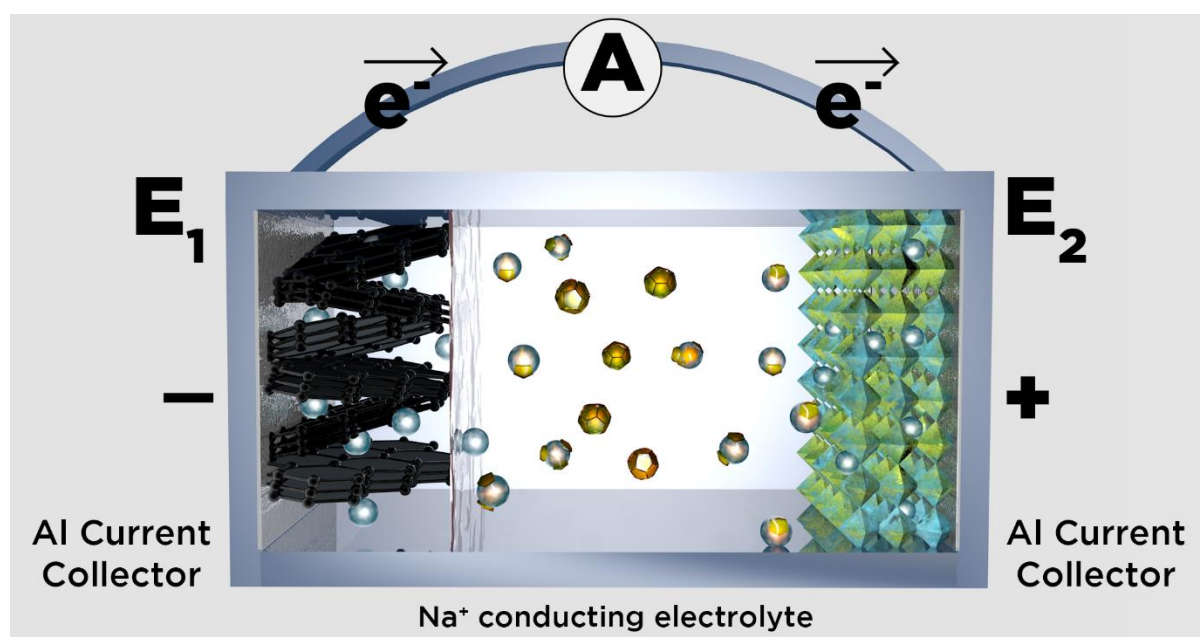


Figure 4. Schematic illustration of an SIB with E_1 and E_2 being the electrode potentials and e^- electrons. The signs are using the galvanic cell convention (anode = negative electrode).

Two electrodes and an electrolyte is the basic composition of all electrochemical cells. If the electrolyte is liquid, a porous separator (membrane) can be used to allow the ion transport while avoiding short circuit by direct contact between the electrodes. The use of a separator can be avoided by having a large enough distance between the electrodes *i.e.* two wires in a beaker, but this large excess of electrolyte makes the whole system less efficient. Battery

technologies using solid polymer, gel polymer, or ceramic electrolytes are not in need of separate separators [9, 24].

The electrodes are usually a composite of several materials making the final product mechanically stable and electrochemically performing; the active electrode material itself, some sort of carbon added to enhance electronic conductivity, and a binder to hold all together [25]. The crystal structure of the active electrode material and its composition determines the electrochemical potential of the material/electrode. By definition “cathode” and “anode” are the positive and negative electrodes, respectively, for a secondary battery. The anode/cathode designation is switching depending on whether the battery is charging or discharging, while the negative/positive nomination remains unchanged. As soon as the two electrodes with potentials of E_1 and E_2 , respectively, are connected by an external circuit, the difference in potential between the electrodes ($E_{cell} = E_1 - E_2$) causes electrons to flow spontaneously from the more negative to the more positive potential (Fig. 4) – which can be used to drive a device. The cell maintains charge balance by the internal ionic transfer within the electrolyte. All is a result of an overall process where the system releases Gibbs free energy (ΔG) [26] (Eq. 1) and moves to a thermodynamically more stable state:

$$\Delta G = -nFE_{cell} \quad (1)$$

where n is the number of electron transferred, F is the Faraday’s constant, and E_{cell} the electrochemical potential difference.

Usually, the *specific capacity* (C) is extracted from a plot such as presented in Fig. 5 by the following relation:

$$C = \frac{nF}{M_w 3.6} \quad (2)$$

where M_w is the molar weight of the active electrode material (in g/mol) in the cell’s native assembled state (charged or discharged), and C the specific capacity expressed in mAhg^{-1} .

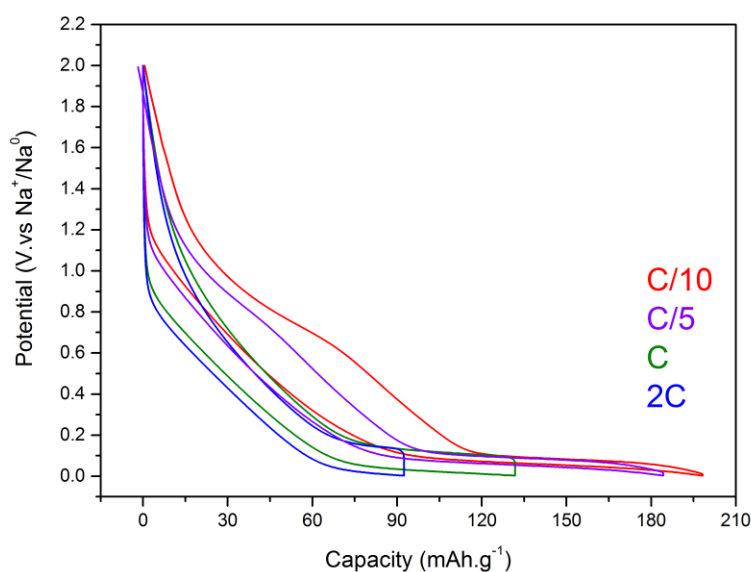


Figure 5. GCPL data at different C-rates for a cell based on a HC WE, a Na metal CE/RE and 0.8 m NaTFSI in EC_{0.45}:PC_{0.45}:Pyr₁₃TFSI_{0.10} as the electrolyte.

The electrochemical stability is very important as the materials used should not be degraded during cycling. The electrochemical stability window (ESW) is the voltage range within which a battery can operate without detrimental decomposition of the electrolyte or any of the electrodes.

When comparing the capacities of the charge and the discharge of an electrochemical cell, the coulombic efficiency can be calculated which ideally should be as close as possible to 100%, in practical cells this often reaches 99.99%. However, this efficiency must not be taken as the single parameter to measure the performance of the cell and its evolution upon cycling. Indeed, a cell where the electrodes are damaged by side reactions would exhibit a gradual decrease in capacity, but may still have high coulombic efficiency if the products can be further oxidized/reduced.

The specific capacity furthermore depends on the kinetics of the electrode reactions: the C-rate. For redox reactions involving insertion of ions in the electrode active material, a C-rate of C/5 for example corresponds to the insertion of 1 mole of ions (for instance Na⁺ or Li⁺) in 5 hours. The dependence of the specific capacity of a material on the C-rate is typically shown in a Ragone plot (Fig. 6).

Based on the capacities of the cathode and the anode a balanced assembly of a full cell is possible. As an example: with anode and cathode materials of specific capacities of 80 mAhg⁻¹ and 160 mAhg⁻¹, respectively, twice the amount of the anode material as compared to the cathode material (by weight) is needed. This calculation is, however, based only on the active materials, why the amount of the “real” anodes and cathodes may differ substantially, as a result of possible different percent of active materials in each case.

The difference in potential between the two electrodes, together with the specific capacity of the balanced full cell defines the theoretical specific energy *i.e.* the maximum amount of energy stored per mass [18]:

$$\text{Theoretical specific energy} = -\frac{\Delta G}{\sum M_w} = C E_{cell} \quad (3)$$

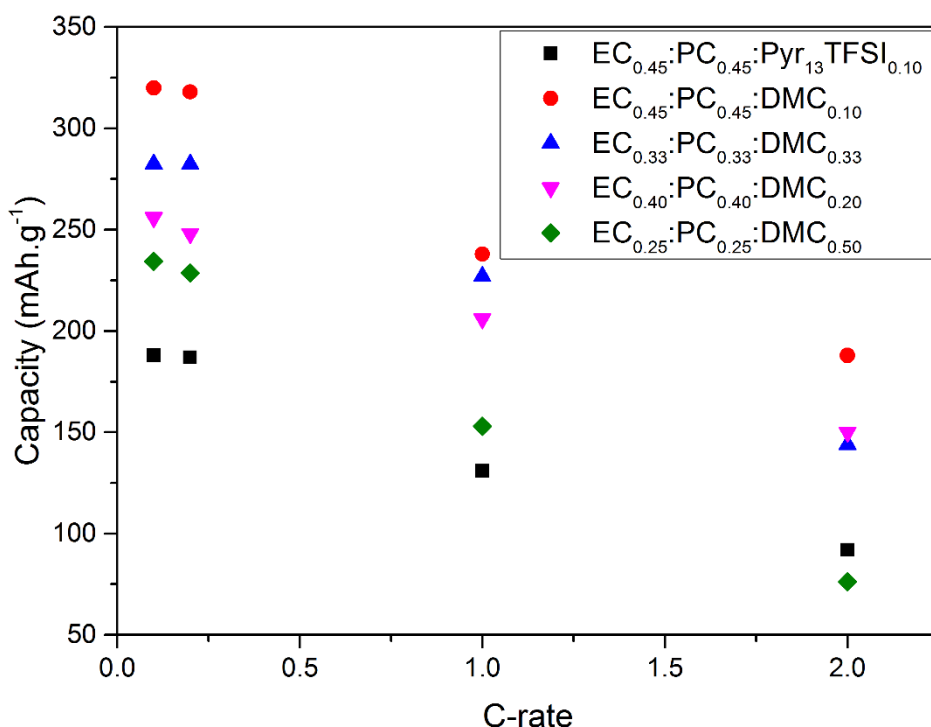


Figure 6. Ragone plot of the specific capacity of HC as function of the C-rate using electrolytes from papers II and V.

2.1 General Concepts and the SIB

The secondary lithium battery beginnings were extremely promising, as the theoretical specific capacity of a lithium metal anode is very large: 3860 mAhg⁻¹ [27] (Table 2). Unfortunately, the uneven deposition of lithium during cycling, ultimately resulting in dangerous dendrite growth, made them unsuitable for any commercial applications [7]. An early idea was to substitute the Li metal anode by an alloy with aluminum, these electrodes, however, have a short life-time due to large volumetric expansion upon cycling [28]. In the end, the metallic lithium anode was substituted by a much safer insertion material, graphite, operating at low potential [6]. This concept was coined “rocking-chair”, as the lithium now “rocks” between two intercalation electrodes. This is still the basis of the

current LIB technology and attractive due to its light weight, compactness, and the resulting high energy density – both by weight and volume.

However, due to economic reasons and Li availability, a currently appealing alternative/complement to the LIB is the SIB, introduced both for the vast abundance of sodium and its relatively low cost compared to lithium (Fig. 3). Ironically, the SIBs could have been as successful as the LIBs; they were investigated simultaneously in the 1970's and 1980's [29-41] until the LIB was commercialized in the 1990's by Sony [6, 42]. The energy densities of SIBs can be comparable to LIBs (Table 3), which really stems from the LIB technology not being based on Li metal anodes (above). The > x3 ratio of the specific capacities of the metals (3829/1165 in Table 1) is therefore reduced to ≈ 1.2 for carbonaceous intercalation materials (graphite/HC \rightarrow 360/300), but this ratio can be modified for different materials. There thus is a much smaller *a priori* theoretical energy density penalty when moving from LIBs to SIBs than what first can be expected [27]. By creating “realistic” cell layouts for example by the software BatPaC [43], energy densities for various cylindrical cells can be modelled. For an SIB the input can be: Al current collectors at both sides, a 3.65 V operating voltage, and capacities of 110 mAhg⁻¹ and 300 mAhg⁻¹ for the cathode and anode active materials, respectively, which are the compounds studied in II. Comparing the so obtained SIB energy density vs. some standard LIB cell configurations show in real numbers how competitive the SIB technology can be (Table 4).

Table 4. Some SIB and LIB cell energy densities (Wh.kg⁻¹) from BatPaC modelling. The battery size is expressed as an expected EV driving range (miles).

EV range\Cell chemistry	SIB		LIBs	
	HC/NVPF	Graphite/LFP	Graphite/LMO	LTO/ LMO
11.2	78	74	90	63
16.8	93	88	106	68
22.4	104	99	109	70
28.0	113	103	114	72
33.6	119	104	118	74
39.2	120	106	118	75
44.8	123	108	120	76

Recently, a lot of work has been carried out to compare the common characteristics of the LIB and SIB technologies, for example in the theoretical study by Ong et al. [44] for similar materials operating in LIBs and SIBs. For larger batteries the use of Al current collectors

(rather than Cu) means a significantly reduced mass as larger batteries involve relatively larger mass of current collectors. The numbers presented in Table 4 are more or less based on bench-scale results applied rudimentary to “the world of real batteries”, and do not include *e.g.* life-length, safety, or fabrication issues. Yet, they serve to disprove the “common belief” that SIBs intrinsically have worse energy densities than LIBs – a misunderstanding based on the potential difference between the Li and Na metals of *ca.* 0.3 V and their different capacities (Table 3).

2.2 SIB Electrodes

2.2.1 Anodes

As compared to lithium metal, it is even more problematic to use sodium metal based anodes as the melting point is relatively low (98°C) [17]. Therefore, alternative anode materials were early studied, in most cases similar to those investigated for LIBs, and a small overview is presented in Table 5. Most early SIB studies envisaged to use graphite, the typical LIB anode due to its high capacity (372 mAhg⁻¹), low potential (<0.1 V vs. Li⁺/Li⁰), and high stability [45-47]. Unfortunately, sodium does not intercalate efficiently in graphite [48], often explained in terms of thermodynamics [45-47].

Table 5. Summary of SIB anode materials with potentials of insertion and specific capacities (* = for first charge/discharge cycle).

Anode materials	Potential of insertion [V vs. Na ⁺ /Na ⁰]	Capacity [mAhg ⁻¹]	Reference
Hard carbon	0.005	300	[49]
Hard carbon C1600	0.005	416	[50]
Na ₂ Ti ₃ O ₇	0.3	178	[51]
TiO ₂	1.5	150	[52]
NiCo ₂ O ₄	> 2.0	200	[53]
Sb ₂ O ₄	0.5	800	[54]
SnSb/C	0.2	544	[55]
NaTi ₂ (PO ₄) ₃	2.1	130	[56]
Ni ₃ S ₂	0.8	400	[57]
MoS ₂	1.2	1000	[58]
SnS/C	1.2	1050	[59]
SnS ₂ /C	1.2	750	[59]
Sn ₄ P ₃	< 1.0	800	[60]
NiP ₃	0.4	1000	[61]
Na ₁₅ Sn ₄	< 0.2	847	[62, 63]
Na ₃ Sb	0.7	660	[63]
Fe ₃ O ₄ *	1.1	643/366	[64]
Fe ₂ O ₃ *	1.0	618/200	[65, 66]
α – MoO ₃ *	1.4	771/410	[67]
CuO*	0.8	935/640	[68]
Na ₂ C ₈ H ₄ O ₄	0.29	250	[69]

2.2.1.1 Carbon Based Anodes

While graphite thus cannot be used [48], other kinds of carbon based electrodes have been extensively investigated. In 1993, carbon based sodium intercalation materials such as petroleum coke (maximum Na content = NaC_{30}) and Shawinigan black (NaC_{15}) were examined by Doeff *et al.* [70] and cycled using PEO- NaCF_3SO_3 electrolytes [71]. The resulting SIB had a capacity of 85 mAhg^{-1} , at the time the highest value ever reported for electrochemical intercalation of Na using carbonaceous materials [70].

While the above SIB used a polymer electrolyte, the use of liquid electrolytes with SIBs became successful first when hard carbon (HC) was used as the anode by Prof. Dahn's group [49]. HC is a non-graphitizable carbon with inherent nano-porosity due to the random stacking of graphene sheets and with pores on the order of the size of the graphene sheets (Fig.7). HC is at the moment the standard negative electrode of SIBs. Its disordered structure allows sodium ions to be intercalated in the structure from any direction at the same time as it exhibits a good reversibility. It has been recently synthesized from pyrolysis of sugar and exhibit a theoretical capacity of 300 mAhg^{-1} [72]. Moreover, HC has a very low potential of insertion (*ca.* $0.005 \text{ V vs. Na}^+/\text{Na}^0$) [70, 73-75]. This ensures a viability to create high energy density SIB cells with high potential cathodes, but can also be a disadvantage; a high current may force plating of metallic Na which makes the cell unstable and unsafe.

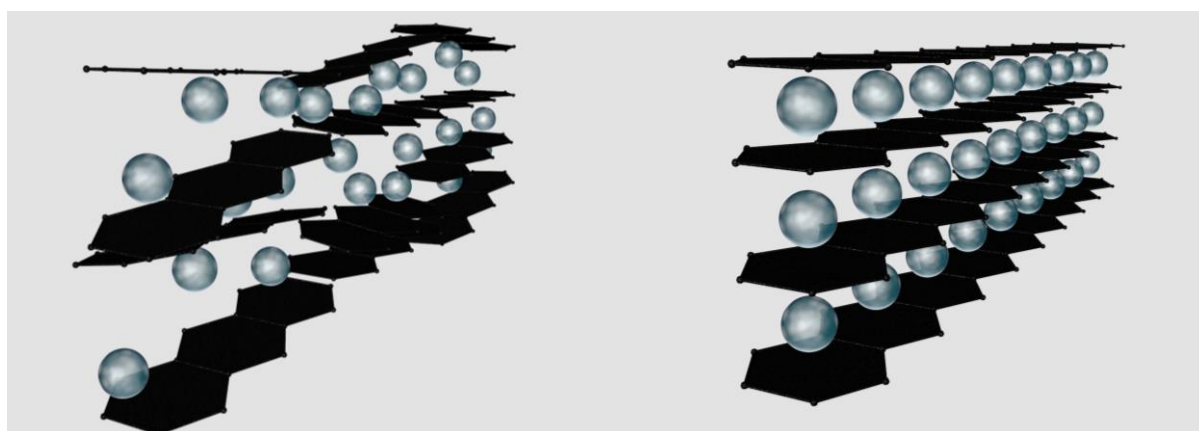


Figure 7. Schematic of the intercalation of sodium into HC (left) vs. lithium into graphite (right).

Recently, a new of HC called "C1600", fabricated from an organic polymer with an aromatic ring and heat-treated in non-reactive gas at 1600°C with a specific surface area of about $10 \text{ m}^2\text{g}^{-1}$ was studied in SIBs utilizing different electrolytes [76]. The best performance was obtained using NaClO_4 in EC:DMC as the electrolyte, giving an initial capacity of 413 mAhg^{-1} , 50 cycles, and being more thermally stable than its Li analogue [50].

2.2.1.2 Non-Carbonaceous Anodes

Alternatives to the carbonaceous materials have been investigated during the last decade and several metal alloys and oxides with high capacities and cyclabilities have been reported (Table 5). Titanium oxides based have been explored [54, 56, 77-80] [51], with the prominent example being $\text{Na}_2\text{Ti}_3\text{O}_7$ with good cyclability and coulombic efficiency and a potential of insertion at 0.3 V vs. $\text{Na}^+/\text{Na}^\circ$, and the option of two Na to be reversibly extracted and inserted into the structure. The main drawback is a high capacity fading upon cycling. As a comparison, layered NaTiO_2 is electrochemically active at *ca.* 1 V vs. $\text{Na}^+/\text{Na}^\circ$ allowing the insertion of only 0.3-0.5 Na [77] and TiO_2 in the form of amorphous nanowires can be cycled at *ca.* 1.5 V vs. $\text{Na}^+/\text{Na}^\circ$ and 0.4 Na at best [52]. An insertion potential of 1.5 V vs. $\text{Na}^+/\text{Na}^\circ$ is, however, too high for the cathodes available; the cell voltage becomes too low. $\text{NaTi}_2(\text{PO}_4)_3$, also a titanium based anode material, has a insertion potential even higher, *ca.* 2.7 V vs. $\text{Na}^+/\text{Na}^\circ$.

Besides the titanium oxides, compounds exhibiting a redox mechanism not based on the insertion of ions in the structure, but in its complete transformation (“conversion reactions”) have been extensively studied. These materials always involve multiple electron reactions, which translate into high specific capacities, yet the voltage hysteresis between oxidation and reduction is a handicap. LIB and SIB conversion reaction materials share these same features.

Oxide materials electrochemically forming alloys with sodium upon cycling, such as Sb_2O_4 , display high specific capacities, but have stability issues due to their high volumetric expansion upon alloying. This problem may be alleviated, for example SnO_2 nanoparticles embedded in a soft-templated mesoporous carbon framework have been shown to exhibit even better performance in SIB than in LIB cells [81]. In total these anodes show an efficient alloying/dealloying mechanism, a low reaction potential vs. $\text{Na}^+/\text{Na}^\circ$, a high theoretical capacity (*ca.* 667 mAhg^{-1}), a low cost, and are environmental benign [81-83]. Also, the cycling ability, capacity retention and coulombic efficiency was proven for more than 2000 cycles at a high current density. As for other materials layered sulphides have been used [30, 33, 84, 85] and present up to 400 mAhg^{-1} at 0.84 V vs. $\text{Na}^+/\text{Na}^\circ$, but with very bad cyclability [57, 86], while intermetallic or alloy materials (Sn/C , SnSb/C) have shown capacities of up to 544 mAhg^{-1} [55, 87], but the large volumetric expansions of these materials is yet a hurdle to overcome.

At last, SIB anodes based on organic compounds have shown some promise; for example disodium terephthalate ($\text{Na}_2\text{C}_8\text{H}_4\text{O}_4$) has a specific capacity of 250-350 mAhg^{-1} at an insertion potential of 0.29 V vs. $\text{Na}^+/\text{Na}^\circ$ [69, 88]. Benzenediacylates show relatively low capacities of 45-50 mAhg^{-1} though constant for more than 100 cycles [89].

2.2.2 Cathodes

The cathode material usually has Na in its composition, thus serving the SIB with the needed Na^+ charge carriers and leading to the cell being assembled in the discharged state. These Na are thus always extracted during the first charge, typically at high potential. SIB cathode materials have been extensively studied in parallel to the various SIB anode materials – several reviews exist [17, 34, 90-93].

Layered sodium transition oxides, Na_xMO_2 (M=transition metals) are promising candidates for positive electrodes, sharing properties with their Li counterparts. The crystal structures are built up by stacking sheets of edge-sharing MO_6 octahedra and a notation was developed by Delmas *et al.* [31] based on the coordination of Na ions in the interlayer space. Two main structures have shown attractive electrochemical capacities, *i.e.* the O3-type and the P2-type, where Na exhibit octahedral (O) and prismatic (P) coordination, respectively. However, the P2-type cannot be stabilised with a Na stoichiometry larger than $\text{Na}_{2/3}\text{MO}_2$ [94]. Even if early studies from the 1970-1980's of sodium containing layered electrodes can be found for Na_xMnO_2 and Na_xCoO_2 [36, 37], the studies of layered oxides for SIBs was greatly facilitated by the numerous earlier studies made on LIB materials such as LiCoO_2 and NMC. Hence, since the revival of SIBs by *ca.* 2010, many research groups have aimed to improve the intercalation properties and the cycling performance of Na layered electrodes, with a consistent argument being the LIB vs. SIB comparisons/similarities. Some properties, such as the diffusion barriers of ions in XCoO_2 (X=Li,Na) and the mechanical stability of O3- XMO_2 , are in favour of SIBs as shown by Ceder *et al.* [44]. Another advantage of the use of sodium is related to chromium phases (XCrO_2), where the Li electrode is electrochemically inactive while the Na electrode displays a reversible capacity of 120 mAhg^{-1} at 3 V vs. $\text{Na}^+/\text{Na}^\circ$ [95]. Layered electrodes with large capacities have recently been synthesized where the O3 and P2 phases can be directly compared. As an example, O3- $\text{Na}[\text{Fe}_{1/2}\text{Mn}_{1/2}]\text{O}_2$ and P2- $\text{Na}_{2/3}[\text{Fe}_{1/2}\text{Mn}_{1/2}]\text{O}_2$ revealed the O3 and P2 phases to have capacities of 110 mAhg^{-1} and 190 mAhg^{-1} , respectively [96], while the Na analogue of NMC ($\text{Na}[\text{Ni}_{1/3}\text{Mn}_{1/3}\text{Co}_{1/3}]\text{O}_2$) (O3-type) showed a capacity of 100 mAhg^{-1} (vs. 120 mAhg^{-1} for Li) and cycling stability for 150 cycles [97].

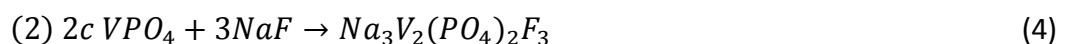
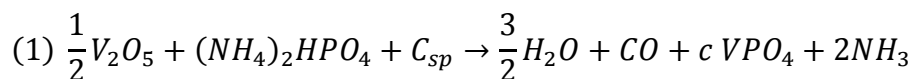
In addition to layered structures, 3D polyanionic frameworks, with the advantage of enhanced structural stability, have also been studied as cathode materials for SIBs [98]. The olivine structured LiFePO_4 is successfully used in commercial LIB cells, while for SIBs, NaFePO_4 exhibit maricite structure, electrochemically inactive, although the olivine polymorph can be prepared from the lithium analogue. As alternatives, vanadium based cathode materials have been studied, such as the NASICON (Na Super Ionic CONductor) structure $\text{Na}_x\text{V}_2(\text{PO}_4)_3$ (NVP). NVP was initially synthesised by Delmas *et al.* [99] and exhibits interesting electrochemical properties; two plateaus are observed at 3.4 V and 1.6 V vs. $\text{Na}^+/\text{Na}^\circ$ associated with the $\text{V}^{4+}/\text{V}^{3+}$ and $\text{V}^{3+}/\text{V}^{2+}$ redox reactions, respectively, in total allowing the extraction of 1.7 Na. Studies made utilizing the window 2.7-3.8 V vs. $\text{Na}^+/\text{Na}^\circ$

have shown that it is possible to obtain a capacity of 93 mAhg⁻¹ with excellent cyclability [100]. We cycled NVP with our IL based electrolytes between 2.7-3.6 V vs. Na⁺/Na⁰ and obtained a capacity of *ca.* 80 mAhg⁻¹ at a C/10 rate. The voltage range had to be reduced due to the decomposition of the electrolyte at high voltages, hence the somewhat lower capacity.

Table 6. Some SIB cathode materials with potentials for sodium insertion and resulting specific capacities.

Cathode materials	Potential of insertion [V vs. Na ⁺ /Na ⁰]	Specific Capacity [mAhg ⁻¹]	Reference
NaCrO ₂	3.0	125	[95]
NaNi _{0.5} Mn _{0.5} O ₂	N/A	130	[43]
O3-NaVO ₂	2.5	120	[101]
Na _{0.33} V ₂ O ₅	1.5-4.0	142	[102]
Na ₃ V ₂ (PO ₄) ₃	1.6 & 3.6	93-116	[99, 103]
Na ₃ V ₂ (PO ₄) ₂ F ₃	3.7 & 4.2	120	[104]
NaFeF ₃	1.5-4.5	150	[105]
NaFePO ₄	2.5	120	[106]
NaMnO ₂	2.63	185-190	[107-109]
NaFeO ₂	3.3	85	[110]
Y-Fe ₂ O ₂	2.0	189	[80]
Na _{0.45} Ni _{0.22} Co _{0.11} Mn _{0.66} O ₂	4.2	135	[111]
Na _{0.67} Mn _{0.65} Fe _{0.2} Ni _{0.15} O ₂	2.0 & 3.8	208	[112]
NaNi _{0.5} Ti _{0.5} O ₂	3.1	121	[113]
Na ₂ Fe ₂ (SO ₄) ₃	3.8	100	[114]
Na ₂ FePO ₄ F	3	89	[115]
NaVPO ₄	3.3	98	[116]
Na(VO) ₂ (PO ₄) ₂ F	3.3, 3.6 & 4.0	105	[117]
Na ₃ MnCO ₃ PO ₄	3.7	191	[118]
Na ₄ Co ₃ (PO ₄)P ₂ O ₇	4.1-4.7	95	[119]
Na ₇ V ₄ (P ₂ O ₇) ₄ PO ₄	3.9	82	[120]
NaMnFe(CN) ₆	3.0	134	[121]

Na₃V₂(PO₄)₂F₃, or NVPF [122, 123], is a related 3D structure compound initially reported by Barker *et al.* [124] where VPO₄ was used as an intermediate phase (see Eq. 4).



The resulting crystal structure is a 3D framework of corner sharing (V₂O₈F₃) bi-octahedral and (PO₄) tetrahedral units connected through oxygen atoms. NVPF exhibits two plateaus at 3.7 and 4.2 V, thus on average 3.95 V, and these both correspond to the redox couple

V^{4+}/V^{3+} . The capacity observed is higher than for NVP, *ca.* 120 mAhg⁻¹ [104], and can thus be coupled to HC to build a promising full SIB with a larger energy density than so far reached for HC|NVP [21]. In III, NVPF is used as the cathode with organic solvent based electrolytes. In contrast to NVP, decomposition of the IL based electrolytes tested occurred with NVPF at potentials higher than 3.6 V vs. Na⁺/Na°. In the following sub-chapter the different types of electrolytes available and their impact on the electrodes and the SIB in total will be outlined.

2.3 Electrolytes

Electrolytes are just as important as the electrodes and an indispensable part of the SIBs. They usually consist of a combination of a sodium salt with a solvent or a solid – polymeric or ceramic, allowing the conduction of sodium ions from one electrode to another. For liquid electrolytes the ionic conductivity can be described by the Vogel-Tammann-Fulcher (VTF) [125-127] derived equation:

$$\sigma = \sigma_0 \cdot \exp\left(\frac{-B}{T-T_0}\right) \quad (4)$$

Where σ is the ionic conductivity, T_0 a temperature associated with the glass transition temperature (T_g), σ_0 is the ionic conductivity at T_0 , T is the absolute temperature, and B is the activation energy. As a comparison, polymers can follow either an Arrhenius (Eq. 5) or a VTF trend depending on the conduction mechanism [128, 129]. The Arrhenius equation:

$$\sigma = \sigma_0 \exp\left(\frac{-E_a}{k_B T}\right) \quad (5)$$

where σ_0 is the conductivity at infinite T , E_a is the activation energy, k_B the Boltzmann constant, and T the temperature.

σ can also be expressed as a function of the number of ions (n_i), their mobilities (μ_i), and their charge (q_i) (Eq. 6) – the equation of total conductivity:

$$\sigma = \sum_i n_i q_i \mu_i \quad (6)$$

The ionic conductivity is in practice expected to need to be > 1 mScm⁻¹ to facilitate ionic transport and acceptable rate capability, and the SIB electrolytes utterly need to show low electronic conductivities, act over a wide temperature range, and have large operative ESWs – ideally exceeding both insertion potentials of the electrodes. At last, it is also important that they exhibit generally appealing features for technological materials such as non-toxicity, environmental “friendliness”, and low cost [130]. There are several types of electrolyte concepts possible for SIBs, often based on the type of matrix used (Table 7).

Table 7. Comparison of different SIB electrolyte concepts.

	Liquid	Polymer	Gel Polymer	Ceramic	IL
Example	1M NaClO ₄ in EC:PC:DMC	NaTFSI in PEO	NaCF ₃ SO ₃ in Succinonitrile/PEO	Na-Zr-Si-P- O	NaTFSI in BMImTFSI
ESW [V vs. Na ⁺ /Na ^o]	1-(4-5)	1-(4-5)	N/A	1-8	1-7.5
Thermal stability	+	++	+++	+++	+++
Ionic conductivity @RT [mScm ⁻¹]	100-1000	0.1	1	0.3-1	1-10
Flammability	+	++	++	+++	++
Reference	[21]	[131]	[132]	[133]	[134]

The most common concept, the organic solvent based liquid electrolytes (LEs) can potentially be hazardous based on their flammability and leakage potential. Solid state electrolytes such as the ceramic β'' -Al₂O₃, widely used in high-temperature Na-S batteries, can potentially improve the safety for SIBs, while performing decently [135]. However, Na-S cells themselves, in contrast to SIBs, operate at 270-350°C and contain molten sulphur, sodium, and polysulphide compounds which are highly corrosive, can create toxic gases such as H₂S, and necessitates resistant containers, why this technology is inappropriate for transportation [136].

Gel polymer electrolytes (GPEs) in general consist of a high dielectric organic solvent containing a sodium salt, thus mainly a LE, immobilized in a polymer matrix host. Several GPE formulations have been reported where the poly(ethylene oxide) (PEO) [131] and poly(vinyl alcohol) (PVA) [137] based have received the most attention. The main advantage of GPEs lies in the improvements of the ionic mobility compared to “dry” solid polymer electrolytes (SPEs), due to the liquid-like conductivity mechanism. Moreover, compared to LEs, GPEs have superior mechanical properties, and can allow faster charge/discharging and higher power densities [138-140]. The main disadvantage as compared to LEs is the relatively low ion permeability due to the polymeric structure lowering the ion mobility [141, 142]. The main reason why LEs still dominates is the high conductivities: > 10 mScm⁻¹.

2.3.1 Organic Solvent Based Electrolytes

A solvent is by definition a substance which can dissolve another substance - the solute. For SIBs one or several organic solvents are used to dissolve a Na-salt to create a LE. Large dielectric constants (ϵ) of the organic solvents ease the salt dissolution [143, 144] and hence allow a larger concentration of metal cations to be present in the solution. In more detail, the degree of ion dissociation is dependent of the interaction strength between the cation, Li^+ or Na^+ , and the anion, carefully chosen in order to optimize the electrolyte and improve the conductance, and the cation-solvent interaction. The interaction between ions is by simple definitions inversely proportional to ϵ and a high ϵ solvent thus eases salt dissociation and increases the conductivity. As an example, the study of ion-ion interactions by Barthel *et al.* revealed that decreasing the interactions by 14% increased the conductivity by 440% [145]. Furthermore, comparing several sodium and lithium salts, it was shown by density functional theory (DFT) calculations [146] that going from Li to Na decreases the ion-pair dissociation energy by *ca.* 15-20%, thus Na based electrolytes based on the same salts should be more conductive than the Li analogues. This assumption is based on most charge carriers being metal cations (i.e. Li^+ , Na^+), suggesting also a high cation transport number (Eq. 7), but does not take into account different solvent shells *etc.*

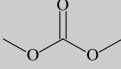
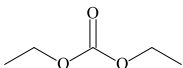
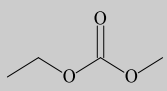
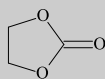
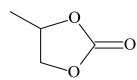
$$t_+ = \frac{\mu_+}{\mu_+ + \mu_-} \quad (7)$$

As the solvents arrange around Li^+/Na^+ creating a stable 1st solvation shell, the cations have lower ionic mobilities impacting on the total conductivity. Moreover, Li^+ and Na^+ are not necessarily coordinated similarly (III), [146]. Therefore, the benefit of a lower dissociation energy can be lost due to the formation of a different solvation shell. The solvation shell is characterized by a solvation number (SN), the number of solvents contributing, and the coordination number (CN), often the same as the SN, being the number of interacting atoms/groups. For instance, in LEs Li^+ usually has a CN of 4 [147-149], supported both by DFT calculations and experimentally, while Na^+ seems to have a slightly larger CN of *ca.* 6 in the same LE solvents (*c.f.* Table 8). Such low-level details influence the conduction of the charge carriers through the electrolyte and thus the general performance of the SIB cells.

Historically, in the 1980's, propylene carbonate (PC) was the most popular organic solvent for both LIB and SIB LEs, mainly due to its high dielectric constant (Table 8) and large thermal stability. However, to use PC with graphite for LIBs was shown to be problematic as PC co-intercalates in between the graphene sheets causing an irreversible exfoliation damaging the electrode structure [150]. Therefore, PC was replaced by ethylene carbonate (EC), which in contrast assists in the formation of a protective passive layer on the top of the graphite electrode avoiding any undesired structural modification —the solid electrolyte interphase (SEI) (section 2.4). However, EC cannot be used as a single electrolyte solvent due to its high melting point (*ca.* 36°C), and therefore usually mixed with linear or cyclic co-solvents (Table 8) with lower melting points. For SIBs, where HC replaces graphite as the

anode (section 2.2.1) PC can be used without damaging the electrode. Therefore, it is not surprising that PC still is present in *ca.* 60% of the electrolytes reported in research related to SIBs [22].

Table 8. Linear and cyclic solvents used in battery electrolytes.

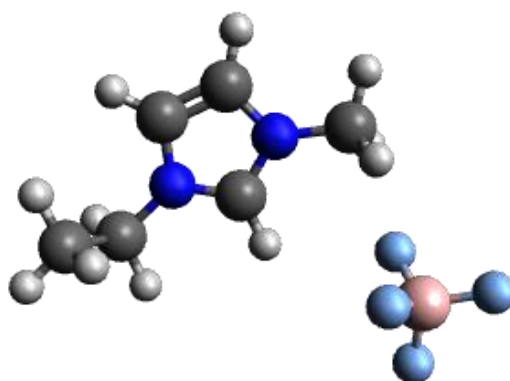
	Solvents	Melting Point (°C)	ϵ (25°C)	
Linear	Dimethyl carbonate DMC		5	3.1
	Diethyl carbonate DEC		-74	2.8
	Ethyl methyl carbonate EMC		-53	3.0
	Dimethoxyethane (G1) DME		-58	7.2
Cyclic	Ethylene carbonate EC		36	89.8
	Propylene carbonate PC		-49	64.9

SIB LEs use the sodium salts NaClO_4 , NaTFSI , or NaPF_6 dissolved in the solvents of Table 8 or others, for instance triglyme (G3) [72, 110, 151, 152]. Some compositions of these solvents, often binary or ternary, exhibit excellent properties and more details on their thermal stabilities, conductivities, viscosities and electrochemical stability windows can be found in the study by Ponrouch [153] (Table 9). For instance, Komaba *et al.* studied electrolyte formulations using 1 M of NaClO_4 in EC:DEC or EC:PC and proved these combinations to outperform EC:DMC and EC:EMC based LEs in terms of conductivity [43]. A similar study from Vidal-Abarca *et al.* [154] showed the EC:DEC combination to improve the battery cell capacity and cyclability compared to sole PC as solvent. PC alone is thus in general not recommended as the general performance such as the maximum capacity and capacity retention decreases, while a mixture of EC and PC or/and another solvent can set a stable environment for the battery cell. At last, a new electrolyte was recently proposed by Hu *et al.* [155]; 1 M of sodium bis(fluorosulfonyl)imide (NaFSI) in pure PC offering high storage performance for a HC|NVP cell.

Table 9. Conductivity (σ), viscosity (η), ESW, and thermal stability of common SIB electrolytes.

Electrolytes 1 M Na-salt	σ [mS.cm ⁻¹]	η [cP]	ESW [V vs. Na ⁺ /Na ⁰]	Thermal stability [°C]
NaTFSI – PC	6.2	7.4	0.1 – 3.4	
NaClO ₄ – PC	6.5	7.7	0.1 – 5.0	
NaPF ₆ – PC	8.0	7.7	0.1 – 5.0	-89 – 244
NaClO ₄ – G3	3.6	10.1	0.1 – 4.8	
NaClO ₄ – EC:DEC	6.4	5.1	0.1 – 5.0	-43 – 99
NaClO ₄ – EC:G3	6.7	8.4	1.0 – 4.5	
NaClO ₄ – EC:PC	8.2	9.1	0.1 – 5.1	-87 – 244
NaClO ₄ – EC:DMC	10.3	4.4	0.1 – 5.0	-14 – 65
NaClO ₄ – EC:DME	12.6	4.0	0.1 – 3.9	

2.3.2 Ionic Liquids

**Figure 8.** An ion pair of the IL BMImBF₄

Ionic liquids are defined as “salts with a melting point below 100°C”. ILs used as electrolytes are usually based on quaternary ammonium cations, and characterized by negligible vapour pressure and not flammable [156]. They exhibit high conductivities, wide liquid temperature ranges, large electrochemical windows, as well as many properties for safer application useful for any batteries [157, 158]. Room temperature ionic liquids (RTIL), having melting points below RT (Fig.8), have been extensively studied the last decade for ambient battery applications [158-162]. Still though, the room temperature performance of IL based electrolytes is less than encouraging and much reduced as compared to organic electrolytes even if the ionic conductivities reported seem appealing. Indeed, all ions present in the electrolytes are participating to the conduction, but it is the cation transport (*i.e.* Na⁺/Li⁺)

that is necessary for the cell cycling. At last, by the synthesis of sodium 2,5,8,11-tetraoxatridecan-13-oate (NaTOTO), an IL with a Na cation has been made [163, 164]

Caution has to be taken, however, on the “environmentally friendly” qualification which is overly used in the battery field to justify the presence of ILs in electrolytes. Indeed, to be qualified as environmental friendly, a chemical compound has to satisfy several criteria such as the energy to manufacture, the cumulative energy demand, the impact on health and environment among others. Unfortunately, ILs are often not greener than the solvents they are supposed to replace. For instance, BMImBF₄ needs more than 30 steps to be synthesised and waste such as hydrogen fluoride (HF) is created [165]. Another study using several criteria stated that ILs were the least environmental friendly solvents among 7 different solvents [166]. Therefore, ILs should be considered for their safety and electrochemical properties more than their environmental properties.

2.3.2.1 Ionic Liquid Based Electrolytes

For SIBs the use of ILs with a fraction of sodium salt as the electrolyte is at a very early stage of research, but certainly worth studying. Our review (IV) on SIB electrolytes can be consulted for more details [22]. Pyrrolidinium (Pyr) and imidazolium (Im) based RTILs stand out amongst the most used ILs as matrices for SIB electrolytes; starting with Pyr based ILs, Ding *et al.* [167] reported NaFSI in Pyr₁₃FSI (2:8) to have conductivities of 3.2 and 15.6 mScm⁻¹ at 298 and 353 K, respectively, and an anodic ESW limit of 5.2 V vs. Na⁺/Na⁰. The same group carried electrochemical tests [168] as capacity and rate capability of a Na/NaFSI in Pyr₁₃FSI/NaCrO₂ cell using an optimized salt/IL ratio of the electrolyte as cited above. Additionally, they characterized several Pyr type ILs for SIBs using the FSI and TFSI anions [169-171] and concluded that the FSI based had a higher oxidation potential limit. The electrochemical study of NaFSI in Pyr₁₃FSI cycled at 90°C with HC by Nohira *et al.*, revealed a reversible capacity of *ca.* 274 mAhg⁻¹, while maintaining 95.5% of the first discharge capacity after 50 cycles, with an impressive 99.9% coulombic efficiency [172, 173].

NaTFSI in Pyr₁₄TFSI has been studied by Noor *et al.* [174] reporting ionic conductivities of 1-2 mScm⁻¹ at RT, and an onset of the Na plating on a Cu electrode at -0.2 V vs. Na⁺/Na⁰ which can be explained by the high viscosity of the electrolyte (*ca.* 100cP) usually impacting the mass transport properties in IL based electrolytes. ²³Na NMR spectroscopy was used by the same group to characterize basic properties and specifically the ion transport of NaTFSI in Pyr₁₃FSI [175], and a cell with this electrolyte cycled vs. Na metal at temperatures up to 100°C with stable plating/stripping CVs on a Ni electrode. A different group also studied NaTFSI in Pyr₁₄TFSI [176] and reported a conductivity of 1 mScm⁻¹ in accordance with the previous results. This was complemented with a DSC analysis showing that the electrolyte remained liquid until -30°C. Moreover, in the introduction of a new IL, Pyr₂₄TFSI, was advertised for the near future.

Very recently, cyclability tests of 0.45 M NaTFSI in Pyr₁₄FSI [111], being composed of both TFSI and FSI anions, vs. a Na_{0.45}Ni_{0.22}Co_{0.11}Mn_{0.66}O₂ electrode in half cells against Na metal was shown to outperform a 0.5 M NaPF₆ in PC. This result was ascribed to the FSI anion assisting in the formation of a more stable SEI, (section 2.4.1) together with a higher stability at high potentials. Furthermore, effects of salt concentration (0.1 – 1 M) and rate variation (0.05 – 5 C) have been studied by Wongittharom *et al.* [177] using NaTFSI in Pyr₁₄TFSI, and revealed a promising capacity retention of 87% after 100 cycles, with the LE 1 M NaClO₄ in EC:DEC having 62% under the same conditions. Reducing the salt concentration to 0.5 M provided the same capacity retention at 50°C, which tentatively means that the charge carrier nature/balance is modified, as explained in **III** and **V**.

The other major class of ILs (Im based) was extensively studied in this thesis; basic physico-chemical properties comparing EMImTFSI and BMImTFSI ILs doped with NaTFSI and LiTFSI were investigated together with electrochemical properties useful for SIB application. A more detailed summary can be found in Chapter 4 as well as in **III** and **V**. In addition, a recent communication from Nohira's group [178] used NaFSI in EMImFSI to evaluate electrochemical and physical properties in a Na half-cell, and confirmed systems containing FSI anions to present wider ESWs in comparison to TFSI based, as previously shown for Pyr IL based electrolytes [169-171].

2.3.3 Hybrid Electrolytes

Organic solvents are highly flammable, presenting as safety risk, and ILs are usually highly viscous, with negative impact on the ionic conductivity (Eq. 4, section 2.3) [179]. Hybrid electrolytes with ILs as additives or co-solvents together with organic solvents appear to enable both safer electrolytes and high conductivities. While studies of hybrid electrolytes are at an early stage and mainly concern LIBs, the results are promising as performance and safety are truly improved [179-187]. Guerfi *et al.* [179] have shown that adding 40 % of EMImTFSI to a LE of 1 M LiPF₆ EC:DEC negatively impacts on the cycling performance for rates not exceeding 2C, but no significant conclusion was made on any safety improvements. Balducci's group [181, 185] carried out several experiments using Pyr₁₄TFSI as the IL together with LiTFSI in PC and showed these hybrid electrolytes to provide comparable performance to traditional LEs together with a better thermal stability. For SIBs, no studies have yet been made apart from **V**, where only 2 % of Pyr₁₃TFSI or BMImTFSI added was shown to increase the safety significantly.

2.4 Electrolyte/Electrode Interfaces

The performance of a battery can be improved by developing new electrode materials and hundreds of such articles are published every year [9, 66, 92, 93, 188-191]. However, the exclusive optimisation of electrodes is not enough to build a successful cell with improved performance. While the high capacities associated to LIBs or SIBs strongly depend on the architecture and electronic behaviour of the electrodes, the side reactions taking place at the electrode/electrolyte interfaces can be the cause of low capacities and low coulombic efficiencies. Usually, the theoretical limits of the ESW are defined by the lowest unoccupied molecular orbital (LUMO) and the highest occupied molecular orbital (HOMO) of the electrolyte. However, passivation layers formed on the surfaces of the electrodes can kinetically extend these thermodynamic limits and increase the operative ESW (Fig. 9) The next two sections will highlight the importance of the electrolyte/electrode interfaces.

2.4.1 The Solid Electrolyte Interphase (SEI) and the Solid Permeable Interface (SPI)

The SEI is a thin protective passivation layer [192] exclusively formed at the anode/electrolyte interface by electrolyte decomposition in contact with the reducing anode surface. The SEI is usually formed during the first charge/discharge cycle and stabilized during the following 10-20 cycles. An efficient SEI should be permeable for the charge carrying ions (Li^+ , Na^+) while preventing any further electrolyte reduction by being electronically insulating.

The understanding of the SEI is complex and laborious even though many studies have been done for LIBs [192, 193]. Still there is no absolute parameter in order to normalize or generalize the composition of the SEI; its properties, quality, and efficiency are dictated by a combination of factors, as described in the review by Verma *et al.* dealing with SEIs of LIBs [193]. In this review, major components of the SEI regularly observed are listed and seem to be inorganic in the major part. Therefore, the reduction of the salt may form SEI components such as $(\text{CH}_2\text{OCO}_2\text{Li})_2$ [194, 195], ROCO_2Li [194, 195], Li_2CO_3 [194, 196], Li_2O [195], polycarbonates [197], LiOH [198], *etc.*

Recently, some studies of SIB SEIs have been also reported [21, 43, 72, 153, 199-201], but yet it is too early to really identify clear useful trends on how to form a stable SEI. However, some striking differences as compared to LIBs have been identified using several techniques. XPS combined with TOF-SIMS on a fully sodiated or lithiated HC electrode using 1 M NaClO_4 in PC revealed similar SEI compounds for LIB and SIB cells, with differences in the proportion of inorganic compounds, significantly larger for the latter [154]. Using the same technique the addition of EC in the electrolyte increased the quantity of C-O environment of carbon in the SEI due to the ring opening of EC with formation of PEO oligomeric/polymeric species [202], while presence of DMC did not modify the SEI composition. SEIs of non-carbonaceous

negative electrodes have been found to have similar compositions as for carbonaceous negative electrodes [203]. Komaba *et al.* [43] has shown using SEM that the SEIs formed on HC using 1M NaClO₄ as the electrolyte had larger unevenly distributed particles on the surface than the SEI formed using 1 M LiClO₄ and an XPS analysis revealed the surface layer to be thinner while mass spectroscopy showed the chemical composition to differ. Another XPS analysis from Philippe *et al.* for SEIs formed on Fe₂O₃ using NaClO₄ or LiClO₄ in EC:DEC showed the former SEI to be more homogeneously distributed, while both were similar in thickness and composition.

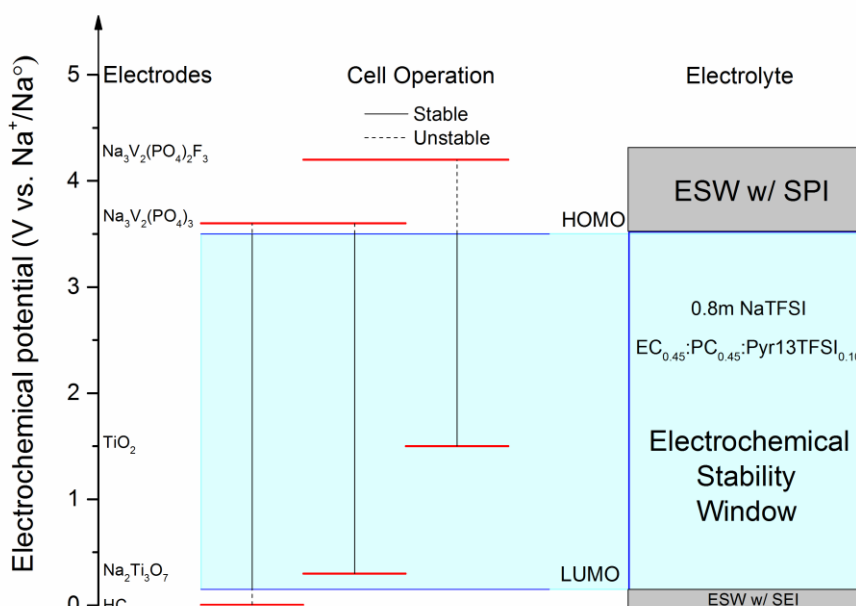


Figure 9. Schematic representation showing the difference between the intrinsic electrolyte ESW and the extended ESW due to the electrode/electrolyte interfaces.

Electrode passivation does not exclusively occur on the anode side; the positive electrode may also need a protective mechanism in order to stabilize the whole cell when operating at high potentials – an SPI. Comparatively less attention has been paid to the SPI in comparison to the SEI despite its similar vital role [204-210]. LIBs and by association SIBs are using cathodes with high insertion potentials often exceeding the oxidation potential of the electrolyte. Thus it is crucial to understand and develop methods to stabilize SPIs (Fig.9).

In order to minimise the electrolyte decomposition and improve the capacity retention, different techniques to improve the SPI have been reported, primarily for LIBs. Coating the cathode grains by encapsulating them with inorganic or organic phases was proven successful for LiMn₂O₄, this minimizes the surface area of active material in direct contact with the electrolyte [211-213]. For LiCoO₂ a coating layer of ZrO₂ was applied to improve the rate performance [214].

2.5 Safety Concerns

In order to commercialize a battery, a manufacturer has to deal with many different safety concerns; if the specifications in terms of toxicity, flammability, and chemical stability are not fulfilled the product cannot be commercialized. Most of us enjoy technologies such as smartphones, tablets and electric cars in spite of the potentially hazardous chemicals contained inside the batteries. Indeed, the attractive high density energy of LIBs and SIBs may backfire in case of a leakage, electrical, or other kinds of failure.

Starting with overcharging events *i.e.* when cells are inadvertently charged to a higher than specified voltage, batteries with intercalation materials at the cathode side may be “delithiated” by the absorption and storage of the overcharged energy. The positive electrode active material may become unstable, decompose, and a large quantity of heat released. This may cause the ignition of any flammable solvent present such as the organic solvents of the electrolyte, followed by other materials. This issue is usually well managed in commercial LIBs as the charging is well controlled; if a cell is overcharged, it is disconnected automatically from the rest of the battery to avoid any further complications.

Over-heating is, however, a serious issue for all batteries. Three major scenarios can cause this phenomenon; the cell can be exposed to high external temperatures, the cell can create abnormal resistive heating (I^2R) during cycling, and short circuit may occur. As soon as the temperature exceeds 100°C the SEI (section 2.4.1) is dissolved and the electrolyte is consumed on the anode side of the cell causing a thermal runaway. In the best case, the reaction will be contained within the cell packaging, while in worst case a cell fire or explosion occurs. The main problem in a large battery pack such as for EVs is the proximity of the cells; if one cell goes into a thermal runaway, the event can propagate to the next closest cells resulting in an even more severe failure and event.

Mechanical abuse is in general caused by crushing or penetration. This may happen during transportation, road accidents, or during the installation of a stationary battery due to mishandling. Mechanical abuse usually causes short circuits, thus leading to over-heating.

To estimate the safety of the SIB, our measurements were focused on the electrolyte flammability. Avoiding, delaying, or shortening electrolyte ignition would greatly reduce the probability of flame propagation to the whole battery pack. The flash point (FP) gives an indication on the temperature necessary to ignite the electrolyte vapours. The higher the FP, the safer is the electrolyte. Delaying the ignition can be important as a safety margin after e.g. an accident – thus the ignition time (IT) is valuable to know. At last, the self-extinguishing time (SET) defines the time needed for a created flame to die out, a reduced SET means a safer electrolyte.

3 Experimental Methods

The methods presented here have all been extensively used to characterise the materials and their resulting properties important for battery application. Dielectric spectroscopy, differential scanning calorimetry (DSC), and Raman spectroscopy have been performed at Chalmers in order to gain a better understanding of the ionic conductivities, the thermal windows, and the molecular interactions occurring in the electrolytes. The three other techniques presented; microwave (MW) synthesis, cyclic voltammetry (CV), and galvanostatic cycling with potential limitation (GCPL), have been carried out at ICMA-B-CSIC to learn more about the electrochemical properties: the electrochemical stability windows (ESWs), the specific capacities, and the battery cycling stability. In addition, safety measurements were carried out at Chalmers to determine the FPs, SETs and ITs of the electrolytes.

3.1 Dielectric Spectroscopy

The purpose of dielectric spectroscopy is to measure the complex dielectric function, presented in Eq. 7, in the broadband frequency range 10^{-6} - 10^{12} Hz [215-217], using a capacitor cell with a complex capacity C^* made of two brass electrodes separated by a Teflon spacer (Fig. 10).

$$\varepsilon^*(\omega) = \varepsilon'(\omega) - i\varepsilon''(\omega) = \frac{C^*(\omega)}{C_0} \quad (8)$$

$\varepsilon'(\omega)$ and $\varepsilon''(\omega)$ are the real and imaginary parts of the complex dielectric function, ω is the angular frequency, C_0 is the vacuum capacitance, while T corresponds to the time for one period:

$$\omega = 2\pi\nu = 2\pi T^{-1} \quad (9)$$

When a sinusoidal electric field $E_1^*(\omega)$ is applied to the cell, the resulting electric field of the sample $E_s^*(\omega)$ is collected, but with a different direction. The current $I_s^*(\omega) = I_0 \exp(i\omega t + \phi)$ (ϕ being the phase) measured gives information on the polarization effects, while the phase difference between $E_1^*(\omega)$ and $I_s^*(\omega)$ is explained by the time necessary to orient dipoles in the studied sample. Therefore, knowing both resulting sample current and potential, it is possible to define the complex impedance as:

$$Z_s^*(\omega) = \frac{U_s^*(\omega)}{I_s^*(\omega)} \quad (10)$$

Knowing that $C^*(\omega)$ can be expressed as:

$$C^*(\omega) = \frac{1}{i\omega Z^*(\omega)} \quad (11)$$

a new expression of $\varepsilon^*(\omega)$ can be derived, proportional to $Z_s^*(\omega)$ by combining (8), (10), and (11):

$$\varepsilon^*(\omega) = \frac{1}{i\omega Z_s^*(\omega) C_0} \quad (12)$$

It is also possible to derive the ionic conductivity from $\varepsilon^*(\omega)$ using the current density $J_s^*(\omega)$ and the electric field $E_s^*(\omega)$ knowing that C_0 can be expressed as:

$$C_0 = \varepsilon_0 \frac{A}{L} \quad (13)$$

with A the electrode surface area and L the distance between the electrodes. Thus, the impedance can be written as:

$$Z_s^*(\omega) = \frac{E_s^*(\omega) \varepsilon_0}{J_s^*(\omega) C_0} \quad (14)$$

Combining (10) and (12) gives:

$$\varepsilon^*(\omega) = \frac{J_s^*(\omega)}{i\omega \varepsilon_0 E_s^*(\omega)} \quad (15)$$

At last, the ionic conductivity of the sample can be derived from (15) as:

$$\frac{J_s^*(\omega)}{E_s^*(\omega)} = \frac{I_s^*(\omega) A}{U_s^*(\omega) L} = \sigma^*(\omega) = i\omega \varepsilon_0 \varepsilon^*(\omega) \quad (16)$$

The studies of the ionic conductivities were made over a wide temperature range; increasing the temperature amplifies the random thermal motion of the molecules. Additionally, the dipole alignment with the electric field will deviate more resulting in less orientation polarisation of the material. Therefore, a modification of the conductivity will be observed due to its proportionality to the dielectric function. An equilibration time is necessary to obtain consistent results; if the temperature is not stabilized and the equilibration time is too short, the dipoles will not reach their final orientation.

3.1.1 Data Interpretation

Once $Z_s^*(t)$ and $\epsilon^*(\omega)$ have been obtained, it is possible to differentiate between three different processes:

- Microscopic fluctuations of molecular dipoles [218]
- The propagation of mobile charge carriers; diffusion of electrons, holes, or ions [219].
- The separation of charges at interfaces; polarisation [219].

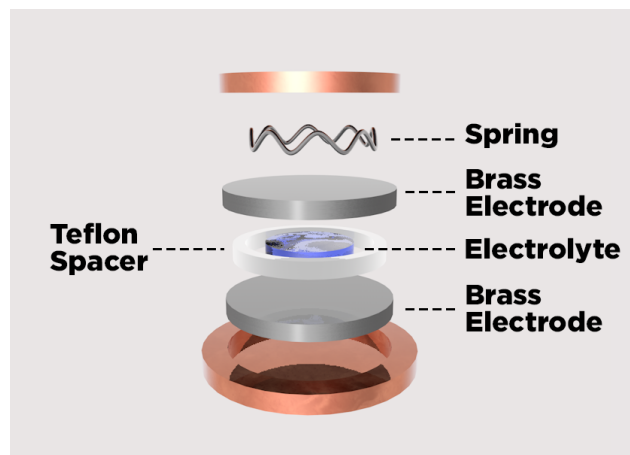


Figure 10. Dielectric spectroscopy cell used for all measurements in II and III.

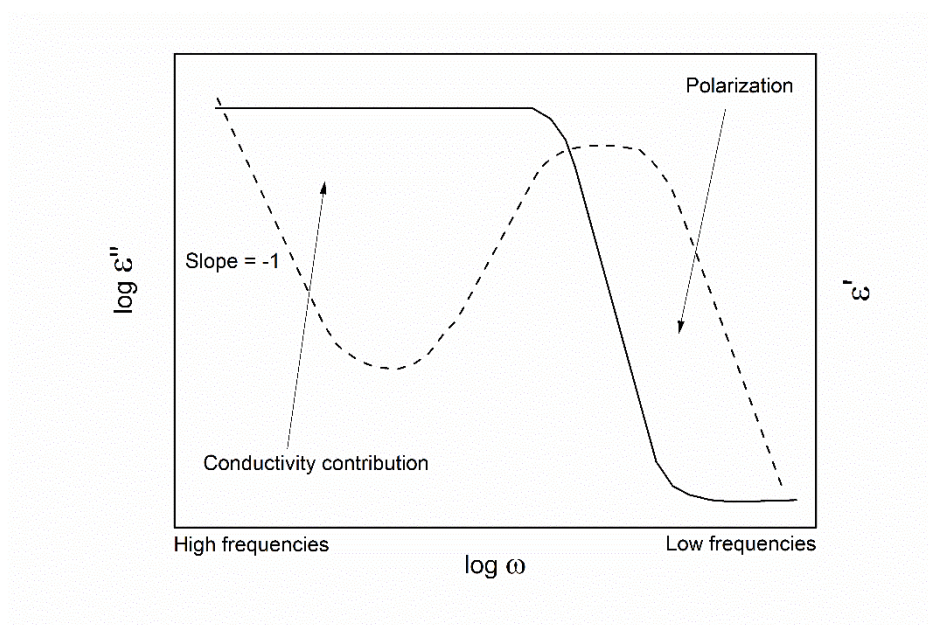


Figure 11. Variation of the real part $\epsilon'(\omega)$ (solid line) and the imaginary part $\epsilon''(\omega)$ (dashed line) of the complex dielectric function.

Pure conduction phenomena e.g. the ionic conductivity of the electrolyte defined above, can be obtained by monitoring the frequency dependence of the real part of $\epsilon^*(\omega)$, i.e. ϵ' (Fig. 11). Practically, the ionic conductivity or DC conductivity is defined as the constant plateau value of $\epsilon'(\omega)$ while the polarization contribution can be found at low frequency.

The temperature dependence of the ionic conductivity from 273 to 333 K as function of the frequency is shown in Fig. 12. The plateaux observed in each measurement is clearly modified with the temperature supporting the temperature dependence of the dielectric properties.

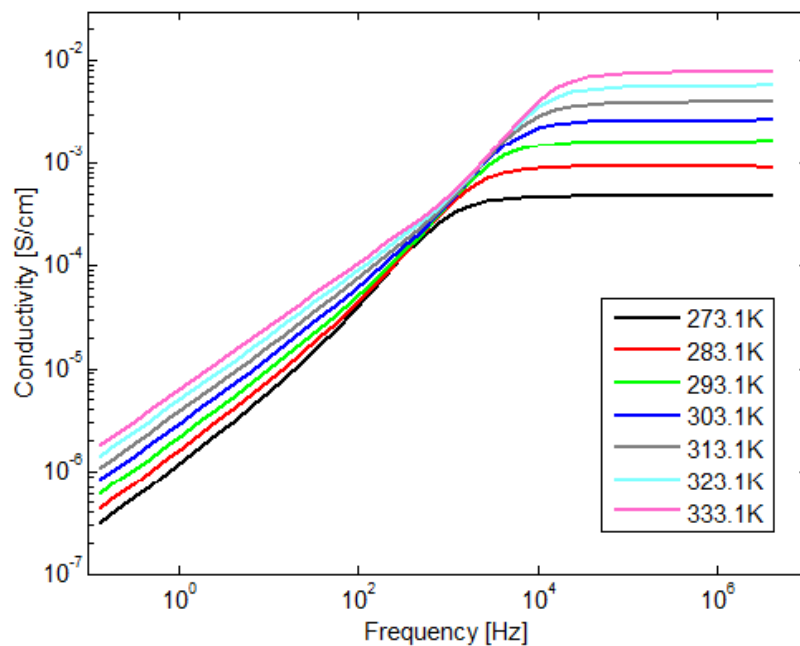


Figure 12. Conductivity vs. frequency for different temperature of NaTFSI in BMImTFSI.

After collecting the conductivity for each temperature (Fig. 11), the conductivity can be presented as functions of the inverse of the temperature. This representation is commonly used in the battery field as the trend usually follows a well-defined path. For instance, for a LE the trend follows a VTF behaviour (section 2.3), while polymers can follow either an Arrhenius (Eq. 16) or a VTF trend depending on the conduction mechanism [128, 129]. In this thesis, studies were carried on LEs having VTF behaviour (Fig. 13).

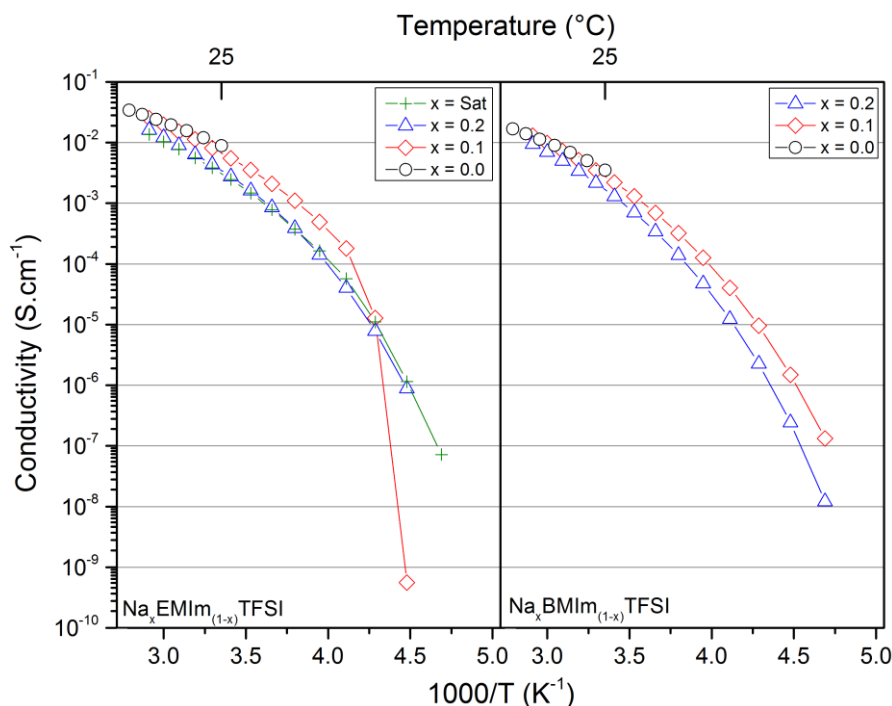


Figure 13. Ionic conductivity results for $\text{Na}_x\text{EMIm}_{(1-x)}\text{TFSI}$ and $\text{Na}_x\text{BMIm}_{(1-x)}\text{TFSI}$ for different molar fractions ($x = 0, 0.1, 0.2$, and saturated).

3.2 Raman Spectroscopy

Even if inelastic scattering of light was predicted by Adolf Smekal already in 1923 [220], it was not observed in practice before 1928 by C. V. Raman [221]. The therefore named Raman spectroscopy relies on inelastic scattering of light in the visible, near infrared, or near ultraviolet wavelengths and how photons, today often from a laser, interact with the vibrational states of the material – often molecules.

3.2.1 Theory of Raman Scattering

Two types of theories can be used to explain the Raman scattering: the classical and the quantum. The classical considers light as an electromagnetic radiation containing an oscillating electric field that interact with a material (*e.g.* molecules) due to its polarizability, while the quantum considers light as photons which hits molecular bonds creating inelastic scattering.

3.2.1.1 Classical Wave Interpretation

Vibrational spectroscopy is a mutual term to describe Raman and infrared spectroscopy (IR). Both techniques are non-destructive, they provide information on the molecular composition, structure and interactions of the studied sample. Each chemical bond can be characterized by the measures of vibrational energy levels that can be transcribed into a unique spectrum equal to a fingerprint. Therefore, vibrational spectroscopy is extremely useful to identify, characterise, and monitor reactions for a sample of any shape as long as it is active in Raman or IR.

The simplest model for vibrations, for a diatomic molecule, is two masses m_1 and m_2 connected by a weightless spring with a stiffness constant k (Fig. 14).

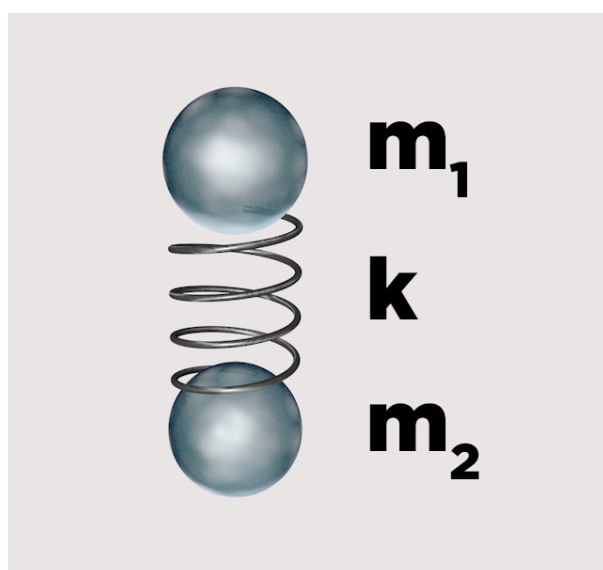


Figure 14. Schematic of two masses m_1 and m_2 connected by a weightless spring with a stiffness force k .

If a force F is applied to move the masses a distance x from their position of equilibrium this is proportional to the constant k , Hooke's law:

$$F = -kx \quad (17)$$

The negative sign is added as the force F always is in the opposite direction of the elongation. When combined with Newton's law, we obtain:

$$m \frac{d^2x}{dt^2} = -kx \quad (18)$$

Furthermore, the resolution of the second order differential equation can be written:

$$x = x_0 \cos(2\pi\nu t + \varphi) \quad (19)$$

with x_0 being the amplitude, ν the frequency of the movement, and φ the phase constant. Eq. 19 describes a sinusoidal movement relating a displacement x to a vibrational frequency.

Considering that the second derivative of x is:

$$\frac{d^2x}{dt^2} = -4\pi^2\nu^2 x_0 \cos(2\pi\nu t + \varphi) = -4\pi^2\nu^2 x \quad (20)$$

A combination with Eq.20 yields:

$$4\pi^2\nu^2 m = k \quad \text{or} \quad \nu = \frac{1}{2\pi} \sqrt{\frac{k}{m}} \quad (21)$$

This frequency of vibration, however, involves only one mass attached to a very large mass connected by a spring. For our diatomic model, the *reduced mass* has to be introduced with the masses m_1 and m_2 instead of m :

$$\frac{1}{m} = \frac{1}{m_1} + \frac{1}{m_2} \quad (22)$$

Thus, the vibrational frequency of a diatomic molecule is:

$$\nu = \frac{1}{2\pi} \sqrt{k \left(\frac{1}{m_1} + \frac{1}{m_2} \right)} \quad (23)$$

To summarize, this model is describing systems such as molecules vibrating in sinusoidal pattern with a frequency proportional to the bond strength and inversely proportional to the *reduced mass*.

3.2.1.2 Quantum Particle Theory

When a light quantum $h\nu_0$ hits a molecule, there is a high probability that an elastic scattering process occurs by emitting back the exact same amount of energy, *i.e.* $h\nu_0$; Rayleigh scattering. On the other hand, if the exchange process of vibrational energy is inelastic, a different quanta of energy is emitted as $h\nu_0 \pm h\nu_s$; Raman scattering. Therefore, the origin of the modified frequencies in Raman is explained by the interaction between a system and a radiation of wavenumber ν_0 making an upward transition from a lower energy level E_0 to an upper energy level E_1 or the opposite (*i.e.* from E_1 to E_0). Each transition passes through an intermediate level; the excited state or the virtual state. If the molecules leaves a quantum of lower energy ($h\nu_0 - h\nu_s$) the process is called Stokes scattering (with reference to Stoke's work on fluorescence [222]), and for a quantum of higher energy ($h\nu_0 + h\nu_s$) the process is called anti-Stokes scattering (Fig. 15).

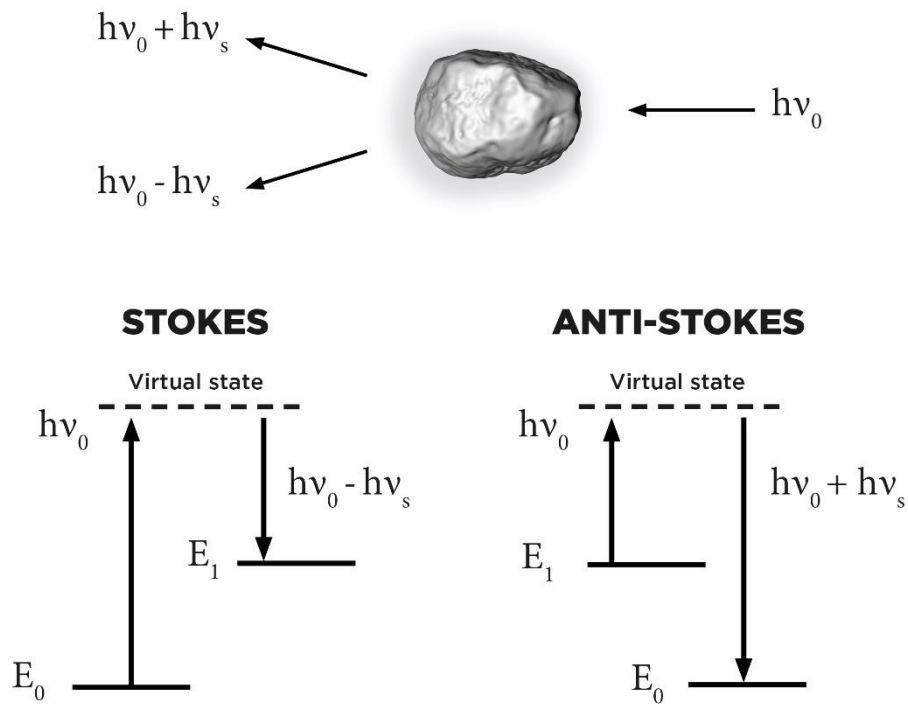


Figure 15. Description of the Stokes and anti-Stokes processes, where E_0 and E_1 are vibrational modes while $h\nu_0$ and $h\nu_s$ are photon energies.

It is possible to corroborate the quantum Raman effect to classical physics as follows: an incident monochromatic light involves an electric field strength E fluctuating with time t :

$$E = E_0 \cos(2\pi\nu_0 t) \quad (24)$$

where E_0 is the amplitude and ν_0 is the laser frequency which can be used to irradiate a molecule and induce an electric dipole moment P :

$$P = \alpha E = \alpha E_0 \cos(2\pi\nu_0 t) \quad (25)$$

with α being the polarizability. The nuclear displacement q when the molecule vibrates with a frequency ν_s can be expressed as:

$$q = q_0 \cos(2\pi\nu_s t) \quad (26)$$

where q_0 is the vibrational amplitude. If the amplitude of vibration is minute, α is a linear function of q , and can be expanded in a Taylor series:

$$\alpha = \alpha_0 + \left(\frac{d\alpha}{dq}\right)_0 q_0 + \dots \quad (27)$$

Combining (25), (26) and (27) with the use of trigonometry identity the electric dipole moment can be written as:

$$P = \alpha_0 E_0 \cos(2\pi\nu_0 t) + \frac{1}{2} \left(\frac{d\alpha}{dq}\right)_0 q_0 E_0 [\cos(2\pi(\nu_0 + \nu_s)t) + \cos(2\pi(\nu_0 - \nu_s)t)] \quad (28)$$

The first term corresponds to the oscillating dipole of frequency ν_0 (Rayleigh scattering), while the second term holds both the Raman scattering of frequency $\nu_0 + \nu_s$ (anti-Stokes) and $\nu_0 - \nu_s$ (Stokes). Thus it also follows that if $\left(\frac{d\alpha}{dq}\right)_0$ is zero, the vibration is not Raman active, which is therefore the selection rule for Raman spectroscopy. At last, small perturbations of the vibrations can be seen as shifts in frequency, why also local environment changes and weaker interactions than covalent bonds can be probed by Raman spectroscopy.

For IR a vibrational mode is allowed if a change in the dipole moment is possible, this does not necessarily imply the presence of a permanent dipole as the rule is valid for a dipole moment modification. IR and Raman are thereby complementary techniques. For instance, if a molecule has a centre of symmetry, modes which are Raman active would be IR inactive and *vice-versa* (e.g. CO₂). Moreover, some molecules may be both IR and Raman active. That said, a mode being active in IR or Raman does not necessarily means that it can be analysed as some signals may be intrinsically too weak to be observed even if allowed.

3.2.2 Molecular Vibrations

The total energy in any molecule includes translational, rotational, and vibrational energies. Starting with the translational energy, a molecule can freely move toward an orthonormal space where three vectors are 90° to each other leading to three degrees of freedom. This is equally true for rotational energies which can also be described in three degrees of freedom, with the exception of linear molecules only having two degrees of rotation as the linear rotation around its molecular axis cannot be observed. Any other degree of freedom is related to vibrational energies, which then can be calculated to be totally 3N-6 for any nonlinear molecule containing N atoms and 3N-5 for linear molecules.

Each corresponding vibration is called normal mode or vibrational mode verifying several assumptions: the vibration of atoms in the molecules have the same frequency while their simultaneous displacement does not affect the mass centre, the amplitude of different particles can be different, the vibrational modes do not interfere with each other, and the number of modes is limited to 3N-6 or 3N-5. Every mode has its own pattern as presented in Table 10 and the identification of vibrational modes allows the characterisation of bonds within a molecule. If a vibrational mode is somehow modified by the environment, this will be observable as a shift in frequency in the spectrum.

Table 10. Molecular vibration modes with their characteristics. The + and - signs correspond to movements vs. the plane.

Modes	Stretching		Bending			
Description	Change in the length of a bond		Change in the angle between the bonds			
Types	asymmetric	symmetric	Rocking	Scissoring	Wagging	Twisting
Representation						
Nomenclature	ν_a	ν_s	ρ	δ	ω	τ

3.2.3 Raman Data Interpretation

A typical Raman spectrum from an hybrid electrolyte of 0.8 m NaTFSI in EC:PC:IL is the result of interactions between the sodium cations, TFSI anions, and solvent molecules, and expressed with the x-axis in wavenumbers and the y-axis in Raman intensity (Fig. 16). As each vibrational mode depends on the atomic masses and the strength of the chemical bond between them they can be used as fingerprints of the molecular structure. Overall, contributions of light atoms in bonds such as C-H, C-O or N-H will appear in the high wavenumber region, and as an example N-H stretching vibrations will always have higher frequencies than the C-H stretching vibrations. Similarly, all functional groups/bonds/vibrations can be localised and analysed based on their vibrational frequency in the Raman spectra. Some characteristic wavenumbers of common functional groups are presented in Table 11.

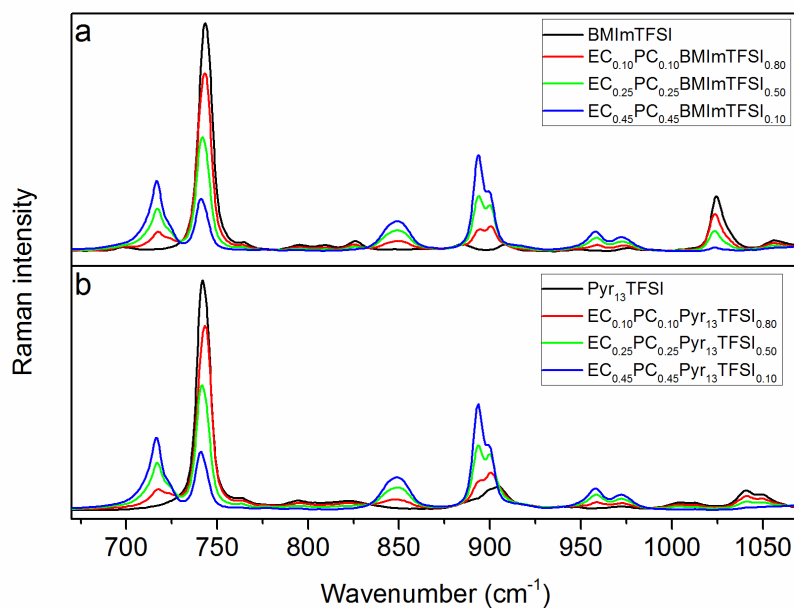


Figure 16. Raman spectra of (a) $EC_x:PC_x:BMImTFSI_{(1-2x)}$ and (b) $EC_x:PC_x:Pyr_{13}TFSI_{(1-2x)}$, between 675-1075 cm^{-1} .

Table 11. Functional groups/vibration modes and their approximate positions in a Raman spectrum.

Functional Group/Vibration Mode	Wavenumber (cm^{-1})
$\nu(C-H)$	2800 – 3000
$\nu(=C-H)$	3000 – 3100
$\nu(C=C)$	1500 – 1900
$\nu(N-H)$	3300 – 3500
$\nu(C=O)$	1680 – 1820
$\nu(S-S)$	430 – 550
$\nu(C-Br)$	500 – 700

All Raman spectra from condensed matter consist of peaks with band widths due to the temperature and thereby resulting slightly different interactions within the sample (in contrast to gases with almost no such interactions). Interpretation complications appear when two or more peaks overlap (Fig. 17). Then deconvolution and fitting techniques have to be used to reveal the contributions from each of the peaks. In our work, the mathematical Voigt function (Eq. 29) [223], which is a convolution of a Lorentzian and a Gaussian profile, has been applied to analyse Raman spectra and extract areas, peak heights, as well as the full width at half maximum (FWHM). The rationale for the choice of a Voigt profile is that the use of a Gaussian or Lorentzian function alone may not appropriately match the bands. In a system composed of molecules, the vibrational frequencies are influenced by the environment. The position, behaviour, and interactions between each molecules result in different broadening and/or line-shape profiles. Two main parameters can be used; the coherence lifetime, τ_c , corresponding to the time interval within which the phase from a vibrating molecule is predictable, and the amplitude

correlation time, τ_a , which is the interval of time necessary for a molecule to fully relax [224].

If the relaxation time is much shorter than the time interval necessary to predict the phase of a vibrating molecule (*i.e.* $\tau_c \gg \tau_a$), the line-shape will be a Gaussian profile. This is usually the case for molecules in a solid where the environment is not in motion while the molecules are separated by well-defined distances. If the relaxation time is much shorter than the time interval necessary to predict the phase (*i.e.* $\tau_c \ll \tau_a$), the line-shape will be a Lorentzian profile. It usually occurs within gases where the molecules are quickly moving, colliding, and rotating. At last, liquids are in between these two cases. Indeed, molecules in liquids are not located at fixed positions, while their motions are hindered by their interactions. In this case, τ_a and τ_c are relatively similar, resulting into a broadening having both Gaussian and Lorentzian line-shape contributions, hence justifying the use of Voigt profiles for the Raman spectra analysis.

Line broadening can be also influenced by instrumental or atmospheric effects. The use of a monochromator with rectangular slits results in a Gaussian profile [225]. In general, this effect does not have a large influence on the line broadening for a liquid as the convolution of two Gaussians is a Gaussian. Doppler broadening may also influence the line shape with an additional Gaussian contribution [226].

$$V(x) = \frac{\left(\frac{\omega_L}{\omega_G}\right)}{\pi^{3/2}} \int_{-\infty}^{\infty} \frac{e^{-(x'/\omega_G)^2}}{(x-x')^2 + \omega_L^2} dx' \quad (29)$$

ω_L and ω_G are two normalized expressions of the Lorentzian and the Gaussian profiles where:

$$\frac{\omega_L}{\omega_G} \equiv \sqrt{\ln 2} \frac{\Gamma_L}{\Gamma_G} \quad (30)$$

with Γ_L and Γ_G being the FWHM of the Lorentzian and the Gaussian profiles, respectively.

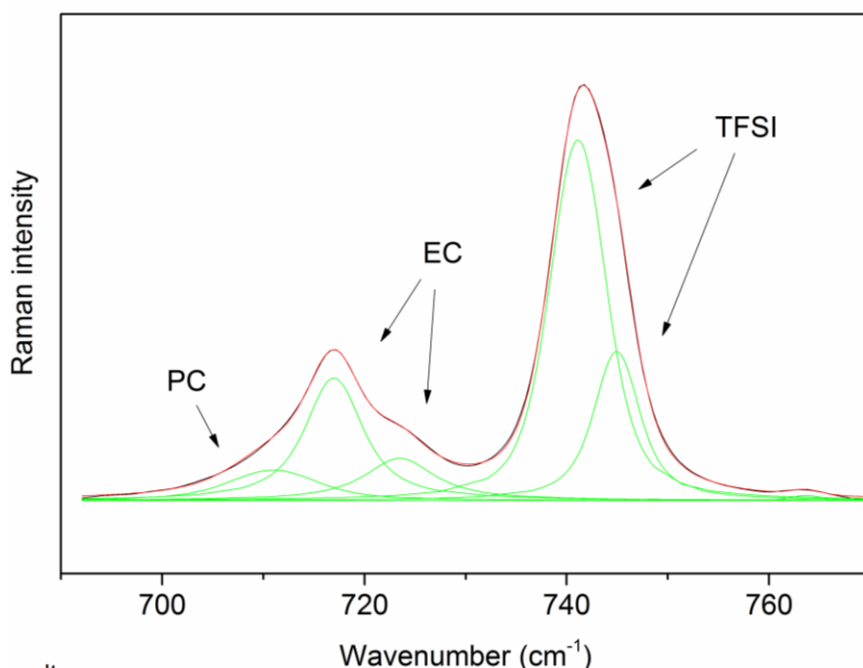


Figure 17. Deconvolution and fitting of peaks of TFSI, EC, and PC between 680-770 cm^{-1} using Voigt profiles. The red line is the experimental Raman data and the green lines are the resulting individual peaks from the fitting procedure.

3.3 Differential Scanning Calorimetry (DSC)

Calorimetry is the science of analysing the evolution of chemical reactions, physical changes, or phase transitions through the measurement of heat exchange. The generation or consumption of heat is analysed in order to understand physical processes. Here we apply calorimetry to obtain several measures of importance for a fundamental understanding of our materials; glass transitions, melting, and crystallization temperatures.

3.3.1 Theoretical Foundation

Calorimetry analysis using DSC is a thermo-analytical analysis that associate the temperature and heat flows to material phase transitions as function of time and temperature. The set-up of a DSC chamber is represented in Fig. 18. During an experiment, energy is transmitted simultaneously into the sample cell containing the sample and a reference cell, which in our case is an empty sealed aluminium pan. The difference of energy between the sample and the reference to match temperatures represent the amount of excess heat absorbed or released by the sample. An alternative view is that a DSC measurement monitors how the heat capacity (C_s) of the sample changes with temperature. In general, the sample holder temperature increases linearly as a function of time defined by the heating rate (*e.g.* $10^\circ\text{C min}^{-1}$ in III) and monitored by the furnace temperature (T_F).

As soon as the furnace is subject to a defined heating rate, heat flows from the furnace to the sample (ϕ_{FS}) and reference (ϕ_{FR}). The temperature difference ΔT should equal zero as the sample and the reference are heated equally. A differential signal is generated when the state equilibrium is disturbed by a physical transition modifying ΔT and therefore the heat flow (dQ_s/dt):

$$\frac{dQ_s}{dt} = \frac{(T_s - T_R)}{\lambda} \quad (31)$$

with T_R and T_s the temperatures of the furnace and the sample, respectively, and λ the total thermal resistance.

The heat flow to the sample can also be written as:

$$\frac{dQ_s}{dt} = C_s \left(\frac{dT_s}{dt} \right) - \left(\frac{dH_s}{dt} \right) \quad (32)$$

where C_s is the heat capacity of the sample together with the pan and H_s is the sample enthalpy.

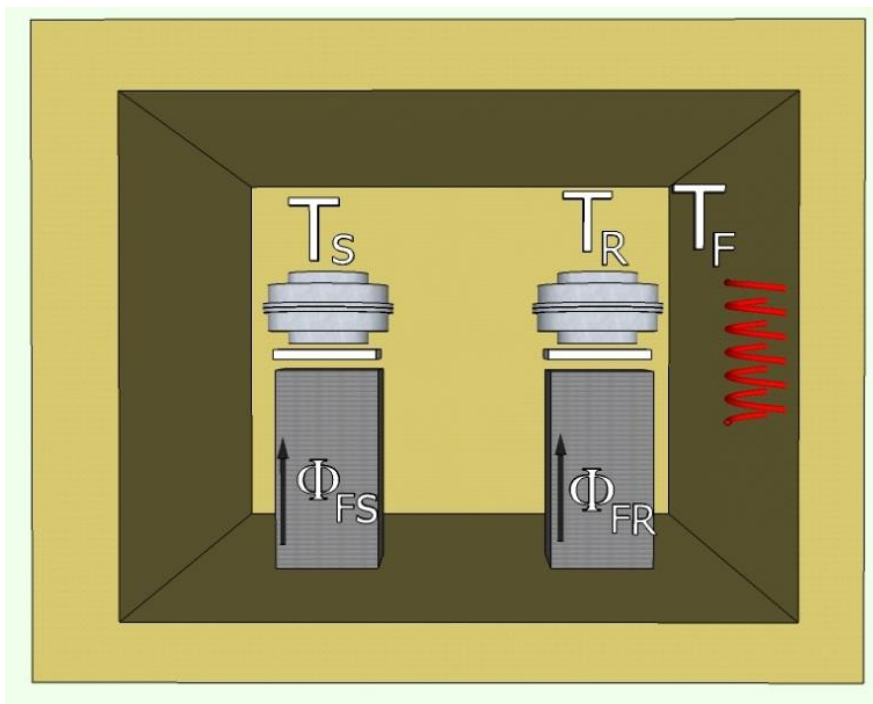


Figure 18. Illustration of a DSC chamber with T_s , T_R , and T_F the temperatures of the sample, reference, and furnace, respectively. ϕ_{FS} and ϕ_{FR} are the heat flow rates from the furnace to the sample, and from the furnace to the reference, respectively.

3.3.2 DSC Data Interpretation

In Fig. 19 a DSC trace of an IL based SIB electrolyte from III is displayed, within which three main features can be observed; the glass transition temperature, the melting temperature, and the crystallization temperature. The glass transition can be observed as a slight modification of the base line, corresponding to the transition between the liquid phase and the solid-like or glass phase where a change of heat capacity occurs. The more pronounced peaks are ascribed to crystallisation (exothermic) and melting (endothermic) processes. The integrated area of the peaks can be used to determine the enthalpy of each process.

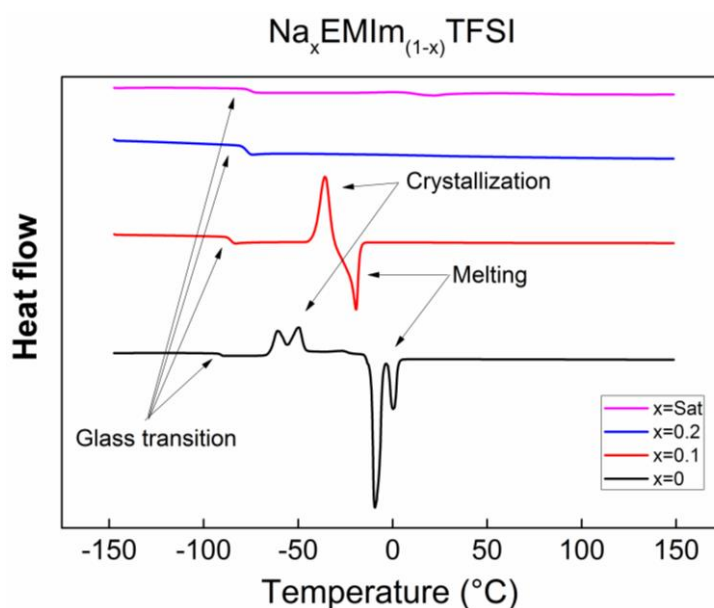


Figure 19. DSC traces of $\text{Na}_x\text{EMIm}_{(1-x)}\text{TFSI}$ for different molar fractions ($x = 0, 0.1, 0.2,$ and saturated) between $-150 - 150^\circ\text{C}$. Typical glass transitions, crystallizations and meltings are highlighted.

3.4 Microwave Synthesis

In the field of chemical synthesis time and energy are both valuable and microwave (MW) based synthesis is extremely beneficial with respect to both. The MW technique is expected to play a fundamental role in a future environmentally friendly synthesis of nano-structured materials [227, 228]. Technically, MW electromagnetic radiation is in the spectrum of wavelengths from 1 mm to 1 m, corresponding to frequencies between 300 MHz and 300 GHz.

MW synthesis is considered as a “soft-chemistry” technique together with techniques such as sol-gel [229] or emulsion drying [230] as they all use low working temperatures. The attractiveness for electrode syntheses lies in the capacity to heat a material from the inside, by converting an electromagnetic energy into heat [231]. Using the penetration potential of the microwave it is possible to generate heat throughout the whole electrode material volume preventing any temperature gradient. Thus, the eternal dilemma between processing times and quality is solved by MW synthesis, as the overall quality for electrochemical applications is enhanced and the time is reduced from days to minutes.

Technically, there are several MW heating processes, but the principle always lies in the ability of an electric field to polarize the charge of the material, where the dipoles cannot follow the rapid change of the electric field (Fig. 20) [232].

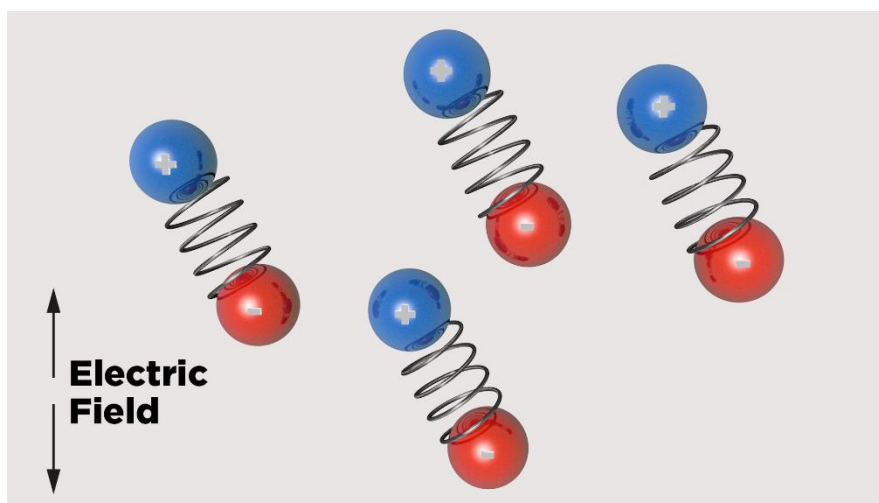


Figure 20. Microwave mechanism from dipole motion.

The restriction of the particle motion by resisting forces, inter-particle interaction, and electric resistance will lead to the generation of random movements producing heat. Therefore, MW radiation has proven to be a highly effective heating source. It can accelerate chemical reaction rates, provide better yields, create more homogeneous materials, stimulate reactions selective to the heating, and achieve better reproducibility [233].

3.4.1 Microwave Electrode Materials Synthesis

Even if the group of Whitacre recently published a paper on MW synthesis of SIB electrode materials [234], most MW synthesis work has focused on LIB electrodes, as presented in the excellent review by Balaji et al. [235]. However, the active use of MW synthesis might be the future also for SIB electrode materials in the near future, and further on likely also within the LIB and SIB industry. While several different approaches of MW synthesis of electrode materials exist, the first to be reported was calcination for the synthesis of LiCoO_2 in 1997 [236]. The experiment procedure was to mix the precursors, $\text{LiCH}_3\text{COO} \cdot 2\text{H}_2\text{O}$ and $\text{Co}(\text{CH}_3\text{COO})_2 \cdot 4\text{H}_2\text{O}$, as pellets to be calcinated in a MW oven. The result obtained was significant, as the loss of lithium during the MW synthesis was only *ca.* 4%, while a loss of 20–30% is normal in conventional synthesis [29]. However, the outstanding feature was the obtained electrode material's ability to withstand high current densities (*ca.* $0.8 \text{ mA} \cdot \text{cm}^{-2}$) without losing more than 5% of the initial capacity. This was ascribed to the formation of reduced size crystallites, improving considerably the electric conductivity of the composite electrode [237].

MW synthesis is possible only if the material can absorb the electromagnetic energy, and if the material absorbs MWs only sparsely, a preheating of the materials or the utilization of a MW amplifier vessel can be used. The MW synthesis in I was carried out in a liquid. At the time, it was one of the first reports dealing with a liquid state MW based synthesis of an electrochemical active electrode material; TiO_2 . The precursors, tetra-butyl ortho-titanate (TBOT) and benzyl alcohol, were initially mixed in a MW active solvent and the final product was obtained in only 20 minutes using a MW effect of 200 W and an amplifier vessel at 200°C . Furthermore, the electrochemical properties of the obtained electrode material such as the cyclability and the capacity retention at high current density were promising.

3.5 Cyclic voltammetry (CV)

Cyclic voltammetry (CV) is a dynamic electrochemical method for acquiring qualitative and quantitative information about the redox processes occurring within an electrochemical cell by scanning the potential at a given sweep rate (usually measured in mV/s) and recording the resulting current. The cell consists of 3 electrodes: a working electrode (WE), a reference electrode (RE) ($\text{Na}^+/\text{Na}^\circ$ in our case), and a counter electrode (CE) (stainless steel (SS) in our case) (Fig. 21). All the electrodes are in contact with the electrolyte.

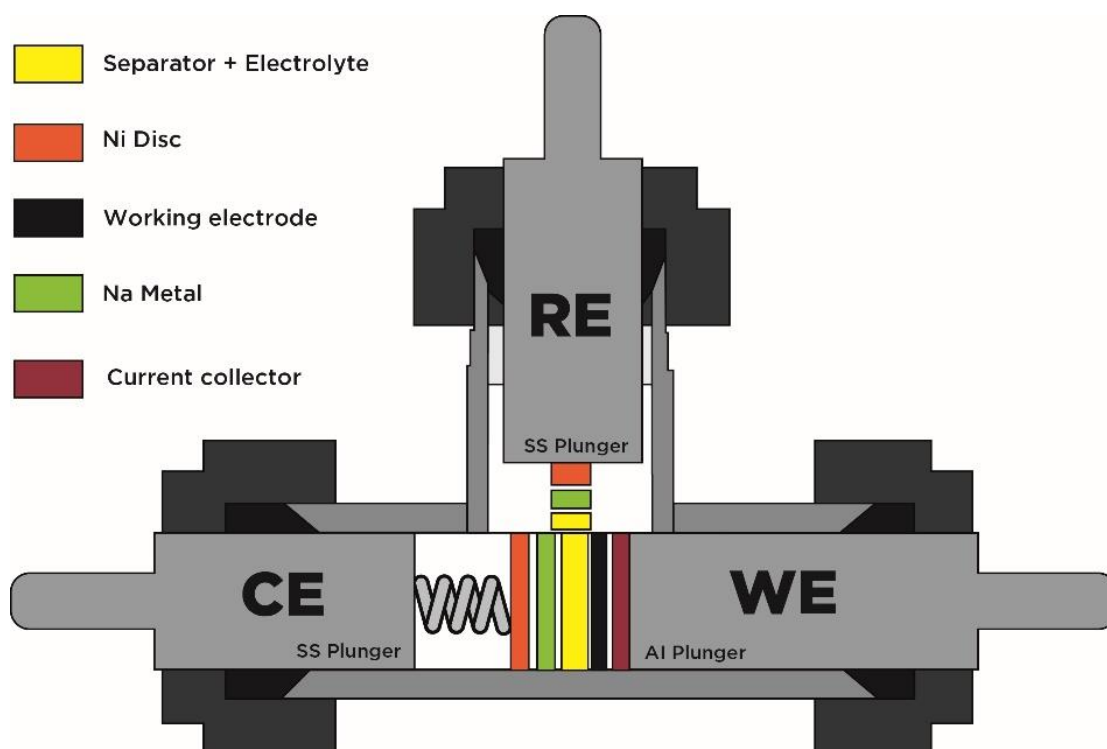


Figure 21. Three electrodes Swagelok cell setup.

The current is measured between the WE and the CE, while no current passes through the RE which serves to monitor the potential of the WE. During the experiment, a linear potential ramp is applied to the WE. The potential sweep starts from the initial open circuit potential V_0 to an imposed potential E_1 . Subsequently the scanning direction is reversed to reach another potential E_2 . Often several cycles are performed during a single experiment in order to observe the stability/evolution of the system. E_1 and E_2 are chosen to match the ESW and observe the electrolyte behaviour at the stability limits. In general, a reduction process takes place at E_1 ascribed to a current decrease while an oxidation process at E_2 ascribed to a current increase (Fig. 22). If an increase or decrease of current is not observed, the electrolyte is stable between the potential limits.

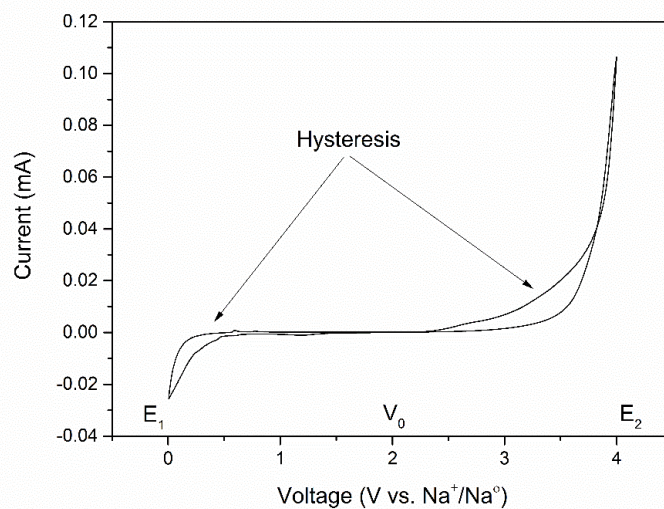


Figure 22. CV of $EC_{0.40}:PC_{0.40}:EMImTFSI_{0.20}$ ($E_1=0.005$) – ($E_2=4$) V vs. Na^+/Na° at a sweep rate of 1 mV/s using an Al WE; $V_0=2$ V vs. Na^+/Na°

3.5.1 Theoretical Foundation

For a better understanding of CV Nernst equation [26] is introduced. It mathematically describes a model with the electrode potential (E_1 , E_2) and the oxidant/reductant species concentration (Eq. 27), directly derived from the Gibbs free energy (Eq. 1). As the connection between the two equations is not trivial, a detailed explanation is written below.

Under standard conditions, the Gibbs free energy is written:

$$\Delta G^0 = -nFE^0 \quad (33)$$

A reaction would thus be spontaneous if E^0 is positive and non-spontaneous if E^0 is negative. From a thermodynamic point of view, ΔG can be expressed as:

$$\Delta G = \Delta G^0 + RT \ln Q \quad (34)$$

with Q being the concentration quotient of the sample species. Furthermore, combining (1) and (33), (34) can be turned into:

$$-nFE = -nFE^0 + RT \ln Q \quad (35)$$

Equation (35) can also be rewritten into the usual Nernst equation representation:

$$E = E^0 - \frac{RT}{nF} \ln Q = E^0 - \frac{RT}{nF} \ln \left(\frac{C_R}{C_O} \right) \quad (36)$$

with C_O and C_R being the concentrations of the oxidized and reduced species, respectively, T the temperature, n the number of electrons, F Faraday's constant, R the gas constant, and E^0 the standard potential.

As can be seen, Nernst equation provides a relation between a potential and a concentration. Therefore, in order to relate a potential to a current – which is the usual CV representation – a relation between the current and the concentration C_O and C_R is given by:

$$i = \frac{dQ}{dt} = -nF \frac{dN}{dt} = nFAD \left(\frac{\partial C}{\partial x} \right)_{x=0} \quad (37)$$

where D is the diffusion coefficient for the species being transported to the electrode surface, $\left(\frac{\partial C}{\partial x} \right)_{x=0}$ is the partial derivative of the concentration of the species with respect to the distance, n the number of transferred electrons, F Faraday's constant, N the number of moles of reductant or oxidant species, and Q the current flux.

3.5.2 CV Data Interpretation

In a cyclic voltammogram the current is typically plotted against the WE potential and each peak observed is associated to a redox process, where the sign of the current determines if it corresponds to an oxidation (positive) or a reduction (negative) process. The peak intensities differ depending of the number of electrons involved, which is related to the concentration of electrochemically active species at the surface of the electrode (Eq. 37). If the redox couple is fully reversible, two peaks will be observed symmetrically, starting at the same onset potential upon oxidation and reduction with equal surface areas i.e. the same number of electrons is exchanged. This is, however, rarely encountered since either kinetic or thermodynamic factors can induce an over-potential and hence a certain hysteresis will be observed. Moreover, some processes may be fully irreversible, such as the SEI-formation in the case of SIBs, and hence only one peak will be observed. Such reactions can also modify the nature of the WE surface and hence differences will be observed between the first and further CV cycles. A cyclic voltammogram of an IL, with the purpose of determining its ESW, the domain within which the IL is neither oxidized nor reduced, is presented in Fig. 23.

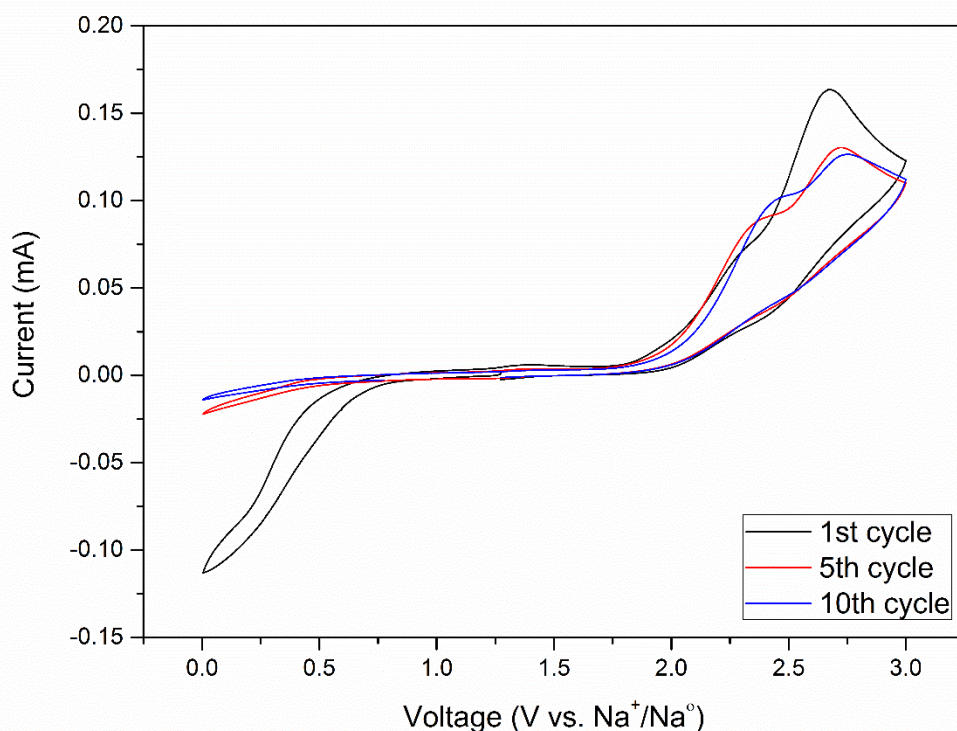


Figure 23. CV of 10 cycles (20 sweeps) for EMImTFSI (0-3 V vs. Na⁺/Na⁰) at a sweep rate of 1 mV/s using a SS WE.

3.6 Chronopotentiometry

Chronopotentiometry is an electrochemical method consisting of applying a constant current (i) to the WE and recording its potential as a function of time. This technique is useful to characterize the electrochemical properties of insertion materials for battery application [32, 51, 56, 95]. Within the battery research field, the method entails the successive application of positive and negative currents within threshold potential values; galvanostatic cycling with potential limitation (GCPL). By GCPL the specific cell capacity (often in mAhg^{-1} of active material) and stability upon cycling can be assessed (Fig. 24). The presence of steps or plateaus in the voltage profile indicate two-phase (heterogeneous) redox processes, while a gradual decay is related to single phase (homogeneous) mechanisms.

Typically the GCPL experiments are performed at different currents (corresponding to different C-rates) to collect information about the kinetics of the redox process(es) (Fig. 25). Indeed, slower kinetics results in a larger decrease of capacity with increasing applied current. In addition, differences in the coulombic efficiency (*c.f.* II, V), by the ratio between the capacities observed for the oxidation and reduction, can give additional information about the presence of any irreversible additional redox process(es) such as electrolyte decomposition or SEI formation.

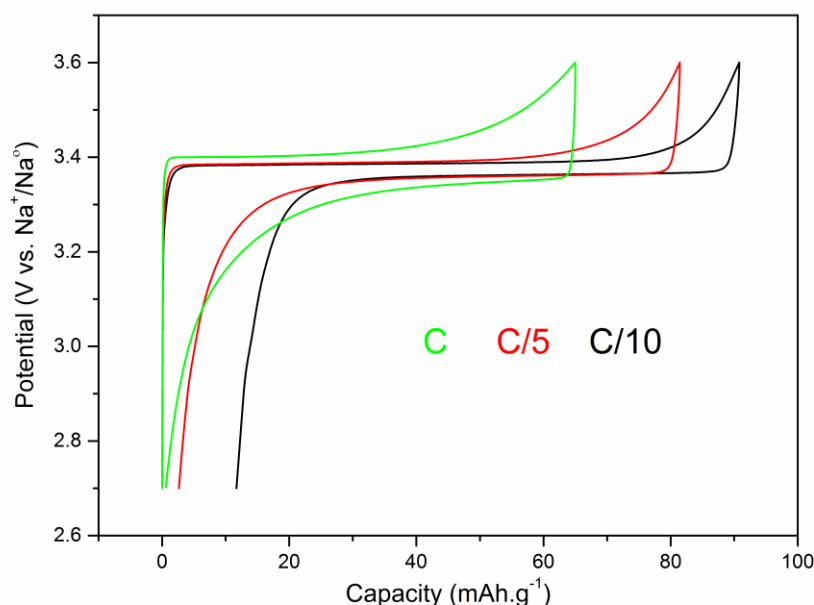


Figure 24. GCPL data for a half cell of NVP of 0.8m NaTFSI in $\text{EC}_{0.45}:\text{PC}_{0.45}:\text{Pyr}_{13}\text{TFSI}_{0.10}$ electrolyte cycled at different C-rates.

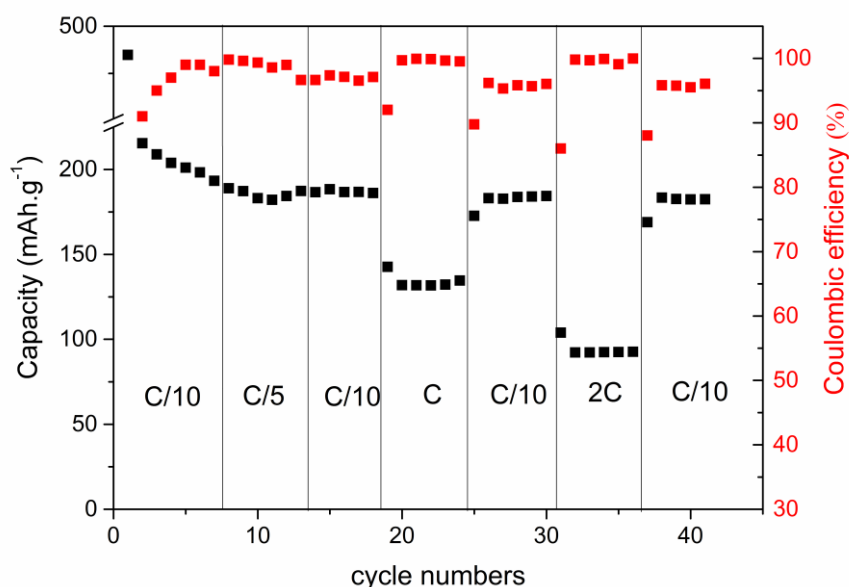


Figure 25. GCPL data for the charge and discharge of NVP with 0.8 m NaTFSI in $EC_{0.45}:PC_{0.45}:PyF_{13}TFSI_{0.10}$ as electrolyte at different C-rates. The alternation between fast and slow C-rates is used to test the structural and chemical stability/reversibility.

3.7 Safety Assessments

Electrolyte ignition is usually the starting point of a chain reaction consuming or destroying an entire battery pack. Therefore, avoiding or lowering the ignition potential of materials such as the organic solvents within the electrolytes is utterly recommended to build safer battery technologies. The safety assessments in this section are related only to the electrolyte itself and through a combination of three independent measures; FP, SET, and IT.

3.7.1 Flash Point (FP)

The flash point (FP) is the lowest temperature at which the application of an ignition source causes the vapours of a material to ignite. Often standardised conditions are applied to measure it: pressure (often 101.3 kPa), distance sample-ignition source, time, etc. The FP should not be confused with the fire point or the auto-ignition point; the former is the temperature at which the vapours continue to burn after being ignited, while the latter is the temperature at which a sample ignites without the help of an external ignition source.

If a solvent has a FP over 100°C it is for our purposes considered as non-flammable. The electrolytes in **V** tend to have high FPs due to the addition of ILs, a characteristic beneficial for battery application as it minimizes the issues described in section 2.5.

There are at least two different methods to obtain the FP. The more manual method consists in increasing the temperature and visually detecting the ignition of the sample

using a glowing wire, a flame, or an electric arc. This approach is usually not very accurate and poorly reproducible. In our, more automated case, a specific FP tester has been used where the sample is placed in a heatable cup placed in a closed chamber. The temperature of the sample is then slowly increased while an electric arc is activated periodically above the cup surface. Upon ignition the pressure in the chamber increases and this determines the FP. In general, the so-obtained flame covers at least 75% of the surface at this temperature in order for the FP to be assigned.

3.7.2 Ignition Time (IT)

Upon contact with an ignition source the sample might not be ignited immediately - several seconds may be necessary before the flame appears. The IT is relatively easy to collect by the experimenter; for LP30 and EC:DMC based electrolytes, the sample ignition was relatively quick (*ca.* 2-3 seconds) as a continuous flame was obtained nearly immediately after the utilisation of the flaming butane torch. The result corroborates to the ITs obtained by Wilken *et al.* [238]. However, the use of EC:PC and furthermore ILs, greatly modified (*i.e.* 10-18 seconds) the IT and several seconds were necessary to permanently ignite the electrolyte. The IT could here not be associated only to the appearance of a flame as it was not as clear as for the EC:DMC based electrolytes. Therefore, a different protocol was chosen and the IT was decided to be calibrated as the time necessary to have a sustainable flame. As a verification an exposure time below the calibrated IT did not generate the permanent flame necessary for the SET experiments (3.7.3). In general, an increased IT can be due to the presence of additives *e.g.* ILs that lower the vapour pressure and hence the amount of ignitable vapour, which of course improves the safety.

3.7.3 Self-Extinguishing Time (SET)

The SET is based on the ability of a material to cease burning once the ignition source has been removed; the shorter the SET – the safer the electrolyte. The SET can be significantly reduced if the ignitable radicals in the emanating vapour are consumed or inhibited by use of proper electrolyte additives *e.g.* flame-retardants [239]. In practice, in the case of an abuse situation of a battery, a fire self-extinguished after only a few seconds has less likelihood to propagate to the surrounding materials/cells – making a short SET extremely important. In **V** a defined amount, less than a gram, of electrolyte, was placed on a watch glass and ignited with the help of a flaming butane torch. The amount is important as the mass will affect the SET (thus measured in s.g^{-1}). As soon as the vapour started to burn, the time was recorded until the flame disappeared – thus a manual method with reproducibility errors why all samples were measured at least 6 times. Despite the manual SET determination method, the standard deviation was relatively low.

4 Results and Discussions

A brief summary of the results contained in the appended papers of this thesis is presented in this chapter. This section is, however, not following a chronologically or paper based order; instead a joint scientific reasoning is used intending to help the reader to go further in understanding the findings, by the topics of the sub-paragraphs composing this chapter.

First, the many physical properties of imidazolium and pyrrolidinium type ILs and their electrolytes will be discussed including viscosity, ionic conductivity, thermal stability, density, and safety properties. Concise explanations will be developed including the influence of the salt concentration, the effect of the specific choice of IL, the temperature dependence, and a discussion on safety assessments. These results are compared to organic solvent based electrolytes to examine the viability of ILs as solvents/components of electrolytes for SIB application.

Second, studies of the Na⁺ cation solvation with the help of Raman spectroscopy will be presented. This includes discussions on the molecular arrangements about the Na⁺ and its solvation shell, as supported by DFT calculations for pure ILs, and extending also to the complexation in hybrid electrolytes of both organic solvents and ILs.

At last, a short discussion is made on the synthesis of the SIB anode material TiO₂ using MWs, and the advantages this technique can provide for any type of battery electrode materials and technology. The electrochemical properties of full and half-cells of SIBs such as the ESW exemplified by the cycling properties of HC and NVPF electrodes, potentially to be used in the next generation of SIBs, will also be discussed.

4.1 Physical Properties of IL Based SIB Electrolytes

ILs based electrolytes have received a lot of attention in recent years as described in **IV**. However, most of the early focus was placed on the physical properties such as ionic conductivity, thermal stability, density, viscosity – including ours (**II**, **V**). With the help of these characterization studies the aim was to make it possible to identify IL based electrolytes as performant as typical organic solvent based electrolytes.

Starting with the Na-salt concentration effects in the ILs EMImTFSI and BMImTFSI, the total conductivity is in general only slightly affected with the addition of Na-salt. As the ILs are exclusively composed of ions, the ionic conductivity reported in all our papers is not representing the migration of Li⁺/Na⁺ charge carriers, but overwhelmed by all the IL ions present (section 2.3.2). As an example from **III**, a slight difference of 1.7 mS.cm⁻¹ at RT between the pure BMImTFSI IL and the saturated Na_xBMIm_{1-x}TFSI electrolyte was recorded, as well as an almost linear conductivity decreasing trend (Fig. 26) – a trend observable also

in the literature [174, 176, 240-243]. In contrast, this behavior is not found for organic solvent based electrolytes (*e.g.* EC, PC, DMC, *etc.*), which usually present local conductivity maxima at *ca.* 0.5-0.8 M and 1 M, for appropriate Na and Li-salts dissolved, respectively [244, 245]. Then, focusing again on the IL properties, the influence of the IL cation alkyl chain length seems to be moderate as moving from BMIm to EMIm based electrolytes has only a very slight effect on the total ionic conductivity. That said, all ion conductivities recorded at RT for IL based electrolytes were above 1 mS.cm⁻¹, which is the usually quoted target battery applications such as LIBs and SIBs. The results presented are similar to those found for LIBs [154, 240, 241, 246], with the exception of the Na⁺ conducting electrolytes displaying slightly better conductivities, despite the Li_xEMIm_(1-x)TFSI system being less viscous than the corresponding Na_xEMIm_(1-x)TFSI system (III). The latter is most probably due to the large IL cation/anion contribution, together with the beneficial properties of Na⁺ containing complexes being [Na(TFSI)_n]⁻⁽ⁿ⁻¹⁾ as compared to [Li(TFSI)_n]⁻⁽ⁿ⁻¹⁾.

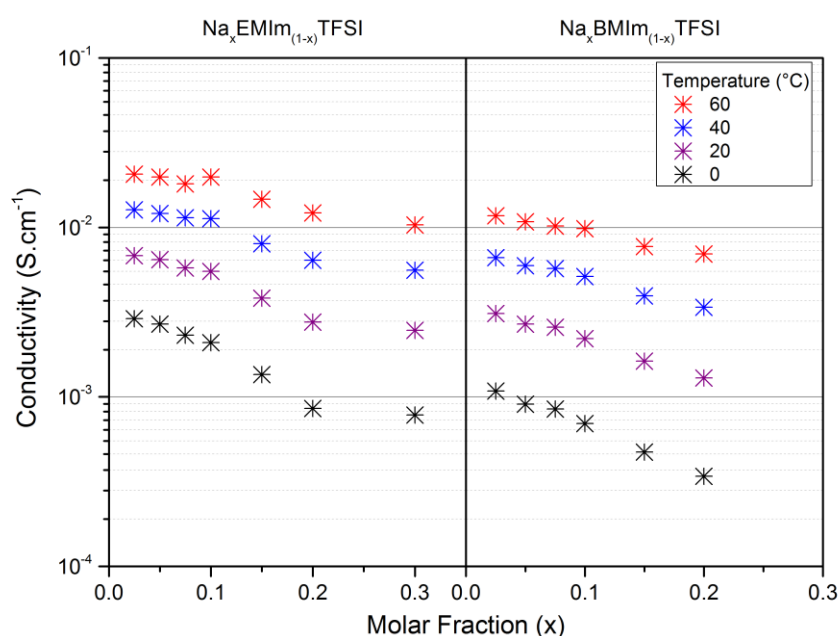


Figure 26. Isotherms of the conductivity for (a) Na_xEMIm_(1-x)TFSI and (b) Na_xBMIm_(1-x)TFSI for different molar fractions ($x = 0.025, 0.05, 0.075, 0.1, 0.15, 0.2,$ and saturated). (III)

Modifications of the conductivity are also noticeable when the IL percentage is modified as in the organic solvent /IL hybrid electrolytes. In V, the conductivities of hybrid electrolytes based on EC, PC, Pyr₁₃TFSI and BMImTFSI, all with 0.8 m NaTFSI were studied. Adding 10-20% of IL slightly increases the (total) ionic conductivity in parallel with increasing the viscosity (Figs. 26 and 27).

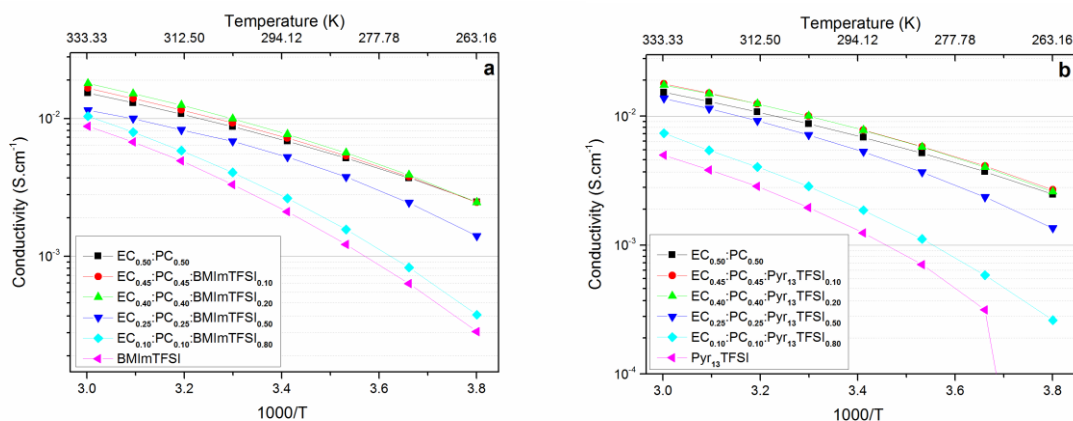


Figure 27. Conductivities of (a) $EC_x:PC_x:BMImTFSI_{(1-2x)}$ and (b) $EC_x:PC_x:Pyr_{13}TFSI_{(1-2x)}$ as functions of temperature. (V)

This observation is re-joining the statement emphasizing the IL ions' contribution to the total conductivity of IL based electrolytes. As the IL contents reaches 50% the conductivities fall drastically, most probably due to the large increases in viscosities. ILs have relatively high viscosities in comparison to organic solvents (II, III, V), problematic for electrochemical application as this usually leads to slower charge displacement and higher heat generation due to resistive heating. The temperature dependence of the ionic conductivity between the organic based EC_{0.50}:PC_{0.50} and the IL based EC_{0.40}:PC_{0.40}:CatTFSI_{0.20} or EC_{0.45}:PC_{0.45}:CatTFSI_{0.10} electrolytes show a general trend that is similar at low temperatures where the conductivities are quasi equal, while there are noticeable differences at higher temperatures. This is a result strongly influenced by the viscosity – as the viscosities differ less at the higher temperatures (Fig. 28).

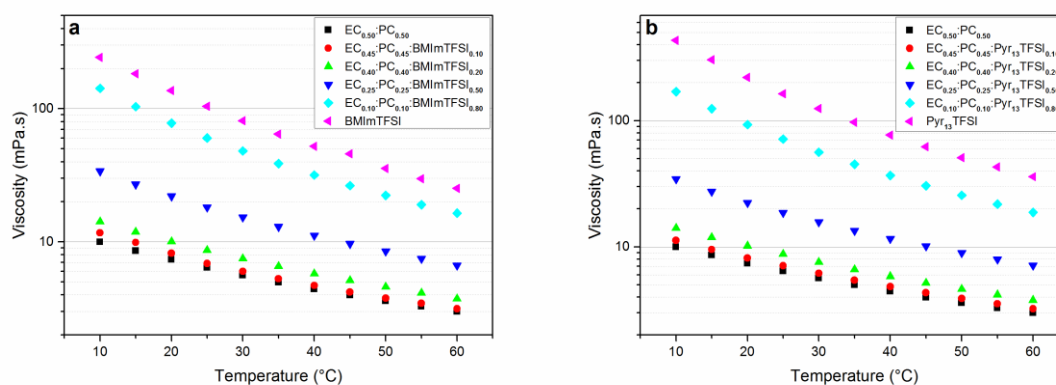


Figure 28. Viscosity of (a) $EC_x:PC_x:BMImTFSI_{(1-2x)}$ and (b) $EC_x:PC_x:Pyr_{13}TFSI_{(1-2x)}$ as functions of temperature. (V)

Thermal properties of electrolytes are important as a stable electrolyte over a large range of temperature is very useful. The thermal range stretches from the T_g to the decomposition temperature, assuming the electrolyte to remain liquid in this range. In III, the T_g was shown to increase as a function of the salt concentration, from -93.7 to -73.4 °C for BMImTFSI and EMImTFSI based electrolytes. This could tentatively mean two different processes taking place: i) Na⁺ complexes with low mobility are formed and/or ii) Na⁺ induced dynamic cross

linking is introduced. Furthermore, the BMImTFSI based electrolytes do not present any crystalline phases, while the EMImTFSI systems do (Fig. 29) – and thus a reduced temperature stability range. It is therefore probable that different Na⁺ complexes are formed (I, II, III, V), and this is the topic of the following section.

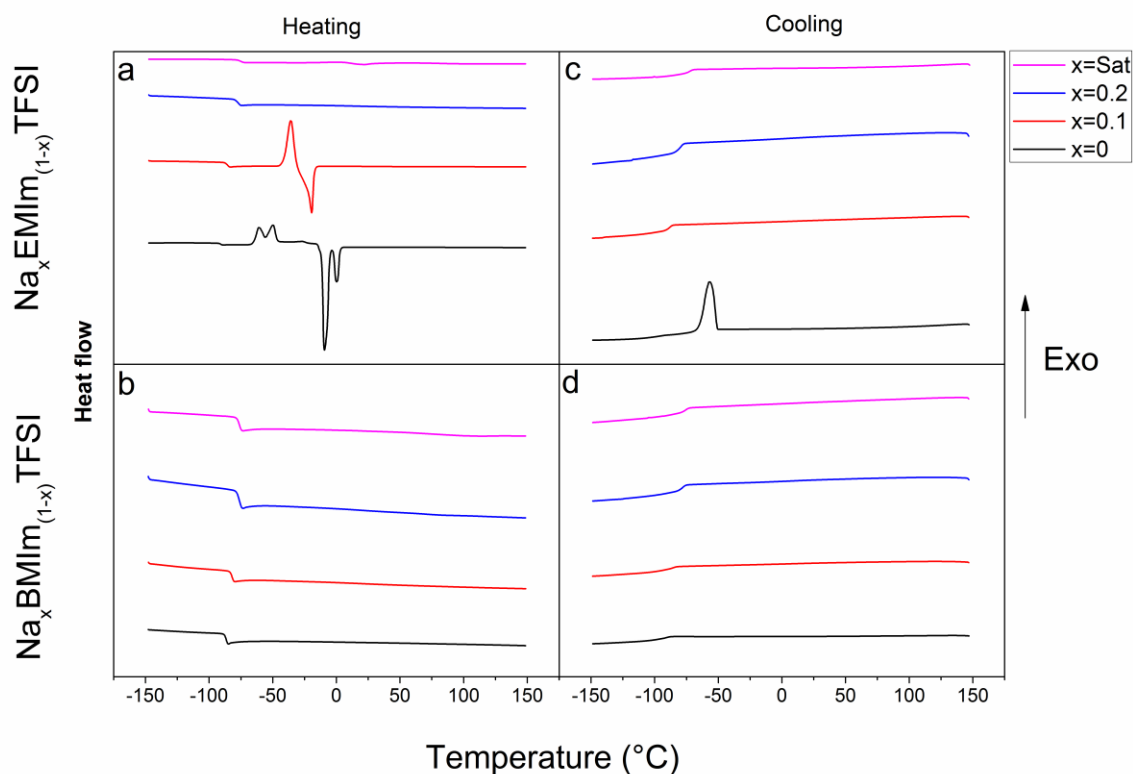


Figure 29. Isotherms of the conductivity for (a) $\text{Na}_x\text{EMIm}_{(1-x)}\text{TFSI}$ and (b) $\text{Na}_x\text{BMIm}_{(1-x)}\text{TFSI}$ for different molar fractions ($x = 0.025, 0.05, 0.075, 0.1, 0.15, 0.2,$ and saturated). (III)

Safety is a requirement for any SIB electrolyte, and to use ILs as additives to improve the flammability properties without severely decreasing the general performance is one approach taken (V). Properties such as the FP, IT, and SET for both Li⁺ and Na⁺ conducting hybrid electrolytes were measured, and for example the FPs of electrolytes with IL contents of 2% to 80% increase from 140°C to 180°C (Fig. 30). Moving to the ITs of EC:PC and EC:PC:IL these are 10 s and 18 s, respectively, and a regular electrolyte(LP30) has >16 s shorter IT than the hybrid electrolytes (Fig 30b). At last, the SET data are in the line with the other safety improvements; any type of IL added decrease the SET linearly over the full range, but most notably the initial addition of 2% of IL reduced the SET by half.

At last, the origins of the safety enhancements have been investigated using the Raman bands from the organic solvents such as EC and PC, before and after safety tests. These bands decrease in intensity, thus a sign of these solvents to be preferentially consumed, while the IL band shapes remain identical with only a minor increase in relative intensity.

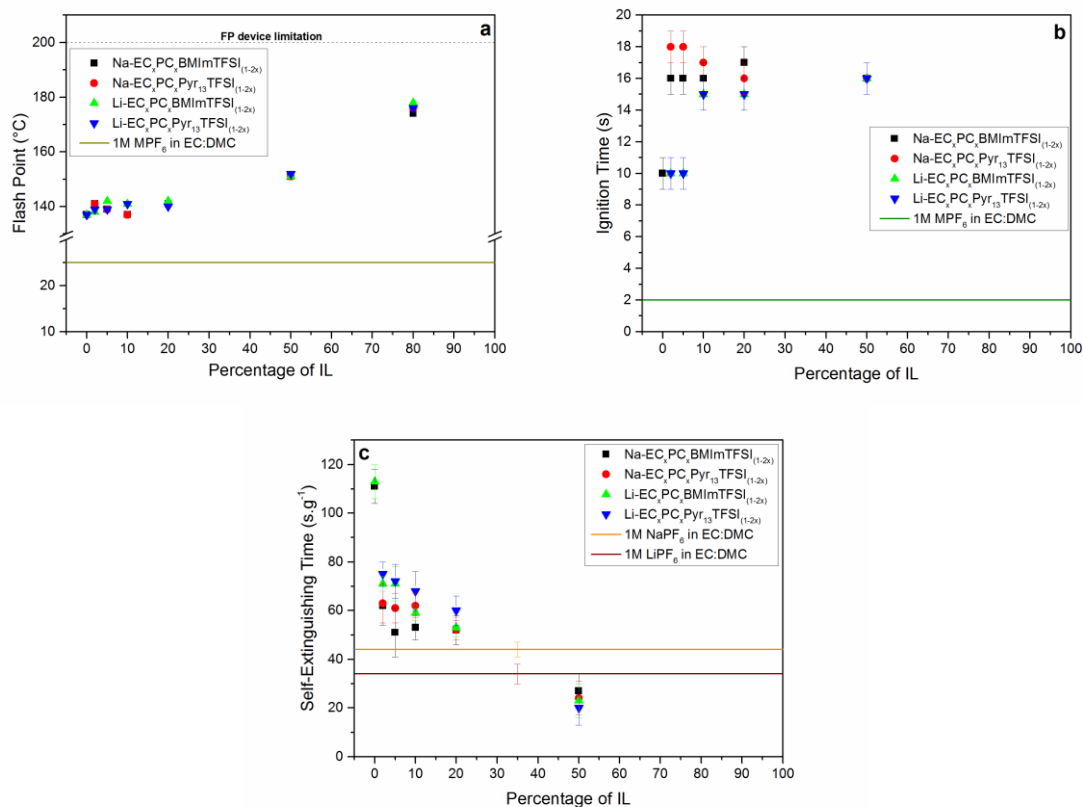


Figure 30. Various safety measures as functions of the electrolyte IL content: (a) FP, (b) IT, and (c) SET. Reference data for 1M MPF_6 in EC:DMC ($M=\text{Na}, \text{Li}$) are represented by horizontal lines. (V)

4.2 Sodium Ion Solvation and Coordination

The Na^+ or Li^+ solvation in battery electrolytes is a basic requirement to allow for charge carrier of interest to be transported through the electrolyte and between the electrodes. Depending on the composition of the electrolyte, different complexes can be formed, ultimately influencing properties such as the ionic conductivity and the viscosity. In this thesis Raman spectroscopy and DFT calculations have been used, often jointly, in order to characterize these complexes – in liquid i.e. organic solvent based (II), IL based (III), and hybrid organic solvent / IL based (V) electrolytes.

As a few examples, in III, the formation of $\text{Na}[(\text{TFSI})_n]^{-(n-1)}$ was investigated for imidazolium cation IL based electrolytes and compared to the already studied $\text{Li}[(\text{TFSI})_n]^{-(n-1)}$ complexes arising from the analogous Li system [247-250]. The strong Raman band located at $730\text{-}765\text{ cm}^{-1}$, known as the best solvation probe for TFSI [247, 249, 251-254], was examined in detail and deconvoluted into two different bands (e.g. “free” TFSI and coordinated TFSI) (Fig. 31, insert). Going from the pure ILs to the highly salt concentrated IL based electrolytes induces a shift from 742 cm^{-1} to 744 cm^{-1} of the convoluted band, due to the formation of ion-pairs, $\text{Na}^+\text{-TFSI}$, and higher aggregates $\text{Na}[(\text{TFSI})_n]^{-(n-1)}$.

Moreover, the cation impacts strongly on the location of the M^+ -TFSI band ($M = \text{Li}, \text{Na}$), where the Li^+ -TFSI and Na^+ -TFSI bands are located at 748 cm^{-1} and 746 cm^{-1} , respectively. This is due to the different charge/radius ratios, with the Na^+ -TFSI interaction being slightly weaker. Therefore, depending on the impact of the respective bands, the average convolution can be located from 742 to 744 cm^{-1} as stated above. For the $\text{Na}[(\text{TFSI})_n]^{-(n-1)}$ complexes the method developed by Lassègues [250] for LIBs and particularly for $\text{Li}[(\text{TFSI})_n]^{-(1-n)}$ was used and adapted (III); the analysis of the intensity (area) ratio $I_{746}/(I_{746}+I_{742})$ for the two TFSI bands revealed that the most representative complex for Na^+ seems to be $\text{Na}[(\text{TFSI})_3]^{2-}$ over the entire concentration range, while for the analogous Li^+ system it was $\text{Li}[(\text{TFSI})_2]^-$ [250]. Comparing conductivities and viscosities for Na and Li conducting IL based electrolytes (III), the Na based electrolytes were found to have lower conductivities and higher viscosities, in accordance with a larger Na complex formed. This was also supported by DFT calculations showing $\text{Na}[(\text{TFSI})_3]^{2-}$ (and $\text{Na}[(\text{TFSI})_2]^-$) to be energetically favoured (III).

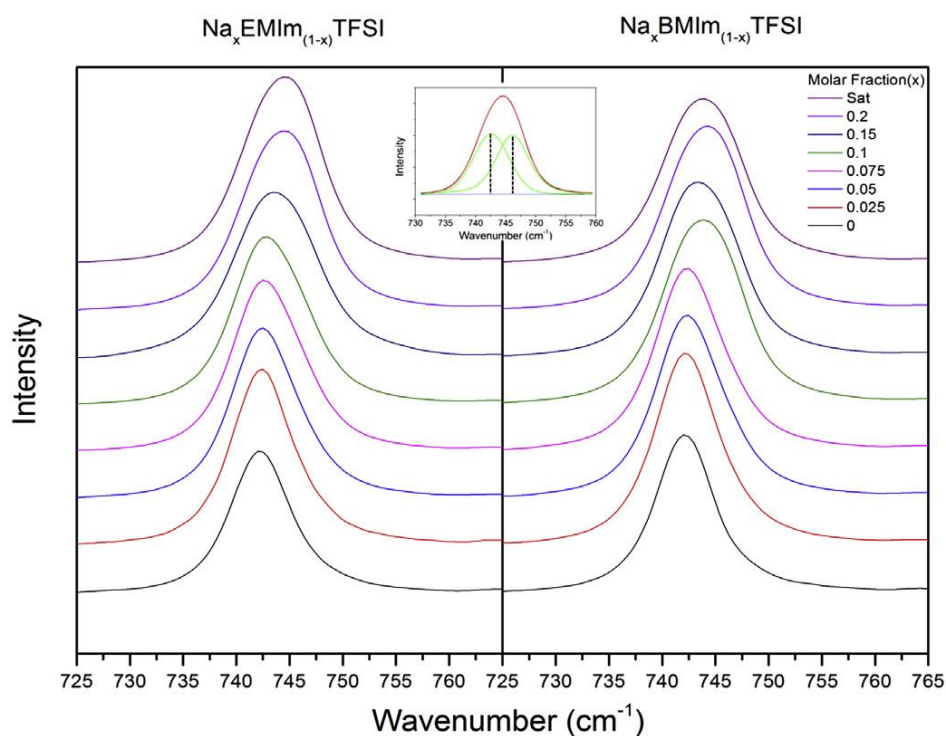


Figure 31. Raman spectra of $\text{Na}_x\text{EMIm}_{(1-x)}\text{TFSI}$ and $\text{Na}_x\text{BMIm}_{(1-x)}\text{TFSI}$ between $725\text{-}765 \text{ cm}^{-1}$ for different molar fractions with the deconvolution and fitting for $\text{Na}_x\text{EMIm}_{(1-x)}\text{TFSI}$, $x=\text{sat}$, as insert.

In both II and V studies on liquid and hybrid electrolytes were carried out to determine the composition of the Na^+ solvation shell. In contrast to III the salt concentration was kept constant while the proportions of the solvents in the electrolytes were modified. In II the liquid electrolytes contained NaTFSI, EC, PC, and DMC, while the hybrid electrolytes in V were composed of NaTFSI, EC, PC, and various ILs. Both in II and V the Raman spectroscopy analysis of the EC ring bending mode band at 714 cm^{-1} [255-258] and the EC breathing mode band at 893 cm^{-1} [255, 259], shifting to 724 cm^{-1} and 900 cm^{-1} upon sodium cation coordination (Fig. 32), respectively, revealed that the solvation shells were constituted mainly of EC. Considering the other potential contribution in II, DMC, the band located at

915 cm^{-1} presented a very weak intensity shoulder/band at 925 cm^{-1} assignable to Na^+ -DMC (Fig. 28a), suggesting its contribution to the solvation shell to be minor. The PC band located at 712 cm^{-1} did not show any change suggesting none or only a weak contribution to the Na^+ solvation.

In **II** the TFSI contribution to the solvation shell was minor and constant, proportional to the 1 M salt concentration, while in **V**, the ILs provided a large amount of TFSI enhancing the contribution. Therefore, the solvation shells in **V** were mainly constituted of EC and TFSI for all the hybrid electrolytes (Tables 12 and 13). In more detail the addition of IL increased the SN_{TFSI} contribution, decreased the SN_{EC} , and decreased the SN_{Total} . The latter could be due to steric effects hindering EC and TFSI to coordinate Na^+ simultaneously.

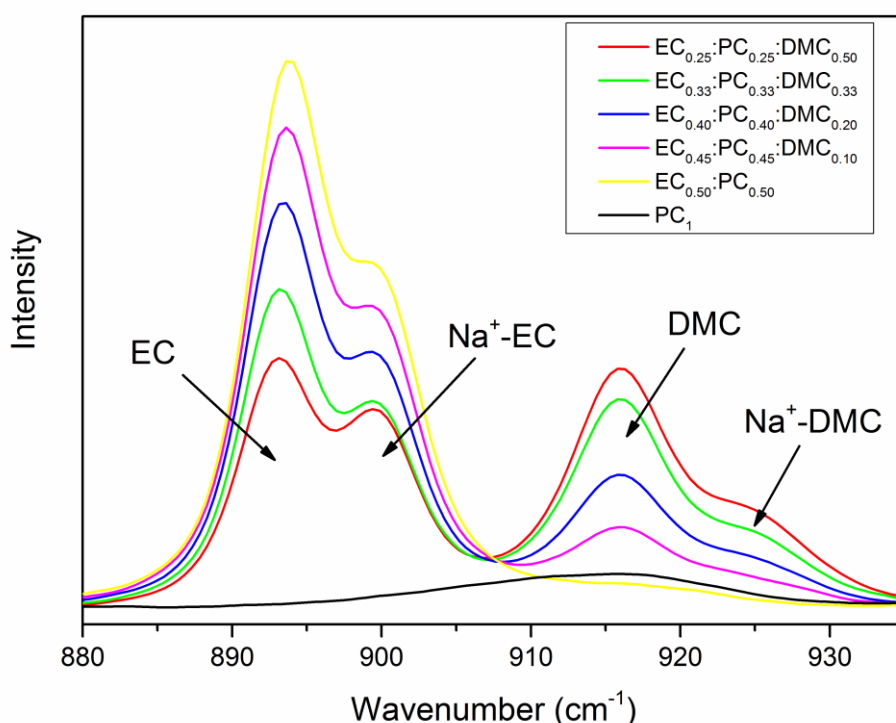


Figure 32. Raman spectra of 1 M NaTFSI in $\text{EC}_x:\text{PC}_x:\text{DMC}_{(1-2x)}$ between 880-940 cm^{-1} for different electrolyte compositions ($x= 0.25, 0.33, 0.45, \text{ and } 0.50$).

Table 12. Associated vibrational modes to bands used in the analysis of hybrid electrolytes.

Vibrational mode	ν_{SNS}		$\nu_{\text{ring breathing}}$	
	TFSI	Na^+ -TFSI	EC	Na^+ -EC
Species	TFSI	Na^+ -TFSI	EC	Na^+ -EC
Experimental Frequency [cm^{-1}]	741±1	744±1	893±1	901±1
Computed Raman Activity [$\text{amu } \text{Å}^{-4}$]	20	19.2	13.7	18.3

Table 13. Solvation number analysis of hybrid electrolytes for two different types of ILs.

Electrolytes	$\frac{A_{Na^+-EC}}{A_{Total}}$	$\frac{A_{Na^+-TFSI}}{A_{Total}}$	SN_{EC}	SN_{TFSI}	SN_{Total}
EC _{0.45} PC _{0.45} BMIImTFSI _{0.10}	0.41	0.27	2.16	0.35	2.52
EC _{0.25} PC _{0.25} BMIImTFSI _{0.50}	0.47	0.31	1.42	0.79	2.21
EC _{0.10} PC _{0.10} BMIImTFSI _{0.80}	0.54	0.31	0.67	1.07	1.73
EC _{0.45} PC _{0.45} Pyr ₁₃ TFSI _{0.10}	0.37	0.30	1.98	0.40	2.38
EC _{0.25} PC _{0.25} Pyr ₁₃ TFSI _{0.50}	0.55	0.27	1.71	0.70	2.41
EC _{0.10} PC _{0.10} Pyr ₁₃ TFSI _{0.80}	0.58	0.34	0.72	1.20	1.92

4.3 Electrode Synthesis and SIB Performance

The electrode synthesis plays a major role in the mechanical and electrochemical performance of any battery type *e.g.* LIB, SIB [260]. In this thesis, the MW synthesis have been chosen due to its attractiveness to produce inorganic nanoparticles and more specifically TiO₂ anode nanoparticles [235, 261]. The MW technique allows a much faster synthesis of the active TiO₂ material with smaller particle sizes and a higher yield. Furthermore, the synthesis was made in a liquid environment and at the time of the publication it was the first known TiO₂ electrode made with this set-up and technique. The final results were impressive as only two minutes were necessary to synthesize particles of sizes ranging between 3-15 nm, while other techniques would need several days to obtain larger sized particles [262, 263]. Aside the amount of time saved, generally commercially attractive, the particle size reduction usually affects the electronic and ionic diffusion of the electrode to improve the electrochemical properties [264]. TiO₂ anatase have been also synthesized using a domestic MW and it has been shown that the particle size were larger than the liquid phase synthesis. In I the electrochemical performance for the MW synthesized TiO₂ active anatase (Fig. 33) showed capacities of 155 mAhg⁻¹ at C/15 with a good capacity retention were observed at high C-rates, 70 mAhg⁻¹.

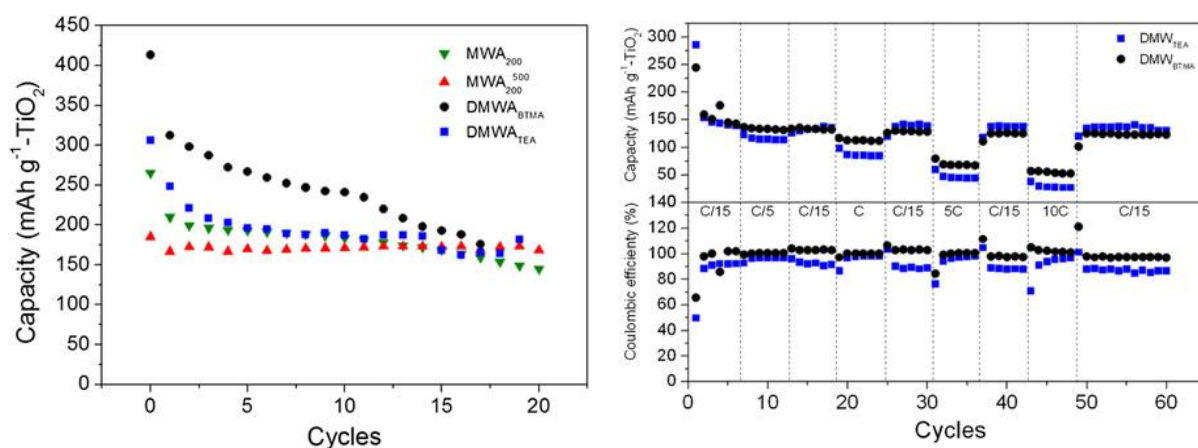


Figure 33. Capacity versus cycle number for MWA_{200} (green inverted triangles), MWA_{200}^{500} (red triangles), DMW_{BTMA} (black circles), DMW_{TEA} (blue squares) (left), and capacity versus cycle number of DMW_{BTMA} (black circles) and DMW_{TEA} (blue squares) (right) all cycled at C/15-rate. (I)

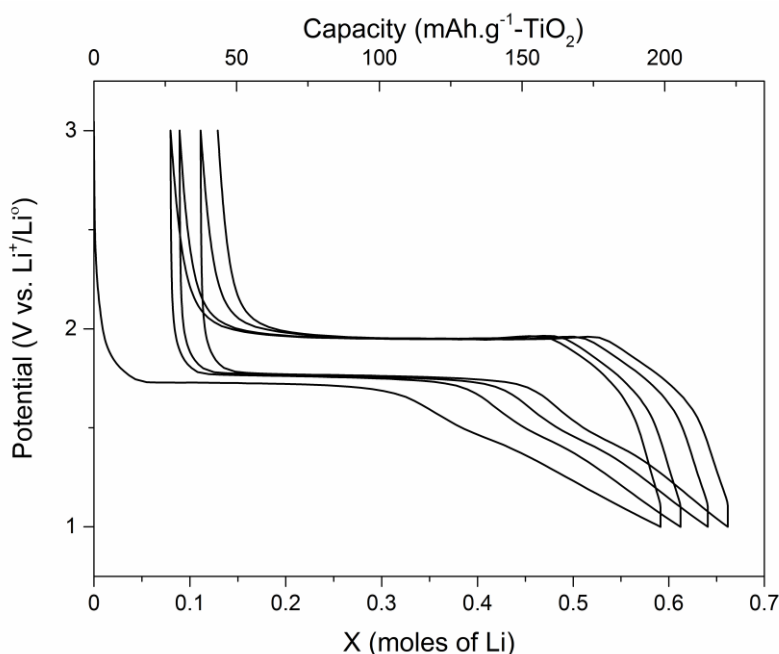


Figure 34. Typical behaviour of the anatase TiO_2 anode material (MW_{200}^{500}) between 1-3 V vs. Li^+/Li^0 .

In II and V the HC anode material was extensively studied. While the study on TiO_2 was more focused on the influence of the synthesis on the electrochemical performance, the studies on HC were oriented towards the influence of the electrolytes compositions on the electrochemical properties such as specific capacity and rate capability (Fig. 35), and safety. In II 1 M $NaClO_4$ in EC:PC:DMC with different solvent proportions were used, as the main purpose was to observe the influence of DMC content. It was revealed that while DMC does not take a major part in the Na^+ solvation, only 10% of DMC was enough to decrease the overpotential between charge and discharge cycles together with an improvement of the rate capability, remaining at above 300 mAhg^{-1} . Adding more DMC decreased the coulombic efficiency, probably due to the poor electrochemical stability of DMC at low potentials. Moreover, the SEI study using XPS revealed EC to be the main contributor to the SEI.

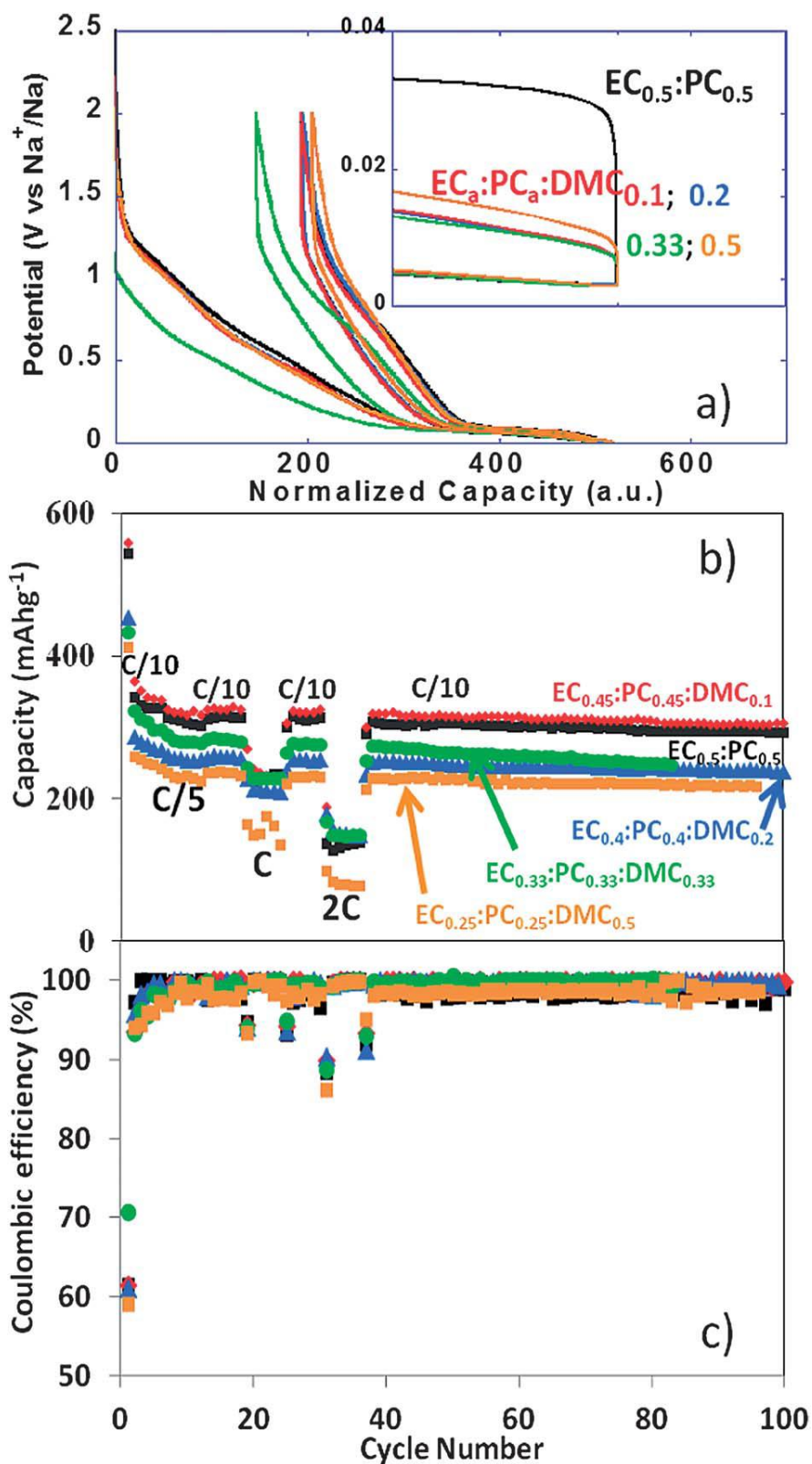


Figure 35. (a) 1st cycle voltage vs. normalized capacity profiles for HC using 1 M NaClO₄ in EC:PC:DMC electrolytes with various amounts of DMC recorded at C/20-rate, (b) discharge capacity and (c) coulombic efficiency vs. cycle number for the corresponding half-cells.

The strategy in **V** was slightly different as the major aim was to improve the safety properties of the SIBs without too much negative impact on the electrochemical properties such as specific capacities and capacity retention. Therefore, DMC was replaced by ILs, BMImTFSI, EMImTFSI, or Pyr₁₃TFSI, which are known for their beneficial properties for safety (section 2.3.2) and cycled in cells with electrolytes of the composition 0.8 m NaTFSI in EC:PC:IL. The CV experiments revealed that adding more than 10% of IL impacts negatively on the ESW at low potentials, likely due to IL decomposition. However, the addition of ILs in the electrolyte composition can also be beneficial as the corrosion potential of Al was shifted to a higher voltage; from 3.5 to 4.5 V vs. Na⁺/Na⁰ [265, 266]. From all the compositions tested, the EC_{0.45}:PC_{0.45}:Pyr₁₃TFSI_{0.10} hybrid electrolyte was selected for further cycling studies with HC. Here the 1st cycle exhibited a large irreversible capacity leading to a coulombic efficiency of mere 40%, while for the subsequent 7 cycles the capacity was found to only slightly decrease with concomitant increase in the coulombic efficiency, indicative of continuous SEI formation (Fig 36).

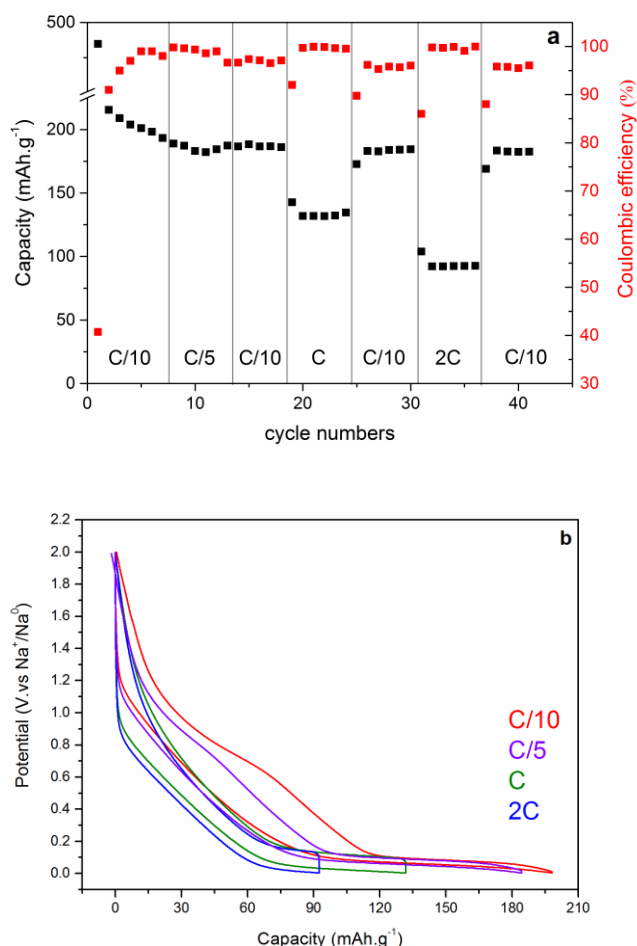


Figure 36. (a) Coulombic efficiency and discharge capacity vs. cycle number for HC electrodes tested at C/10, C/5, 1C, and 2C-rates and a EC_{0.45}:PC_{0.45}:Pyr₁₃TFSI_{0.10} electrolyte and (b) Potential vs. capacity profiles at different C-rates for HC and a EC_{0.45}:PC_{0.45}:Pyr₁₃TFSI_{0.10} electrolyte.

A good capacity retention was obtained for HC in $\text{EC}_{0.45}:\text{PC}_{0.45}:\text{Pyr}_{13}\text{TFSI}_{0.10}$ with a specific capacity of 185 mAhg^{-1} at C/10 over 50 cycles. Several factors could explain the differences of specific capacities obtained in II and V. The IL may modify the SEI composition as compared to EC:PC:DMC, possibly detrimental to the system stability and increasing the electrolyte decomposition processes at low potentials and negatively impact the diffusion of Na^+ due to a different composition. Yet another reason could be that the HCs were not identically treated.

Moving to the positive electrode tests, carbon-coated NVPF was studied using 1 M NaPF_6 and 1 M NaClO_4 in $\text{EC}_{0.45}:\text{PC}_{0.45}:\text{DMC}_{0.10}$ as the electrolytes. An excellent capacity retention was achieved with stable specific capacity of 110 mAhg^{-1} at C/20 for 80 cycles. In addition an impressive rate capability was achieved with more than 90 mAhg^{-1} at 20C (II). Therefore, by assembling a full cell of HC, NVPF, and 1 M NaX ($X = \text{PF}_6, \text{ClO}_4$) in $\text{EC}_{0.45}:\text{PC}_{0.45}:\text{DMC}_{0.10}$, it was possible to make a fully operative SIB with a very low polarisation and excellent capacity retention upon cycling with 97 mAhg^{-1} over 120 cycles (Fig. 37).

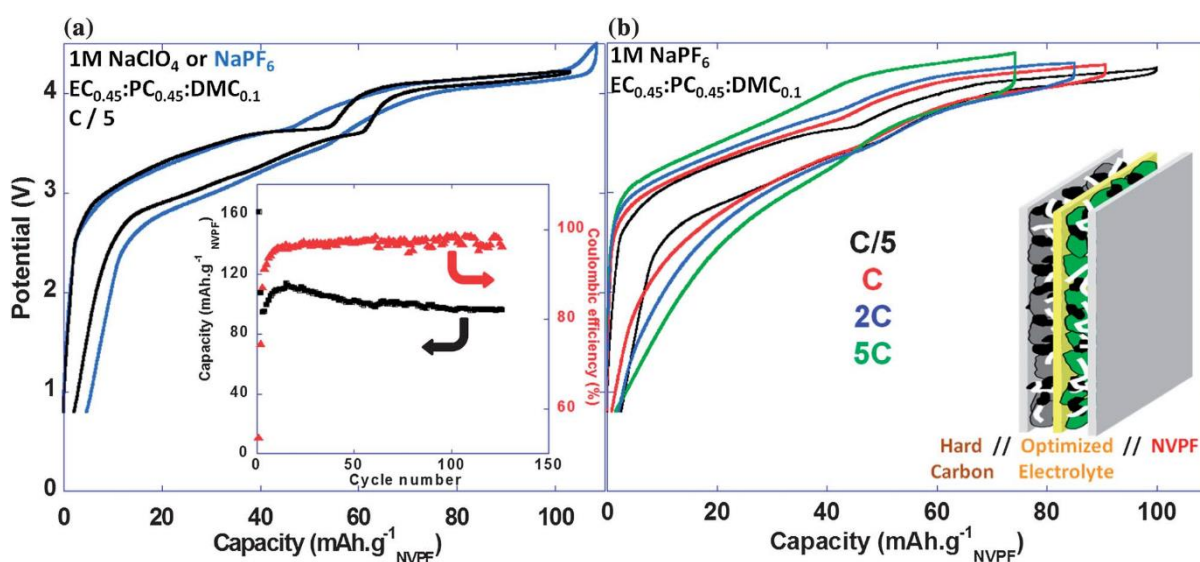


Figure 37. (a) Voltage vs. capacity profiles for HC || NVPF full SIB cells cycled with 1 M NaPF_6 or 1 M NaClO_4 in $\text{EC}_{0.45}:\text{PC}_{0.45}:\text{DMC}_{0.1}$ electrolytes recorded at C/5-rate (b) Voltage vs. capacity profiles for HC || NVPF full SIB cells cycled with 1 M NaPF_6 in $\text{EC}_{0.45}:\text{PC}_{0.45}:\text{DMC}_{0.10}$ electrolytes at different C-rates.

5 Conclusions and Outlook

- It is possible to run full SIB cells exhibiting excellent properties using electrode materials of today, despite these still being under optimisation.
- From simulations of cells SIBs and LIBs can have similar energy densities. It would not be surprising to see the amount of SIB investigations to increase further in the near future.
- Lithium and sodium conducting electrolytes and storing electrodes behave differently, which holds promise as electrode materials electrochemically inactive for lithium can be active for sodium.
- Ionic liquid based, or hybrid, electrolytes are viable for battery applications and may bring a higher degree of safety, a far from negligible factor for commercialisation.
- The mode of electrode material synthesis can change the reactivity of a material and MW based synthesis is a promising route to improved SIB performance. The short processing time can be of interest and importance for mass production.

The outlook is primarily based on the results of the papers presented:

- **Paper I:** It would be interesting to apply the MW synthesis route for other SIB electrode materials, both anodes and cathodes, as it has been proven so efficient for the anatase TiO₂ anode materials.
- **Paper II:** The results obtained with liquid organic solvent based electrolytes is a good omen also for a possible application with ILs as safety enhancing additives, even if the ionic conductivities would be slightly reduced.
- **Paper III:** The spectroscopic characterization of IL based electrolytes will be a future tool for increased understanding also of the formation of the SEI within SIBs. Indeed, it would be interesting in the future to focus on the SEI formation to select the most appropriate ILs for each available electrode material.

- **Paper IV:** This review focused on SIB electrolytes summarizes the revival of SIB interest since the 2000s. Inspired by LIBs, the future of this technology seem to be bright while accomplished prototypes already appeared in the battery field [267]. SIBs are considered as the best alternative to LIBs and are expected to grow very quickly in the future.
- **Paper V:** ILs as additives have been shown to improve the safety properties of electrolytes, utterly important for future commercialization. However, it would be interesting to use pure IL based electrolytes with good electrochemical properties in a full SIB cell. Larger ESWs and low potential limit upon reduction are the key features to develop further.

Acknowledgements

I would like to thank my supervisors Patrik and Rosa giving me the opportunity to work on an interesting project between Sweden and Spain. The healthy working environment and the quality of facilities have made my PhD a fascinating experience. The financial support from the Swedish Energy Agency, the Swedish Science Council (VR), Stiftelsen Olle Engkvist Byggmästare, and Chalmers Areas of Advance of Materials and Energy, are all gratefully acknowledged.

Thanks to the whole KMF group for the support that it can bring when everything goes wrong, and particularly to Luis, Johan, Susanne, Maciej, Benson, Khalid, Ezio and Erlendur who have welcomed me the very first days of my Swedish journey; they are my old guard. Also, I would like to give a special mention to the two Asian ninjas who occupied MY office when I came back from Barcelona. I have no idea how they manage to stand me for two years.

Also I am really grateful to all the people I have worked with in Spain. El ICMAB is an amazing institute where I could share many ideas and pull out an impressive amount of results which could not be possible to achieve only in Sweden. Muchas gracias, Alex y Jess para vuestra bondad y generosidad durante el año que he pasado en Barcelona.

Je remercie également ma famille et tout particulièrement mes parents pour m'avoir permis d'être ce que je suis à présent.

Bibliography

- [1] G.C. Allen, *Econ J*, 77 (1967) 138-140.
- [2] D. Altschiller, *Libr J*, 132 (2007) 94-94.
- [3] H. Heaton, *Am Hist Rev*, 64 (1959) 351-353.
- [4] R. Rohd, R. Muller, *Berkeley Earth*, (2015) <http://berkeleyearth.org/wp-content/uploads/2015/2008/China-Air-Quality-Paper-July-2015.pdf>.
- [5] IEA, International Energy Agency, (*Key World Energy Statistics*, 2014) 28, 29, 44.
- [6] Y. Nishi, *Chem Rec*, 1 (2001) 406-413.
- [7] S. Megahed, B. Scrosati, *J Power Sources*, 51 (1994) 79-104.
- [8] Y. Nishi, *J Power Sources*, 100 (2001) 101-106.
- [9] J.M. Tarascon, M. Armand, *Nature*, 414 (2001) 359-367.
- [10] IEA, International Energy Agency, (*Key World Energy Statistics*, 2012) 6, 24, 28.
- [11] IEA, International Energy Agency, (*Key World Energy Statistics*, 2013) 6, 24, 28.
- [12] A. Shibata, K. Sato, *Power Eng J*, 13 (1999) 130-135.
- [13] D. Aurbach, Y. Gofer, Z. Lu, A. Schechter, O. Chusid, H. Gizbar, Y. Cohen, V. Ashkenazi, M. Moshkovich, R. Turgeman, E. Levi, *J Power Sources*, 97-8 (2001) 28-32.
- [14] K.F. Blurton, A.F. Sammells, *J Power Sources*, 4 (1979) 263-279.
- [15] Organisation Internationale des Constructeurs Automobiles, (OICA) <http://www.oica.net/>.
- [16] U.S. Geological Survey, 2013 (*Mineral Commodity Summaries 2013*).
- [17] M.D. Slater, D. Kim, E. Lee, C.S. Johnson, *Adv Funct Mater*, 23 (2013) 947-958.
- [18] E.J. Cairns, *Encyclopedia of Energy*, 1 (2004) 117-126.
- [19] J. Kopera, *Inside the Nickel Metal Hydride Battery*, (2004).
- [20] D. Linden, T.B. Reddy, *Handbook of Batteries*, Chapter 26 (2011).
- [21] A. Ponrouch, R. Dedryvere, D. Monti, A.E. Demet, J.M.A. Mba, L. Croguennec, C. Masquelier, P. Johansson, M.R. Palacin, *Energ Environ Sci*, 6 (2013) 2361-2369.
- [22] A. Ponrouch, D. Monti, A. Boschini, B. Steen, P. Johansson, M.R. Palacin, *J Mater Chem A*, 3 (2015) 22-42.
- [23] A. Volta, *Philosophical Transactions Royal Society London*, 90 (1800) 403.
- [24] E. Quartarone, P. Mustarelli, A. Magistris, *Solid State Ionics*, 110 (1998) 1-14.
- [25] K. Kubota, S. Komaba, *J Electrochem Soc*, 162 (2015) A2538-A2550.
- [26] A.J. Bard, L.R. Faulkner, *Electrochemical methods - Fundamentals and Applications*, Wiley, 2001.
- [27] M.R. Palacin, *Chem Soc Rev*, 38 (2009) 2565-2575.
- [28] M.M. Thackeray, J.T. Vaughey, C.S. Johnson, A.J. Kropf, R. Benedek, L.M.L. Fransson, K. Edstrom, *J Power Sources*, 113 (2003) 124-130.
- [29] K. Mizushima, P.C. Jones, P.J. Wiseman, J.B. Goodenough, *Mater Res Bull*, 15 (1980) 783-789.
- [30] A.S. Nagelberg, W.L. Worrell, *J Solid State Chem*, 29 (1979) 345-354.
- [31] C. Delmas, C. Fouassier, P. Hagenmuller, *Physica B & C*, 99 (1980) 81-85.
- [32] J.J. Braconnier, C. Delmas, C. Fouassier, P. Hagenmuller, *Mater Res Bull*, 15 (1980) 1797-1804.
- [33] M.S. Whittingham, *Prog Solid State Ch*, 12 (1978) 41-99.
- [34] H.L. Pan, Y.S. Hu, L.Q. Chen, *Energ Environ Sci*, 6 (2013) 2338-2360.
- [35] B.L. Ellis, L.F. Nazar, *Curr Opin Solid St M*, 16 (2012) 168-177.
- [36] J.P. Parant, R. Olazcuag, M. Devalett, C. Fouassie, P. Hagenmul, *J Solid State Chem*, 3 (1971) 1-11.
- [37] C. Delmas, J.J. Braconnier, C. Fouassier, P. Hagenmuller, *Solid State Ionics*, 3-4 (1981) 165-169.
- [38] J.J. Braconnier, C. Delmas, P. Hagenmuller, *Mater Res Bull*, 17 (1982) 993-1000.
- [39] M.S. Whittingham, *J Chem Soc Chem Comm*, (1974) 328-329.
- [40] M.S. Whittingham, R.A. Huggins, *J Chem Phys*, 54 (1971) 414-416.
- [41] M.S. Whittingham, *Science*, 192 (1976) 1126-1127.

- [42] T. Nagaura, K. Tozawa, *Progress in Batteries and Solar Cells*, 9 (1990) 209-213.
- [43] S. Komaba, W. Murata, T. Ishikawa, N. Yabuuchi, T. Ozeki, T. Nakayama, A. Ogata, K. Gotoh, K. Fujiwara, *Adv Funct Mater*, 21 (2011) 3859-3867.
- [44] S.P. Ong, V.L. Chevrier, G. Hautier, A. Jain, C. Moore, S. Kim, X.H. Ma, G. Ceder, *Energ Environ Sci*, 4 (2011) 3680-3688.
- [45] S.Y. Hong, Y. Kim, Y. Park, A. Choi, N.S. Choi, K.T. Lee, *Energ Environ Sci*, 6 (2013) 2067-2081.
- [46] Y. Liu, F.F. Fan, J.W. Wang, Y. Liu, H.L. Chen, K.L. Jungjohann, Y.H. Xu, Y.J. Zhu, D. Bigio, T. Zhu, C.S. Wang, *Nano Lett*, 14 (2014) 3445-3452.
- [47] D.P. Divincenzo, E.J. Mele, *Phys Rev B*, 32 (1985) 2538-2553.
- [48] J. Sangster, *J Phase Equilib Diff*, 28 (2007) 571-579.
- [49] D.A. Stevens, J.R. Dahn, *J Electrochem Soc*, 147 (2000) 1271-1273.
- [50] J. Zhao, L.W. Zhao, K. Chihara, S. Okada, J. Yamaki, S. Matsumoto, S. Kuze, K. Nakane, *J Power Sources*, 244 (2013) 752-757.
- [51] P. Senguttuvan, G. Rousse, V. Seznec, J.M. Tarascon, M.R. Palacin, *Chem Mater*, 23 (2011) 4109-4111.
- [52] H. Xiong, M.D. Slater, M. Balasubramanian, C.S. Johnson, T. Rajh, *J Phys Chem Lett*, 2 (2011) 2560-2565.
- [53] A.V. Chadwick, S.L.P. Savin, S. Fiddy, R. Alcantara, D.F. Lisbona, P. Lavela, G.F. Ortiz, J.L. Tirado, *J Phys Chem C*, 111 (2007) 4636-4642.
- [54] Q. Sun, Q.Q. Ren, H. Li, Z.W. Fu, *Electrochem Commun*, 13 (2011) 1462-1464.
- [55] L.F. Xiao, Y.L. Cao, J. Xiao, W. Wang, L. Kovarik, Z.M. Nie, J. Liu, *Chem Commun*, 48 (2012) 3321-3323.
- [56] S. Il Park, I. Gocheva, S. Okada, J. Yamaki, *J Electrochem Soc*, 158 (2011) A1067-A1070.
- [57] J.S. Kim, H.J. Ahn, H.S. Ryu, D.J. Kim, G.B. Cho, K.W. Kim, T.H. Nam, J.H. Ahn, *J Power Sources*, 178 (2008) 852-856.
- [58] C.B. Zhu, X.K. Mu, P.A. van Aken, Y. Yu, J. Maier, *Angew Chem Int Edit*, 53 (2014) 2152-2156.
- [59] T.F. Zhou, W.K. Pang, C.F. Zhang, J.P. Yang, Z.X. Chen, H.K. Liu, Z.P. Guo, *Acs Nano*, 8 (2014) 8323-8333.
- [60] Y. Kim, Y. Kim, A. Choi, S. Woo, D. Mok, N.S. Choi, Y.S. Jung, J.H. Ryu, S.M. Oh, K.T. Lee, *Adv Mater*, 26 (2014) 4139-4144.
- [61] J. Fullenwarth, A. Darwiche, A. Soares, B. Donnadieu, L. Monconduit, *J Mater Chem A*, 2 (2014) 2050-2059.
- [62] V.L. Chevrier, G. Ceder, *J Electrochem Soc*, 158 (2011) A1011-A1014.
- [63] A. Darwiche, C. Marino, M.T. Sougrati, B. Fraise, L. Stievano, L. Monconduit, *J Am Chem Soc*, 134 (2012) 20805-20811.
- [64] S.M. Oh, S.T. Myung, C.S. Yoon, J. Lu, J. Hassoun, B. Scrosati, K. Amine, Y.K. Sun, *Nano Lett*, 14 (2014) 1620-1626.
- [65] M.C. Lopez, P. Lavela, G.F. Ortiz, J.L. Tirado, *Electrochem Commun*, 27 (2013) 152-155.
- [66] M. Valvo, F. Lindgren, U. Lafont, F. Bjorefors, K. Edstrom, *J Power Sources*, 245 (2014) 967-978.
- [67] S. Hariharan, K. Saravanan, P. Balaya, *Electrochem Commun*, 31 (2013) 5-9.
- [68] S. Yuan, X.L. Huang, D.L. Ma, H.G. Wang, F.Z. Meng, X.B. Zhang, *Adv Mater*, 26 (2014) 2273-2279.
- [69] L. Zhao, J.M. Zhao, Y.S. Hu, H. Li, Z.B. Zhou, M. Armand, L.Q. Chen, *Adv Energy Mater*, 2 (2012) 962-965.
- [70] M.M. Doeff, Y.P. Ma, S.J. Visco, L.C. Dejonghe, *J Electrochem Soc*, 140 (1993) L169-L170.
- [71] M.M. Doeff, M.Y. Peng, Y.P. Ma, L.C. Dejonghe, *J Electrochem Soc*, 141 (1994) L145-L147.
- [72] A. Ponrouch, A.R. Goni, M.R. Palacin, *Electrochem Commun*, 27 (2013) 85-88.
- [73] D.A. Stevens, J.R. Dahn, *J Electrochem Soc*, 148 (2001) A803-A811.
- [74] P. Thomas, D. Billaud, *Electrochim Acta*, 47 (2002) 3303-3307.
- [75] R. Alcantara, J.M. Jimenez-Mateos, P. Lavela, J.L. Tirado, *Electrochem Commun*, 3 (2001) 639-642.

- [76] T. Kikuchi, K. Kurakane, T. Yamamoto, T. Hattori, M. Makidera, U.S. Patent, US 2010/0248041 A1, (2010).
- [77] C. Delmas, A. Maazaz, P. Hagenmuller, *Solid State Ionics*, 9-10 (1983) 83-88.
- [78] R. Alcantara, M. Jaraba, P. Lavela, J.L. Tirado, *Chem Mater*, 14 (2002) 2847-2848.
- [79] S. Komaba, T. Mikumo, A. Ogata, *Electrochem Commun*, 10 (2008) 1276-1279.
- [80] B. Koo, S. Chattopadhyay, T. Shibata, V.B. Prakapenka, C.S. Johnson, T. Rajh, E.V. Shevchenko, *Chem Mater*, 25 (2013) 245-252.
- [81] A. Jahel, C.M. Ghimbeu, A. Darwiche, L. Vidal, S. Hajjar-Garreau, C. Vix-Guterl, L. Monconduit, *J Mater Chem A*, 3 (2015) 11960-11969.
- [82] P. Wu, N. Du, H. Zhang, J.X. Yu, Y. Qi, D.R. Yang, *Nanoscale*, 3 (2011) 746-750.
- [83] Y. Wang, D.W. Su, C.Y. Wang, G.X. Wang, *Electrochem Commun*, 29 (2013) 8-11.
- [84] T.B. Kim, J.W. Choi, H.S. Ryu, G.B. Cho, K.W. Kim, J.H. Ahn, K.K. Cho, H.J. Ahn, *J Power Sources*, 174 (2007) 1275-1278.
- [85] X.J. Liu, S. Kang, J. Kim, H. Ahn, S. Lim, I. Ahn, *Rare Metals*, 30 (2011) 5-10.
- [86] T.B. Kim, W.H. Jung, H.S. Ryu, K.W. Kim, J.H. Ahn, K.K. Cho, G.B. Cho, T.H. Nam, I.S. Ahn, H.J. Ahn, *J Alloy Compd*, 449 (2008) 304-307.
- [87] J.F. Qian, Y. Chen, L. Wu, Y.L. Cao, X.P. Ai, H.X. Yang, *Chem Commun*, 48 (2012) 7070-7072.
- [88] Y. Park, D.S. Shin, S.H. Woo, N.S. Choi, K.H. Shin, S.M. Oh, K.T. Lee, S.Y. Hong, *Adv Mater*, 24 (2012) 3562-3567.
- [89] V.A. Mihali, S. Renault, L. Nyholm, D. Brandell, *Rsc Adv*, 4 (2014) 38004-38011.
- [90] S.W. Kim, D.H. Seo, X.H. Ma, G. Ceder, K. Kang, *Adv Energy Mater*, 2 (2012) 710-721.
- [91] V. Palomares, P. Serras, I. Villaluenga, K.B. Hueso, J. Carretero-Gonzalez, T. Rojo, *Energ Environ Sci*, 5 (2012) 5884-5901.
- [92] L.P. Wang, L.H. Yu, X. Wang, M. Srinivasan, Z.C.J. Xu, *J Mater Chem A*, 3 (2015) 9353-9378.
- [93] M. Sawicki, L.L. Shaw, *Rsc Adv*, 5 (2015) 53129-53154.
- [94] D. Kim, E. Lee, M. Slater, W.Q. Lu, S. Rood, C.S. Johnson, *Electrochem Commun*, 18 (2012) 66-69.
- [95] S. Komaba, C. Takei, T. Nakayama, A. Ogata, N. Yabuuchi, *Electrochem Commun*, 12 (2010) 355-358.
- [96] N. Yabuuchi, M. Kajiyama, J. Iwatate, H. Nishikawa, S. Hitomi, R. Okuyama, R. Usui, Y. Yamada, S. Komaba, *Nat Mater*, 11 (2012) 512-517.
- [97] M. Sathiyaraj, K. Hemalatha, K. Ramesha, J.M. Tarascon, A.S. Prakash, *Chem Mater*, 24 (2012) 1846-1853.
- [98] C. Masquelier, L. Croguennec, *Chem Rev*, 113 (2013) 6552-6591.
- [99] D.B. Porter, R. Olazcuaga, C. Delmas, F. Cherkaoui, R. Brochu, G. Leflem, *Rev Chim Miner*, 17 (1980) 458-465.
- [100] Z.L. Jian, L. Zhao, H.L. Pan, Y.S. Hu, H. Li, W. Chen, L.Q. Chen, *Electrochem Commun*, 14 (2012) 86-89.
- [101] C. Didier, M. Guignard, C. Denage, O. Szajwaj, S. Ito, I. Saadoune, J. Darriet, C. Delmas, *Electrochem Solid St*, 14 (2011) A75-A78.
- [102] H.M. Liu, H.S. Zhou, L.P. Chen, Z.F. Tang, W.S. Yang, *J Power Sources*, 196 (2011) 814-819.
- [103] K. Saravanan, C.W. Mason, A. Rudola, K.H. Wong, P. Balaya, *Adv Energy Mater*, 3 (2013) 444-450.
- [104] R.A. Shalokor, D.H. Seo, H. Kim, Y.U. Park, J. Kim, S.W. Kim, H. Gwon, S. Lee, K. Kang, *J Mater Chem*, 22 (2012) 20535-20541.
- [105] M. Nishijima, I.D. Gocheva, S. Okada, T. Doi, J. Yamaki, T. Nishida, *J Power Sources*, 190 (2009) 558-562.
- [106] Y.L. Liu, Y.H. Xu, X.G. Han, C. Pellegrinelli, Y.J. Zhu, H.L. Zhu, J.Y. Wan, A.C. Chung, O. Vaaland, C.S. Wang, L.B. Hu, *Nano Lett*, 12 (2012) 5664-5668.
- [107] X.H. Ma, H.L. Chen, G. Ceder, *J Electrochem Soc*, 158 (2011) A1307-A1312.
- [108] J. Billaud, R.J. Clement, A.R. Armstrong, J. Canales-Vazquez, P. Rozier, C.P. Grey, P.G. Bruce, *J Am Chem Soc*, 136 (2014) 17243-17248.

- [109] I.H. Jo, H.S. Ryu, D.G. Gu, J.S. Park, I.S. Ahn, H.J. Ahn, T.H. Nam, K.W. Kim, *Mater Res Bull*, 58 (2014) 74-77.
- [110] J. Zhao, L.W. Zhao, N. Dimov, S. Okada, T. Nishida, *J Electrochem Soc*, 160 (2013) A3077-A3081.
- [111] L.G. Chagas, D. Buchholz, L.M. Wu, B. Vortmann, S. Passerini, *J Power Sources*, 247 (2014) 377-383.
- [112] D.D. Yuan, X.H. Hu, J.F. Qian, F. Pei, F.Y. Wu, R.J. Mao, X.P. Ai, H.X. Yang, Y.L. Cao, *Electrochim Acta*, 116 (2014) 300-305.
- [113] H.J. Yu, S.H. Guo, Y.B. Zhu, M. Ishida, H.S. Zhou, *Chem Commun*, 50 (2014) 457-459.
- [114] P. Barpanda, G. Oyama, S. Nishimura, S.C. Chung, A. Yamada, *Nat Commun*, 5 (2014).
- [115] Y. Kawabe, N. Yabuuchi, M. Kajiyama, N. Fukuhara, T. Inamasu, R. Okuyama, I. Nakai, S. Komaba, *Electrochem Commun*, 13 (2011) 1225-1228.
- [116] Y. Lu, S. Zhang, Y. Li, L.G. Xue, G.J. Xu, X.W. Zhang, *J Power Sources*, 247 (2014) 770-777.
- [117] P. Serras, V. Palomares, P. Kubiak, L. Lezama, T. Rojo, *Electrochem Commun*, 34 (2013) 344-347.
- [118] H.L. Chen, Q. Hao, O. Zivkovic, G. Hautier, L.S. Du, Y.Z. Tang, Y.Y. Hu, X.H. Ma, C.P. Grey, G. Ceder, *Chem Mater*, 25 (2013) 2777-2786.
- [119] M. Nose, H. Nakayama, K. Nobuhara, H. Yamaguchi, S. Nakanishi, H. Iba, *J Power Sources*, 234 (2013) 175-179.
- [120] S.Y. Lim, H. Kim, J. Chung, J.H. Lee, B.G. Kim, J.J. Choi, K.Y. Chung, W. Cho, S.J. Kim, W.A. Goddard, Y. Jung, J.W. Choi, *P Natl Acad Sci USA*, 111 (2014) 599-604.
- [121] L. Wang, Y.H. Lu, J. Liu, M.W. Xu, J.G. Cheng, D.W. Zhang, J.B. Goodenough, *Angew Chem Int Edit*, 52 (2013) 1964-1967.
- [122] R.K.B. Gover, A. Bryan, P. Burns, J. Barker, *Solid State Ionics*, 177 (2006) 1495-1500.
- [123] M. Bianchini, N. Brisset, F. Fauth, F. Weill, E. Elkaim, E. Suard, C. Masquelier, L. Croguennec, *Chem Mater*, 26 (2014) 4238-4247.
- [124] J. Barker, M.Y. Saidi, J. Swoyer, U.S. Patent 6,387,568, (2002).
- [125] H. Vogel, *Phys Z*, 22 (1921) 645-646.
- [126] G. Tammann, W. Hesse, *Z Anorg Allg Chem*, 156 (1926).
- [127] G.S. Fulcher, *J Am Ceram Soc*, 8 (1925) 339-355.
- [128] F. Croce, G.B. Appetecchi, L. Persi, B. Scrosati, *Nature*, 394 (1998) 456-458.
- [129] F. Croce, L. Settimi, B. Scrosati, D. Zane, *J New Mat Electr Sys*, 9 (2006) 3-9.
- [130] K. Xu, *Chem Rev*, 104 (2004) 4303-4417.
- [131] V.M. Mohan, V. Raja, P.B. Bhargav, A.K. Sharma, V.V.R.N. Rao, *J Polym Res*, 14 (2007) 283-290.
- [132] M. Patel, K.G. Chandrappa, A.J. Bhattacharyya, *Solid State Ionics*, 181 (2010) 844-848.
- [133] J.W. Hoj, J. Engell, *Mat Sci Eng B-Solid*, 19 (1993) 228-233.
- [134] D. Monti, E. Jónsson, M.R. Palacin, P. Johansson, *J Power Sources*, 245 (2014) 630-636.
- [135] J.T. Kummer, N. Weber, *Sae Transactions*, 76 (1968) 88-99.
- [136] K.B. Hueso, M. Armand, T. Rojo, *Energ Environ Sci*, 6 (2013) 734-749.
- [137] P.B. Bhargav, V.M. Mohan, A.K. Sharma, V.V.R.N. Rao, *Ionics*, 13 (2007) 441-446.
- [138] S. Link, M.A. El-Sayed, *J Phys Chem B*, 103 (1999) 4212-4217.
- [139] K. Koga, T. Ikeshoji, K. Sugawara, *Phys Rev Lett*, 92 (2004).
- [140] S.K. Ghosh, T. Pal, *Chem Rev*, 107 (2007) 4797-4862.
- [141] E. Peled, C. Menachem, D. BarTow, A. Melman, *J Electrochem Soc*, 143 (1996) L4-L7.
- [142] K.H. Su, Q.H. Wei, X. Zhang, J.J. Mock, D.R. Smith, S. Schultz, *Nano Lett*, 3 (2003) 1087-1090.
- [143] G. Akerlof, *J Am Chem Soc*, 54 (1932) 4125-4139.
- [144] M. Salomon, *Pure Appl Chem*, 70 (1998) 1905-1912.
- [145] J. Barthel, H.J. Gores, R. Neueder, A. Schmid, *Pure Appl Chem*, 71 (1999) 1705-1715.
- [146] E. Jonsson, P. Johansson, *Phys Chem Chem Phys*, 14 (2012) 10774-10779.
- [147] Y. Ikezawa, H. Nishi, *Electrochim Acta*, 53 (2008) 3663-3669.
- [148] S.K. Jeong, M. Inaba, Y. Iriyama, T. Abe, Z. Ogumi, *Electrochim Acta*, 47 (2002) 1975-1982.
- [149] M. Morita, Y. Asai, N. Yoshimoto, M. Ishikawa, *J Chem Soc Faraday T*, 94 (1998) 3451-3456.

- [150] R. Fong, U. Vonsacken, J.R. Dahn, *J Electrochem Soc*, 137 (1990) 2009-2013.
- [151] X. Xia, J.R. Dahn, *J Electrochem Soc*, 159 (2012) A647-A650.
- [152] X. Xia, J.R. Dahn, *J Electrochem Soc*, 159 (2012) A1048-A1051.
- [153] A. Ponrouch, E. Marchante, M. Courty, J.M. Tarascon, M.R. Palacin, *Energ Environ Sci*, 5 (2012) 8572-8583.
- [154] C. Vidal-Abarca, P. Lavela, J.L. Tirado, A.V. Chadwick, M. Alfredsson, E. Kelder, *J Power Sources*, 197 (2012) 314-318.
- [155] Z.L. Jian, W.Z. Han, X. Lu, H.X. Yang, Y.S. Hu, J. Zhou, Z.B. Zhou, J.Q. Li, W. Chen, D.F. Chen, L.Q. Chen, *Adv Energy Mater*, 3 (2013) 156-160.
- [156] H. Olivier-Bourbigou, L. Magna, *J Mol Catal a-Chem*, 182 (2002) 419-437.
- [157] M. Armand, F. Endres, D.R. MacFarlane, H. Ohno, B. Scrosati, *Nat Mater*, 8 (2009) 621-629.
- [158] J.P. Hallett, T. Welton, *Chem Rev*, 111 (2011) 3508-3576.
- [159] S.J. Zhang, N. Sun, X.Z. He, X.M. Lu, X.P. Zhang, *J Phys Chem Ref Data*, 35 (2006) 1475-1517.
- [160] T. Welton, *Chem Rev*, 99 (1999) 2071-2083.
- [161] M. Galinski, A. Lewandowski, I. Stepniak, *Electrochim Acta*, 51 (2006) 5567-5580.
- [162] A. Lewandowski, M. Galinski, *General properties of ionic liquids as electrolytes for carbon-based double layer capacitors*, Springer, The Netherland, (2006).
- [163] O. Zech, M. Kellermeier, S. Thomaier, E. Maurer, R. Klein, C. Schreiner, W. Kunz, *Chem-Eur J*, 15 (2009) 1341-1345.
- [164] O. Zech, J. Hunger, J.R. Sangoro, C. Iacob, F. Kremer, W. Kunz, R. Buchner, *Phys Chem Chem Phys*, 12 (2010) 14341-14350.
- [165] P.G. Jessop, *Green Chem*, 13 (2011) 1391-1398.
- [166] Y. Zhang, B.R. Bakshi, E.S. Demessie, *Environ Sci Technol*, 42 (2008) 1724-1730.
- [167] C.S. Ding, T. Nohira, K. Kuroda, R. Hagiwara, A. Fukunaga, S. Sakai, K. Nitta, S. Inazawa, *J Power Sources*, 238 (2013) 296-300.
- [168] C.S. Ding, T. Nohira, R. Hagiwara, K. Matsumoto, Y. Okamoto, A. Fukunaga, S. Sakai, K. Nitta, S. Inazawa, *J Power Sources*, 269 (2014) 124-128.
- [169] T. Nohira, T. Ishibashi, R. Hagiwara, *J Power Sources*, 205 (2012) 506-509.
- [170] A. Fukunaga, T. Nohira, Y. Kozawa, R. Hagiwara, S. Sakai, K. Nitta, S. Inazawa, *J Power Sources*, 209 (2012) 52-56.
- [171] T. Yamamoto, T. Nohira, R. Hagiwara, A. Fukunaga, S. Sakai, K. Nitta, S. Inazawa, *J Power Sources*, 217 (2012) 479-484.
- [172] A. Fukunaga, T. Nohira, R. Hagiwara, K. Numata, E. Itani, S. Sakai, K. Nitta, S. Inazawa, *J Power Sources*, 246 (2014) 387-391.
- [173] C. Ding, T. Nohira, R. Hagiwara, A. Fukunaga, S. Sakai, K. Nitta, *Electrochim Acta*, 176 (2015) 344-349.
- [174] S.A.M. Noor, P.C. Howlett, D.R. MacFarlane, M. Forsyth, *Electrochim Acta*, 114 (2013) 766-771.
- [175] H. Yoon, H.J. Zhu, A. Hervault, M. Armand, D.R. MacFarlane, M. Forsyth, *Phys Chem Chem Phys*, 16 (2014) 12350-12355.
- [176] J.S. Moreno, G. Maresca, S. Panero, B. Scrosati, G.B. Appetecchi, *Electrochem Commun*, 43 (2014) 1-4.
- [177] N. Wongittharom, T.C. Lee, C.H. Wang, Y.C. Wang, J.K. Chang, *J Mater Chem A*, 2 (2014) 5655-5661.
- [178] K. Matsumoto, T. Hosokawa, T. Nohira, R. Hagiwara, A. Fukunaga, K. Numata, E. Itani, S. Sakai, K. Nitta, S. Inazawa, *J Power Sources*, 265 (2014) 36-39.
- [179] A. Guerfi, M. Dontigny, P. Charest, M. Petitclerc, M. Lagace, A. Vijn, K. Zaghib, *J Power Sources*, 195 (2010) 845-852.
- [180] R.S. Kuhnel, A. Balducci, *J Phys Chem C*, 118 (2014) 5742-5748.
- [181] S. Menne, R.S. Kuhnel, A. Balducci, *Electrochim Acta*, 90 (2013) 641-648.
- [182] S. Wilken, S.Z. Xiong, J. Scheers, P. Jacobsson, P. Johansson, *J Power Sources*, 275 (2015) 935-942.

- [183] T. Sato, T. Maruo, S. Marukane, K. Takagi, *J Power Sources*, 138 (2004) 253-261.
- [184] M. Montanino, M. Moreno, M. Carewska, G. Maresca, E. Simonetti, R. Lo Presti, F. Alessandrini, G.B. Appetecchi, *J Power Sources*, 269 (2014) 608-615.
- [185] T. Vogl, S. Menne, A. Balducci, *Phys Chem Chem Phys*, 16 (2014) 25014-25023.
- [186] L. Lombardo, S. Brutti, M.A. Navarra, S. Panero, P. Reale, *J Power Sources*, 227 (2013) 8-14.
- [187] B.B. Yang, C.H. Li, J.H. Zhou, J.H. Liu, Q.L. Zhang, *Electrochim Acta*, 148 (2014) 39-45.
- [188] A.S. Arico, P. Bruce, B. Scrosati, J.M. Tarascon, W. Van Schalkwijk, *Nat Mater*, 4 (2005) 366-377.
- [189] P.G. Bruce, B. Scrosati, J.M. Tarascon, *Angew Chem Int Edit*, 47 (2008) 2930-2946.
- [190] J.B. Goodenough, Y. Kim, *Chem Mater*, 22 (2010) 587-603.
- [191] C. Liu, F. Li, L.P. Ma, H.M. Cheng, *Adv Mater*, 22 (2010) E28-E62.
- [192] E. Peled, H. Yamin, *Israel J Chem*, 18 (1979) 131-135.
- [193] P. Verma, P. Maire, P. Novak, *Electrochim Acta*, 55 (2010) 6332-6341.
- [194] D. Aurbach, B. Markovsky, A. Shechter, Y. EinEli, H. Cohen, *J Electrochem Soc*, 143 (1996) 3809-3820.
- [195] D. Aurbach, M.D. Levi, E. Levi, A. Schechter, *J Phys Chem B*, 101 (1997) 2195-2206.
- [196] D. Aurbach, A. Zaban, *J Electroanal Chem*, 348 (1993) 155-179.
- [197] A.M. Andersson, K. Edstrom, *J Electrochem Soc*, 148 (2001) A1100-A1109.
- [198] A. Kominato, E. Yasukawa, N. Sato, T. Ijuuin, H. Asahina, S. Mori, *J Power Sources*, 68 (1997) 471-475.
- [199] N. Weadock, N. Varongchayakul, J.Y. Wan, S. Lee, J. Seog, L.B. Hu, *Nano Energy*, 2 (2013) 713-719.
- [200] M.A. Munoz-Marquez, M. Zarrabeitia, E. Castillo-Martinez, A. Eguia-Barrio, T. Rojo, M. Casas-Cabanas, *Acs Appl Mater Inter*, 7 (2015) 7801-7808.
- [201] S. Wenzel, T. Hara, J. Janek, P. Adelhelm, *Energ Environ Sci*, 4 (2011) 3342-3345.
- [202] L. Vogdanis, B. Martens, H. Uchtmann, F. Hensel, W. Heitz, *Makromol Chem*, 191 (1990) 465-472.
- [203] A. Abouimrane, W. Weng, H. Eltayeb, Y.J. Cui, J. Niklas, O. Poluektov, K. Amine, *Energ Environ Sci*, 5 (2012) 9632-9638.
- [204] R. Dedryvere, D. Foix, S. Franger, S. Patoux, L. Daniel, D. Gonbeau, *J Phys Chem C*, 114 (2010) 10999-11008.
- [205] R. Dedryvere, M. Maccario, L. Croguennec, F. Le Cras, C. Delmas, D. Gonbeau, *Chem Mater*, 20 (2008) 7164-7170.
- [206] H. Duncan, D. Duguay, Y. Abu-Lebdeh, I.J. Davidson, *J Electrochem Soc*, 158 (2011) A537-A545.
- [207] M. Broussely, P. Biensan, F. Bonhomme, P. Blanchard, S. Herreyre, K. Nechev, R.J. Staniewicz, *J Power Sources*, 146 (2005) 90-96.
- [208] A.M. Andersson, D.P. Abraham, R. Haasch, S. Maclaren, J. Liu, K. Amine, *J Electrochem Soc*, 149 (2002) A1358-A1369.
- [209] I. Yamada, K. Miyazaki, T. Fukutsuka, Y. Iriyama, T. Abe, Z. Ogumi, *J Power Sources*, 294 (2015) 460-464.
- [210] D. Aurbach, K. Gamolsky, B. Markovsky, G. Salitra, Y. Gofer, U. Heider, R. Oesten, M. Schmidt, *J Electrochem Soc*, 147 (2000) 1322-1331.
- [211] Y.F. Yuan, H.M. Wu, S.Y. Guo, J.B. Wu, J.L. Yang, X.L. Wang, J.P. Tu, *Appl Surf Sci*, 255 (2008) 2225-2229.
- [212] J.W. Lee, S.M. Park, H.J. Kim, *Electrochem Commun*, 11 (2009) 1101-1104.
- [213] X.F. Li, Y.L. Xu, *Appl Surf Sci*, 253 (2007) 8592-8596.
- [214] J.S. Kim, C.S. Johnson, J.T. Vaughey, S.A. Hackney, K.A. Walz, W.A. Zeltner, M.A. Anderson, M.M. Thackeray, *J Electrochem Soc*, 151 (2004) A1755-A1761.
- [215] N.E. Hill, W. Vaughan, A. Price, M. Davis, *Dielectric properties and molecular behaviour*, Van Nostrand, London, 1969.
- [216] A.R. Blythe, *Electrical properties of polymers*, Cambridge University Press, 1979.

- [217] J. Chamberlain, G.W. Chantry, High frequency dielectric measurement, IPC Science and Technology Press, Guildford, 1973.
- [218] C.J.F. Böttcher, P. Bordewijk, Theory of electric polarization, vol II. Dielectrics in time-dependent fields, Elsevier, Oxford New York, 1978.
- [219] F. Kremer, A. Schönhals, Broadband Dielectric spectroscopy, Springer, 2003.
- [220] A. Smekal, *Naturwissenschaften*, 11 (1923) 873-875.
- [221] C.V. Raman, K.S. Krishnan, *Nature*, 121 (1928) 501-502.
- [222] G.G. Stokes, *Mathematical and Physical Papers*, (1880) Cambridge.
- [223] H.O. Di Rocco, D.I. Iriarte, J. Pomarico, *Appl Spectrosc*, 55 (2001) 822-826.
- [224] M. Bradley, *Curve Fitting in Raman and IR Spectroscopy: Basic Theory of Line Shapes and Applications*, Thermo Fischer Scientific, (2007).
- [225] R.J. Meier, *Vib Spectrosc*, 39 (2005) 266-269.
- [226] M.J. Hollas, *Modern Spectroscopy*, (1998) 35-36.
- [227] D.M.P. Mingos, D.R. Baghurst, *Chem Soc Rev*, 20 (1991) 1-47.
- [228] I. Bilecka, M. Niederberger, *Nanoscale*, 2 (2010) 1358-1374.
- [229] S.H. Kang, J.B. Goodenough, *J Electrochem Soc*, 147 (2000) 3621-3627.
- [230] K.T. Hwang, W.S. Um, H.S. Lee, J.K. Song, K.W. Chung, *J Power Sources*, 74 (1998) 169-174.
- [231] D.M.P. Mingos, A.G. Whittaker, Van Eldik R, Hubbard C.D, (eds) *Chemistry under extreme or non-classical conditions*, Wiley, New York, 1996.
- [232] P. Chantrey, *Electron Power*, 29 (1983) 659-659.
- [233] D. Stuerger, K. Gonon, M. Lallemand, *Tetrahedron*, 49 (1993) 6229-6234.
- [234] W. Wu, A. Mohamed, J.F. Whitacre, *J Electrochem Soc*, 160 (2013) A497-A504.
- [235] S. Balaji, D. Mutharasu, N. Sankara Subramanian, K. Ramanathan, *Ionics*, 15 (2009) 765-777.
- [236] H.W. Yan, X.J. Huang, Z.H. Lu, H. Huang, R.J. Xue, L.Q. Chen, *J Power Sources*, 68 (1997) 530-532.
- [237] H. Li, Z.H. Lu, H. Huang, X.J. Huang, L.Q. Chen, *Ionics*, 2 (1996) 259-265.
- [238] S. Wilken, S.Z. Xiong, J. Scheers, P. Jacobsson, P. Johansson, *J Power Sources*, 283 (2015) 531-531.
- [239] S. Wilken, P. Johansson, P. Jacobsson, B. Scrosati, K.M. Abraham, W. Schalkwijk, J. Hassoun, *Lithium Batteries: Advanced Technologies and Applications*, Wiley, Chapter 3 (2013).
- [240] B. Garcia, S. Lavalley, G. Perron, C. Michot, M. Armand, *Electrochim Acta*, 49 (2004) 4583-4588.
- [241] S. Seki, Y. Ohno, Y. Kobayashi, H. Miyashiro, A. Usami, Y. Mita, H. Tokuda, M. Watanabe, K. Hayamizu, S. Tsuzuki, M. Hattori, N. Terada, *J Electrochem Soc*, 154 (2007) A173-A177.
- [242] J.K. Kim, A. Matic, J.H. Ahn, P. Jacobsson, *J Power Sources*, 195 (2010) 7639-7643.
- [243] H. Yoon, A.S. Best, M. Forsyth, D.R. MacFarlane, P.C. Howlett, *Phys Chem Chem Phys*, 17 (2015) 4656-4663.
- [244] M.S. Ding, T.R. Jow, *J Electrochem Soc*, 151 (2004) A2007-A2015.
- [245] A. Bhide, J. Hofmann, A.K. Durr, J. Janek, P. Adelhelm, *Phys Chem Chem Phys*, 16 (2014) 1987-1998.
- [246] S. Seki, Y. Kobayashi, H. Miyashiro, Y. Ohno, A. Usami, Y. Mita, N. Kihira, M. Watanabe, N. Terada, *J Phys Chem B*, 110 (2006) 10228-10230.
- [247] J.C. Lassegues, J. Grondin, D. Talaga, *Phys Chem Chem Phys*, 8 (2006) 5629-5632.
- [248] S. Duluard, J. Grondin, J.L. Bruneel, I. Pianet, A. Grelard, G. Campet, M.H. Delville, J.C. Lassegues, *J Raman Spectrosc*, 39 (2008) 627-632.
- [249] Y. Umebayashi, T. Mitsugi, S. Fukuda, T. Fujimori, K. Fujii, R. Kanzaki, M. Takeuchi, S.I. Ishiguro, *J Phys Chem B*, 111 (2007) 13028-13032.
- [250] J.C. Lassegues, J. Grondin, C. Aupetit, P. Johansson, *J Phys Chem A*, 113 (2009) 305-314.
- [251] D. Brouillette, D.E. Irish, N.J. Taylor, G. Perron, M. Odziemkowski, J.E. Desnoyers, *Phys Chem Chem Phys*, 4 (2002) 6063-6071.
- [252] M. Castriota, T. Caruso, R.G. Agostino, E. Cazzanelli, W.A. Henderson, S. Passerini, *J Phys Chem A*, 109 (2005) 92-96.

- [253] A. Bakker, S. Gejji, J. Lindgren, K. Hermansson, M.M. Probst, *Polymer*, 36 (1995) 4371-4378.
- [254] L. Edman, *J Phys Chem B*, 104 (2000) 7254-7258.
- [255] B. Fortunat, P. Mirone, G. Fini, *Spectrochimica Acta, A* 27 (1971) 1917-1927.
- [256] K.L. Dorris, J.E. Boggs, A. Danti, L.L. Altpeter, *J Chem Phys*, 46 (1967) 1191-1193.
- [257] J.R. Durig, G.L. Coulter, D.W. Wertz, *J Mol Spectrosc*, 27 (1968) 285-295.
- [258] J.L. Allen, O. Borodin, D.M. Seo, W.A. Henderson, *J Power Sources*, 267 (2014) 821-830.
- [259] B. Klassen, R. Aroca, M. Nazri, G.A. Nazri, *J Phys Chem B*, 102 (1998) 4795-4801.
- [260] L.W. Ji, Z. Lin, M. Alcoutlabi, X.W. Zhang, *Energ Environ Sci*, 4 (2011) 2682-2699.
- [261] M.H. Bhat, B.P. Chakravarthy, P.A. Ramakrishnan, A. Levasseur, K.J. Rao, *B Mater Sci*, 23 (2000) 461-466.
- [262] S. Mahshid, M. Askari, M.S. Ghamsari, *J Mater Process Tech*, 189 (2007) 296-300.
- [263] A.K. Rai, L.T. Anh, J. Gim, V. Mathew, J. Kang, B.J. Paul, J. Song, J. Kim, *Electrochim Acta*, 90 (2013) 112-118.
- [264] D. Zhang, J.P. Tu, J.Y. Xiang, Y.Q. Qiao, X.H. Xia, X.L. Wang, C.D. Gu, *Electrochim Acta*, 56 (2011) 9980-9985.
- [265] R.S. Kuhnel, M. Lubke, M. Winter, S. Passerini, A. Balducci, *J Power Sources*, 214 (2012) 178-184.
- [266] C.X. Peng, L. Yang, B.F. Wang, Z.X. Zhang, N. Li, *Chinese Sci Bull*, 51 (2006) 2824-2830.
- [267] L. Cailloce, A battery revolution in motion, (accessed 2015-12-15), <https://news.cnrs.fr/articles/a-battery-revolution-in-motion>.